

A Finite Element Model of the LHC Dipole Cold Mass with Hysteretic, Non-linear Behavior and Single Turn Description: Towards the Interpretation of Magnet Quenches

THÈSE N° 4259 (2008)

PRÉSENTÉE
À LA FACULTÉ DES SCIENCES DE BASE

Laboratoire de physique des hautes énergies 1

PROGRAMME DOCTORAL EN PHYSIQUE
ÉCOLE POLYTECHNIQUE FÉDÉRALE DE LAUSANNE

POUR L'OBTENTION DU GRADE DE DOCTEUR ÈS SCIENCES
PAR

Mirko Pojer

Laurea in Fisica, Università degli Studi di Milano, Italie
et de nationalité italienne

acceptée sur proposition du jury:

Prof. R. Schaller, président du jury

Prof. L. Rivkin, directeur de thèse

Prof. A. Bay, rapporteur

Dr. A. Devred, rapporteur

Dr. W. Scandale, rapporteur



Suisse
(2008)

SPONSORED BY



"Bien podrán los encantadores
quitarme la ventura, pero el esfuerzo
y el ánimo, será imposible"

(Don Quijote)

A mis dos joyas...

ABSTRACT

In one of its acceptation, the word *quench* is synonym of destruction. And this is even more consistent with reality in the case of the Large Hadron Collider dipole magnets, whose magnetic field and stored energy are unprecedented: the uncontrolled transition from the superconducting to the resistive state can be the origin of dramatic events. This is why the protection of magnets is so important, and why so many studies and investigations have been carried out on quench origin.

The production, cold testing and installation of the 1232 arc dipole magnets is completed. They have fulfilled all the requirements and the operation reliability of these magnets has already been partially confirmed. From an academic standpoint, nevertheless, the anomalous mechanical behaviour, which was sometimes observed during power tests, has not yet been given a clear explanation. The work presented in this thesis aims at providing an instrument to better understand the reasons for such anomalies, by means of finite element modelling of the cross-section of the dipole cold mass.

During the investigation on quench phenomenology and its characterization, a distinction can be done between the two main quench origins during cold test without beam: the local degradation of the conductor and the frictional heating resulting from mechanical disturbances (such as conductor motion under the effects of the Lorentz forces). Concerning the second type, it is illustrated how important a good positioning of the cables is in a magnet cross-section and which is the fundamental role of azimuthal pre-stress. There are numerous studies of the consequences of conductor motion under the effect of electro-magnetic forces and of the loss of pre-stress during energization. However, no model has ever been able to reproduce in detail and predict such phenomena. The present model, developed in ANSYS® environment, was initiated with the idea of representing the real behaviour of an LHC-type dipole coil, by taking into account each turn individually, reproducing the non-linear and hysteretic mechanical behaviour observed on a stack of insulated cables and inserting friction between mating surfaces. The representation of the mechanical complexity of the composite material is certainly one of the originalities of this study. To validate the model, a comparison with elastic modulus measurements, systematically performed in industry, was carried out, both for single layers and for assembled poles. The agreement is certainly worth the effort lavished and justifies the following steps in simulation, which are the modelling of the collaring mechanism and the cool-down process. These are other important and original elements. The last one, in particular, requires progressively changing the mechanical properties of the superconductor, following the temperature profile. This implied some simplifications to comply with the enhanced convergence difficulties, but does not invalidate the goodness of the description and the results obtained. This is a faithful reproduction of a magnet life-cycle, uncommon in this kind of studies.

Keywords: finite element model, LHC dipole, superconducting accelerator magnet, mechanical hysteresis, quench.

RESUME

Une des définitions du mot *quench* est synonyme de destruction. C'est encore plus réel dans le cas des aimants dipôles du Large Hadron Collider, où le champ magnétique et l'énergie stocké sont sans précédents: la transition de l'état supraconducteur à l'état résistif de manière incontrôlée peut être à l'origine d'événements dramatiques. C'est pourquoi la protection des aimants est si importante et pourquoi autant d'études ont été menées sur l'origine du quench.

La production, les tests à froid et l'installation des 1232 aimants dipôles dans les arcs est terminée. Ces aimants ont remplis tous les prérequis et la fiabilité opérationnelle de ces aimants a déjà été confirmée en partie. D'un point de vue académique, néanmoins, le comportement mécanique anormal, qui a été parfois observé durant les tests en puissance, n'a pas encore eu d'explication claire. Le travail présenté dans cette thèse a pour but de fournir un instrument pour une meilleure compréhension des raisons de ces anomalies, par l'aide de modélisation aux éléments finis de la section transversale de la masse froide d'un dipôle.

Durant l'étude du phénomène de quench et sa caractérisation, une distinction peut être faite entre les deux origines principales de quench durant la mise en puissance sans faisceau: la dégradation locale du conducteur et l'échauffement par frottement résultant des perturbations mécaniques (comme un déplacement du conducteur sous la force de Lorentz). Concernant le second type, il est démontré l'importance d'un bon positionnement des câbles dans la section transversale de l'aimant et quel est le rôle fondamental des précontraintes azimutales. De nombreuses études existent sur la conséquence du mouvement d'un conducteur sous l'effet d'une force électromagnétique et la perte de précontraintes durant l'énergisation. Néanmoins aucun modèle n'a jamais été capable de reproduire en détail et prédire un tel phénomène. Ce modèle, développé dans un environnement ANSYS®, avait comme idée initiale de représenter le comportement réel d'une bobine dipôle type LHC, en prenant en compte chaque spire individuellement, reproduisant la non-linéarité et les hystérésis mécaniques observées sur un empilement des câbles isolés et ajoutant le frottement entre surfaces en contact. La représentation de la complexité mécanique du matériel composite est certainement une des particularités de cette étude. Pour valider le modèle, une comparaison avec les mesures du module élastique, effectuées de manière systématique en industrie, a été menée sur des couches simples et sur des pôles assemblés. Le résultat est certainement à la hauteur des efforts produits et justifie les étapes suivantes en simulation, qui consistent à modéliser le mécanisme de *collaring* et du processus de refroidissement. Ceux-ci sont d'autres éléments importants et originaux. Le dernier, en particulier, nécessite le changement progressif des propriétés mécaniques du supraconducteur, suivant son profil de température. Et il implique quelques simplifications pour suivre les difficultés augmentées de la convergence mathématique. Mais ceci n'invalide pas la justesse de la description et des

résultats obtenus. Celle présenté est une réelle reproduction d'un cycle de vie de l'aimant, ce qui est rare dans ce type d'études.

Mots clé: model à éléments finîtes, dipôle du LHC, aimants supraconductifs pour accélérateurs, hystérésis mécanique.

ACKNOWLEDGEMENT

I would first like to express my gratitude to Dr. Arnaud Devred, for the confidence and the appreciation he showed in granting me such an interesting work. I am grateful to him for his continuous support and the lengthy discussions we had, and for his punctilious remarks, that certainly improved the quality of this report. Merci.

To Dr. Walter Scandale my greatest appreciation for his support. I am also grateful to Prof. Lucio Rossi for encouraging me in pursuing such an important objective: years are passing, but I am still ‘one of his students’. Grazie ad entrambe.

I would like to warmly thank Prof. Albin Wrulich, who first gave me the chance of carrying out this job with EPFL, and Prof. Leonid Rivkin that supported me with trustfulness. They have believed in this project and always encouraged me with professionalism and friendly help.

Among the persons that helped me in developing my model, my greatest esteem goes to Dr. Stefania Farinon, who introduced me to the still mysterious world of finite elements and whose initial help was fundamental for the course of this job. To Dr. Paolo Fessia I have to credit as well my appreciation, for his uncommon availability and for his valuable suggestions and advices. My thanks also go to Dr. Marco La China and Dr. Alessandro Dallochio, for their professional guidance to a profane.

Grazie alla mia famiglia, e in particolare ai miei genitori, Maria e Guerrino, per il loro continuo e affettuoso supporto. Muchas gracias a Esther y Juan Antonio, por preguntarme sin tregua “cuándo acabas la tesis?”.

Thank you very much to all my friends, who filled and continue filling my life in Geneva.

Last but not least, a lovely thank you to Ester and Irene, who give colour and sweetness to my life: without them all this would have not been possible. Os quiero mucho.

Contents

Abstract	v
Résumé	vii
1. THE LARGE HADRON COLLIDER	1
1.1. CERN and the LHC: half a century of innovation.....	3
1.2. The LHC	4
1.2.1. The reason for a new accelerator.....	4
1.2.2. The injection and acceleration chain	5
1.2.3. The machine layout	8
1.3. Four giants... and a half: the experiments	10
Bibliography	13
2. THE LHC DIPOLE MAGNETS.....	15
2.1. At the edge of technology	17
2.1.1. The need for superconducting magnets	17
2.1.2. Fundamentals of superconductivity.....	18
2.1.3. Why superfluid helium.....	20
2.2. Ten years of magnet development	22
2.2.1. The R&D program.....	22
2.2.2. The final design	23
Bibliography	27
3. MECHANICAL STABILITY AND QUENCH ORIGIN.....	29
3.1. Magnet performance limitations: QUENCH	31
3.1.1. Quench phenomenology and magnet protection	31
3.1.2. Protection for the LHC magnet strings.....	34
3.1.3. Experimental characterization of a quench	36
3.1.4. Quench origin	39
3.2. Conductor-limited quenches	41
3.2.1. Mechanical stabilization of coil and cryogenic transition	41
3.2.2. Comparison with critical current.....	43
3.2.3. Algorithm for temperature margin estimate	48
3.3. Solid friction and heat generation	50
3.3.1. Stick-Slip phenomenology	51
3.3.2. Mechanical constraints failure: one real case	54

3.4. Some remarks	58
Bibliography	59
4. STATISTICAL TREATMENT OF SERIES DIPOLE QUENCHES.....	61
4.1. Technical specification for the supply of the cold masses.....	63
4.1.1. Room temperature acceptance tests.....	63
4.1.2. Acceptance tests at liquid helium temperature	64
4.1.3. Diagnosis of non-conformities	66
4.2. Quench results from the cold test of 1261 dipoles.....	67
4.2.1. Global magnet performance	68
4.2.2. Performance of the magnets selected for the machine	69
4.2.3. Statistics on longitudinal distribution of quenches.....	71
Bibliography	79
5. THE ANSYS® MODEL.....	81
5.1. Objectives and definition of the model.....	83
5.2. ANSYS® contact capabilities.....	85
5.2.1. Definition of the design and influence of friction	85
5.2.2. Contact characterization	87
5.3. Material properties and MELAS function	90
5.3.1. Stress-strain characteristics for the superconductor	90
5.3.2. Material non-linearity and hysteresis at room temperature	93
5.4. From simple numerical models to complete structure.....	97
5.5. Results of the simulations	105
Bibliography	108
6. MANUFACTURING, COOLING AND POWERING THE LHC DIPOLE	109
6.1. Reproducing the collaring of the coils.....	111
6.1.1. Collaring the superconducting coils	111
6.2. Reproducing the cool-down of the coils	114
6.2.1. Thermal contraction coefficient	114
6.2.2. Evaluating the thermal contraction for the coils.....	115
6.2.3. Cooling the magnet	117
6.3. Powering the magnet	118
6.4. Analysis of the simulations.....	119
Bibliography	125
CONCLUSIONS.....	127

A1. MANUFACTURING THE DIPOLES AT THE THREE FIRMS (UP TO PRE-	
COLLARING).....	131
Preliminary remarks.....	133
A1.1. Components and tooling	133
A1.1.1. Cable insulation	133
A1.1.2. Angular copper wedges	134
A1.1.3. End spacers	134
A1.1.4. Inter-layer spacers.....	135
A1.1.5. Ground plane insulation.....	135
A1.1.6. Collars.....	137
A1.1.7. Winding machine and winding mandrels	137
A1.1.8. Sizing bars, protection sheets and suiting covers.....	139
A1.1.9. Mould top hats and curing presses.....	139
A1.2. Winding and curing.....	141
A1.2.1. Layer-jump preparation	141
A1.2.2. Winding: mandrel covers, winding tension and duration	141
A1.2.3. Support of coil heads during winding.....	143
A1.2.4. Curing	145
A1.2.5. Re-surfacing.....	147
A1.3. Young's modulus measurements and shimming	149
A1.3.1. Pole assembly	150
A1.3.2. Pole end measurement and shimming	152
A1.4. Ground plane insulation and pre-collaring.....	153
A1.4.1. Pre-collaring	155

CHAPTER 1

THE LARGE HADRON COLLIDER

1.1. CERN AND THE LHC: HALF A CENTURY OF INNOVATION.

Once completed and operational, the new accelerator being built at CERN, the Large Hadron Collider (LHC), will be the largest and most powerful accelerator ever built. It represents a masterpiece in technology but it also breaks off with an old way of building accelerators: it will be, in fact, the first accelerator built at CERN with strong support from all over the world (India, Japan, USA, Russia and many others). CERN (Conseil Européen pour la Recherche Nucléaire) was indeed proposed in 1949, and finally created in Geneva in 1954, to restore Europe's prominent role in fundamental physics research and "to assist and encourage the formation and organization of regional centers and laboratories in order to increase and make more fruitful the international collaboration of scientists..." [Rabi, 1950]. Important discoveries were since then made at CERN and a series of machines were constructed to go along with physics requirements for deeper investigation and understanding of Nature. The Synchrocyclotron (SC) was the first accelerator, with a 600 MeV energy, followed by the Proton Synchrotron (PS) and the ISR (Intersecting Storage Ring), which was the first proton-proton collider, with continuous proton beams colliding at a momentum of about 30 GeV/c; in the SPS (Super Proton Synchrotron) bunched proton and antiproton beams were accelerated from 26 GeV/c to 315 GeV/c and brought into collision, and it was there that the Z^0 and W bosons were discovered [Rubbia, 1994].

The construction of LEP (Large Electron Positron collider) was approved in 1981; it was designed as a Z factory (it was, in fact, conceived before the discovery of this particle with the SPS in 1983) and was accelerating electrons and positrons in opposite directions in a common vacuum pipe inside a ring of conventional, resistive magnets, before making them collide head-on in four intersection regions. The initial energy was chosen to be around 91 GeV, so that, in the collisions, a Z^0 particle would be produced. During the second phase (called LEP2), at the end of 1995, its energy was doubled up to 209 GeV, thanks to the installation of superconducting RF cavities. LEP was then focused on production of $Z^0 Z^0$ pairs and $W^+ W^-$ (Z^0 charged partners), and on the quest for new particles, in particular the Higgs boson.

In the LEP project, the civil engineering played for the first time an important role; LEP was in fact built in a 27 km tunnel, 100 metres underground, below the Jura Mountain and at the border of the Lemman Lake.

Even if LEP started operating in 1989, already a few years before its completion, in 1984, some physicists began to think about the possibility and the necessity of building a new accelerator in the same location, to accelerate protons instead of electrons and reaching the necessary energies and luminosity for a new physics.

1.2. THE LHC.

1.2.1. The reason for a new accelerator.

The understanding of our Universe has found important answers in the past century. Nevertheless, fundamental questions are still unsolved. Among them, the reason why elementary particles have masses is the most puzzling.

The Standard Model has in fact given us a full picture of the fundamental constituents of matter, of the forces acting between them and of the carriers of such interactions; it has also succeeded in unifying the electromagnetic and the weak forces in the electro-weak interaction, but it has up to now failed in providing the response to the fundamental problem of mass and to the Grand Unified Theory (GUT), according to which all four forces can be unified in a single "super force".

The explanation of the mass origin and the difference between masses of different particles may lie within the Standard Model, in an idea called the Higgs mechanism. According to this, the whole space is filled with a 'Higgs field', and by interacting with this field, particles acquire their masses. Particles which interact strongly with the Higgs field are heavy, whilst those which interact weakly are light. The Higgs field has at least one new particle associated with it, the Higgs boson. It is the main objective of LHC trying to identify such a particle. Several are the mechanism by which a Higgs boson could be generated in a particle interaction (the most favourable is the gluon-gluon fusion), but all of them suppose an energy range which is largely beyond what was attained with LEP, in the range of 1TeV.

Other important theories that could be investigated with the LHC are the SuperSYmmetry (SUSY), according to which each particle has a super-symmetric partner, the matter-antimatter unbalance (if matter and antimatter were both present at the origin of the Universe and in equal quantity, why has matter prevailed on the other?), the presence of dark matter or the existence of extra-dimensions. All these aspects will possibly find large space for discussion in particle physics at CERN in the next decades.

The choice for a new (proton) machine instead of the already available e^-e^+ collider resides in the fact that, when we try to accelerate particles on a circular orbit, they oppose this acceleration by emitting radiation (synchrotron light) in the direction of the original motion: the lighter the particle, the stronger the radiation. In fact, the power emitted is given by [Wille, 2006]:

$$P_s = \frac{e^2 c}{6\pi\epsilon_0 (m_0 c^2)^4} \frac{E^4}{\rho^2} \quad (1.1),$$

where m_0 , e and E are the mass, charge and energy of the particle; c is the speed of light, ϵ_0 the dielectric constant and ρ the bending radius.

For LEP, in its ultimate upgrade, 288 cavities, with a total accelerating voltage of nearly 3.7 GV, were needed to take particles' energy to 104 GeV; most of the energy gained per turn was nevertheless dissipated in the form of synchrotron radiation: 3% of the beam energy was lost per turn, which means that the energy provided to the particles was almost completely used to compensate the energy lost in the revolution.

Protons are 2000 times heavier than electrons; this is why they are the preferable candidate for high energy studies in circular machines: in LHC, 8 cavities per beam will provide an energy gain per turn of almost 500 keV, with only 7 keV lost because of synchrotron radiation, at collision energy. Moreover, protons are not elementary particles, but are made of quarks and gluons: a greater variety of possible interactions and a spectrum of energy values can be obtained than in elementary particle collisions.

1.2.2. The injection and acceleration chain.

The Large Hadron Collider [CERN, 2003] is being installed in the same tunnel as LEP, minimizing the costs for civil engineering. New underground areas had to be nevertheless excavated, to accommodate, in particular, the transfer lines for the two beams and the two new experiments. The whole underground complex is shown in Figure 1.1.

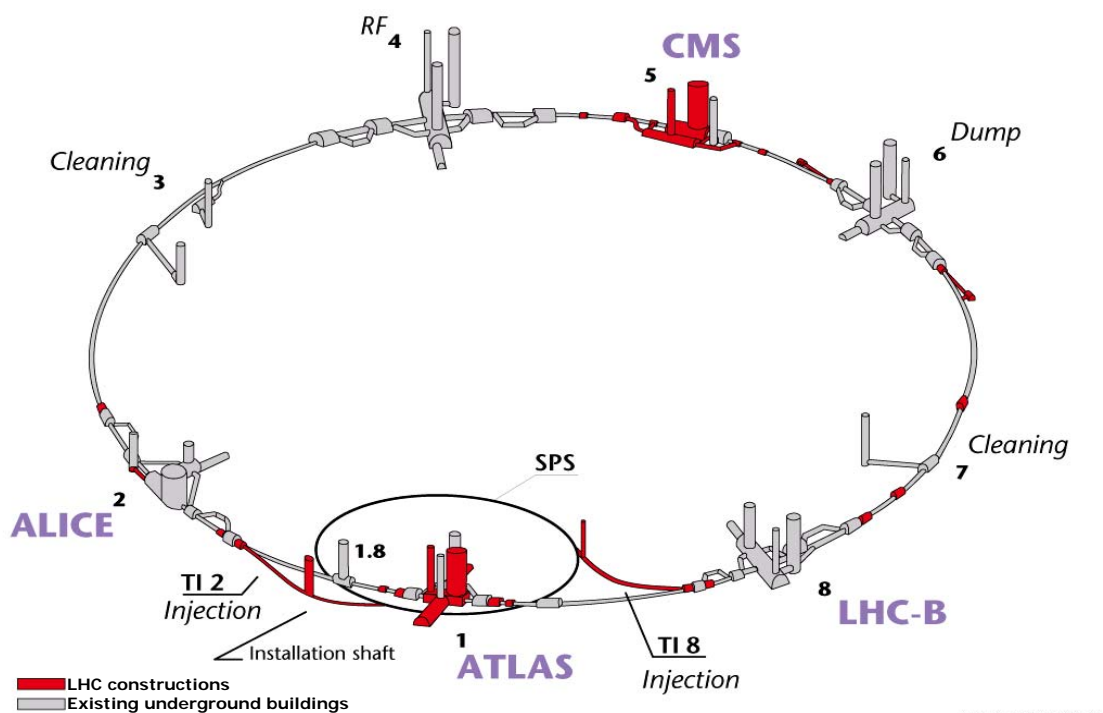


Figure 1.1_ Layout of the LHC tunnel, including new infrastructures.

LHC will also profit from the existing rings as injection chain for bunches of particles. The schematic of the accelerating chain is shown in Figure 1.2.

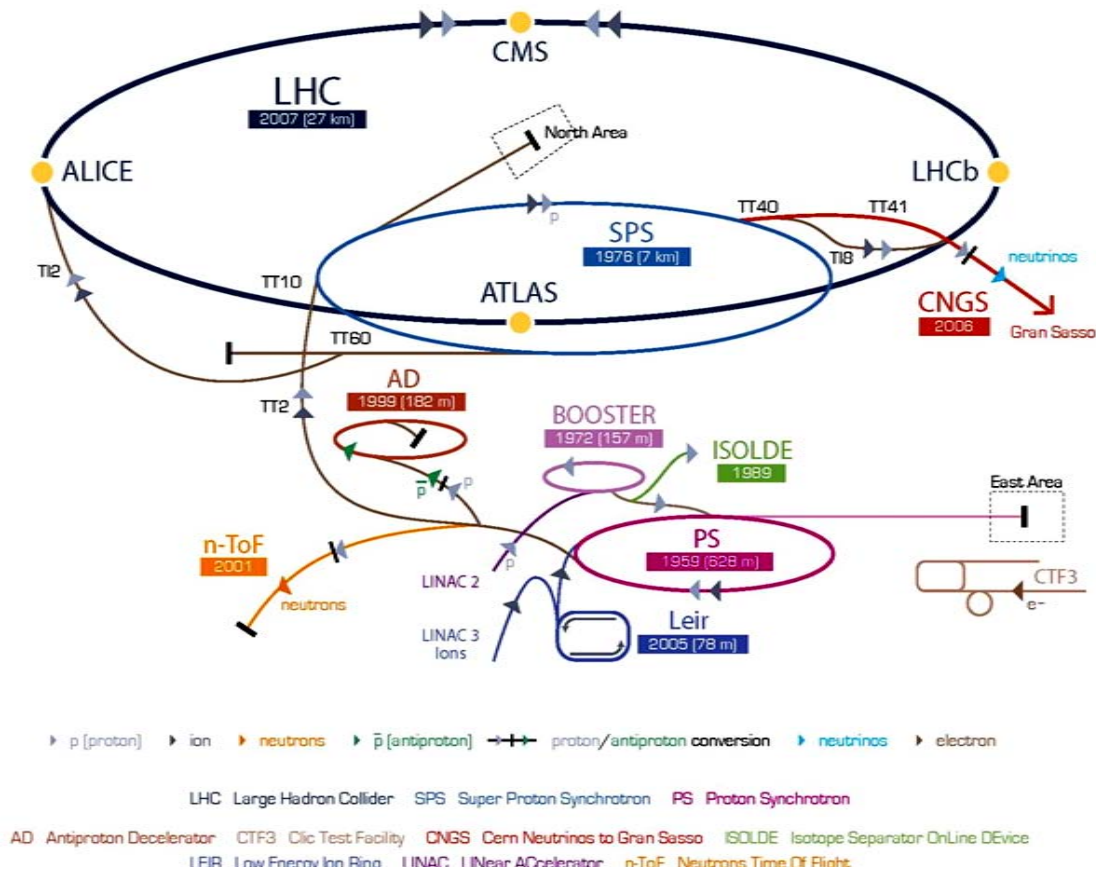


Figure 1.2_ CERN accelerator complex

Protons for the accelerator are taken from a standard hydrogen gas, where orbiting electrons are stripped off hydrogen atoms. Protons are then injected into the PS Booster (PSB) at energy of 50 MeV from Linac2. The booster accelerates them to 1.4 GeV. The beam is afterward fed to the Proton Synchrotron (PS) where it is accelerated to 25 GeV, after which it is sent to the Super Proton Synchrotron (SPS) where the protons are accelerated to 450 GeV. They are finally transferred to the LHC, both in a clockwise and anticlockwise direction (the filling time is 4'20'' per LHC ring), where they are accelerated for 20 minutes to their nominal 7 TeV energy.

Because of the way in which they are produced, the protons circulate in the LHC machine in *bunches*, packets of particles which fill the ring with a 7 m distance between one another. In nominal operating conditions, the number of bunches is 2808, with a number of particles per bunch of nearly 10^{11} protons.

Salient machine parameters are listed in Table 1.1, together with the peak luminosity, which is the number of collisions per second per square centimeter.

TABLE 1.1 _ LHC BEAM PARAMETERS AND PEAK LUMINOSITY.

		Injection	Collision
Beam Data			
Proton energy	[GeV]	450	7000
Relativistic gamma		479.6	7461
Number of particles per bunch		1.15×10^{11}	
Number of bunches		2808	
Longitudinal emittance (4σ)	[eVs]	1.0	2.5
Transverse normalized emittance	[$\mu\text{m rad}$]	3.5	3.75
Circulating beam current	[A]	0.582	
Stored energy per beam	[MJ]	23.3	362
Peak Luminosity Related Data			
RMS bunch length	[cm]	11.24	7.55
RMS beam size at the IP1 and IP5	[μm]	375.2	16.7
RMS beam size at the IP2 and IP8	[μm]	279.6	70.9
Geometric luminosity reduction factor F		-	0.836
Peak luminosity in IP1 and IP5	[$\text{cm}^{-2}\text{sec}^{-1}$]	-	1.0×10^{34}
Peak luminosity per bunch crossing in IP1 and IP5	[$\text{cm}^{-2}\text{sec}^{-1}$]	-	3.56×10^{30}

The reason for bunched distribution of particles also lays on the way particles are accelerated, which is by means of RF cavities. In fact, when a group of particles is crossing a cavity, only those in phase with the RF signal will be accelerated, while the others will be slowed down. For the LHC, in particular, superconducting cavities will be used, that permit small energy losses and large stored energy. Eight cavities per beam will be installed, each delivering 2 MV (an accelerating field of 5 MV/m) at 400 MHz. The cavities will operate at 4.5 K and will be grouped by four in cryo-modules, with two cryo-modules per beam [Boussard, 1999].

In a second phase, LHC will also accelerate lead ions, produced from a highly purified lead sample heated to a temperature of about 550 °C. The lead vapor is ionized by an electron current. Many different charge states are produced with a maximum around Pb27+. These ions are selected and accelerated to 4.2 MeV/u (energy per nucleon) before passing through a carbon foil, which strips most of them into Pb54+. The Pb54+ beam is accumulated and then accelerated to 72 MeV/u in the Low Energy Ion Ring (LEIR), which transfers them to the PS. PS accelerates the beam to 5.9 GeV/u and sends it to the SPS after first passing it through a

second foil where it is fully stripped to Pb82+. SPS further accelerates the beam to 177 GeV/u then sends it to the LHC, which accelerates it to 2.76 TeV/u.

1.2.3. The machine layout.

In LHC, two counter-rotating proton beams will be accelerated from the injection energy of 0.45 TeV up to a flat top energy of 7 TeV, at which collisions take place for about 10 hours. The two beams will circulate in separate pipes, 194 mm apart, for most of their travel along the accelerator; in four points, their orbit converge, in correspondence of the interaction regions, where the beam cross and exchange trajectories.

The sectoring of LEP has been clearly preserved in LHC: the new accelerator (as shown in Figure 1.1) is, in fact, subdivided in eight sectors, separated by an equal number of straight sections, 528 m long, used as experimental or utility sections. Since the shape of LHC is almost circular, it is mainly filled with dipoles (1232 superconducting dipole magnets are used in the arcs), to keep the particles on their orbit. According to the Lorentz force equation

$$\vec{F} = q \cdot (\vec{E} + \vec{v} \times \vec{B}) \quad (1.2),$$

we need, in fact, dipolar fields perpendicular to the direction of motion to bend the particles along the curvilinear trajectory. Electric fields could also be used to bend relativistic particles, but high intensity electric fields, with an associated bending force comparable to that of the most traditional magnets, are not available^a.

Magnetic fields are as well used to focus the two beams, especially in the vicinity of the interaction points, or to steer the beam: quadrupoles and correctors of various orders are installed all along the machine with this aim.

If we look in detail at the components of an arc, we can recognise elementary blocks, called cells, which are 106.9 m long: 23 regular cells are contained in an arc. Every half cell contains one 5.4-m-long cold-mass (6.6-m-long cryostat) short straight section (SSS) assembly and three 14.3-m-long dipole magnets. These are the main elements of an LHC regular cell, which is schematically represented in Figure 1.3.

As it will be shown in more details in the next chapter, dipoles and quadrupoles incorporate both beam pipes in a two-in-one aperture design. For the dipoles, both apertures are powered in series and all dipole magnets in an arc form one electrical circuit. On the contrary, the quadrupoles of each arc form two electrical circuits: all focusing quadrupoles of Beam 1 and Beam 2 are powered in series; the same for the defocusing quadrupoles of both beams.

^a For a magnetic field of 1 T, an electric field, exerting on a relativistic particle an analogous Lorentz force, should have an intensity of 300 MV/m, which is presently out of technology capabilities.

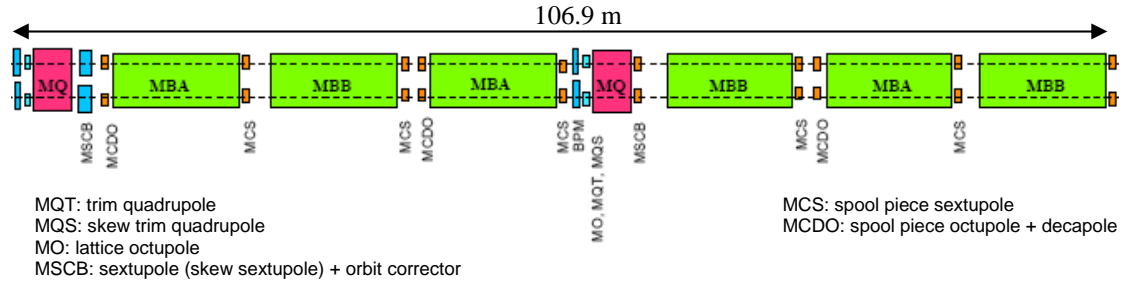


Figure 1.3_ LHC regular cell.

A number of corrector magnets are also installed in the arcs, as shown in Figure 1.3: the lattice corrector magnets, on both sides of the quadrupole assembly (trim and skew trim quadrupoles, lattice octupoles and sextupoles plus orbit correctors), and the spool-piece corrector magnets, which are thin non-linear magnets attached at the extremities of the dipoles (spool-piece sextupoles, octupoles and decapoles).

The transition between each arc and the long straight section (LSS) is realized through the dispersion suppression regions, made by two LHC cells with missing dipoles, and quadrupoles magnets which are not powered in series with those of the arcs. The dispersion suppressors are used to adapt the LHC reference orbit to the geometry of the LEP tunnel, to cancel the horizontal dispersion arising in the arc and generated by the separation/recombination dipoles, and to help in matching the insertion optics to the periodic solution of the arc.

To complete the description of the whole machine, the LSSs containing experiments (InsertionRegion1, 2, 5, 8) are almost identical and comprise four matching quadrupoles, recombination/separation dipoles and the 31-m-long low- β triplet assembly; the triplet contains 4 single bore, large aperture (70 mm) quadrupoles MQX (produced by KEK in Japan and FNAL in the USA) which are powered by nested power converters [Lamm, 2005]. The remaining LSSs contain the momentum cleaning system (IR3), the betatron cleaning (IR7), the radiofrequency system (IR4) and the dumping system (IR6), where the beams, in case of need, can be fast-extracted and dumped on a 750-m-far absorber block [Goddard, 2003].

In summary, LHC contains in total 1232 main dipoles (of which 1104 in the lattice and 128 in the Dispersion Suppression (DS) sections), 392 main quadrupoles (360 in the lattice and 32 in the DS), 86 superconducting quadrupoles in the matching/DS sections (MQM), 26 wide aperture quadrupoles (MQY), 32 MQX and 20 special dipoles for beam separation, and more than 7600 superconducting corrector magnets.

Whilst the total energy in each beam at maximum energy is about 360 MJ (which is about as energetic as a 400 t train, like the French TGV, traveling at 150 km/h), the total consumption is around 120 MW which corresponds more or less to the power consumption for households in the Canton of Geneva.

1.3. FOUR GIANTS ... AND A HALF: THE EXPERIMENTS.

As in the case of its predecessor, LHC will host four underground experimental areas, two of them positioned, nevertheless at different locations from LEP experiments: ATLAS (A Toroidal LHC ApparatuS) and CMS (Compact Muon Solenoid) are being in fact installed at point 1 and 5 and two big caverns (Figure 1.1) had to be built on purpose. These are moreover the biggest and most impressive experiments of LHC. The other experiments installed at the LHC are: A Large Ion Collider Experiment (ALICE, being installed at point 2), Large Hadron Collider beauty experiment (LHCb, at point 8) and TOTal Elastic and diffractive cross section Measurement (TOTEM). Different from the others, TOTEM will not have a proper cavern, but will be installed near the CMS interaction point and will have detectors in three different locations along the vacuum chamber of the LHC.

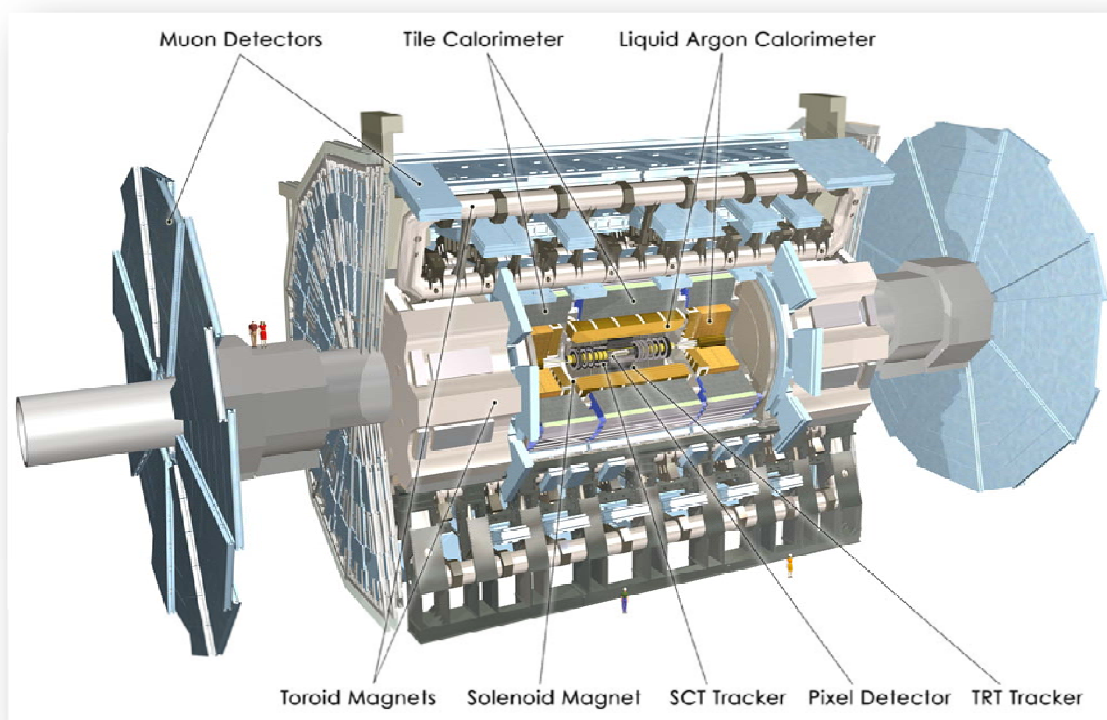


Figure 1.4_ ATLAS experiment with a detailed view of its components.

ATLAS [ATLAS Collaboration, 1994] is a general purpose detector designed to cover the widest possible range of physics at the LHC, from the search for the Higgs boson to supersymmetry (SUSY) and extra dimensions. With its 46 m in length and 25 m in diameter (see Figure 1.4), it will be the largest-volume collider detector ever constructed. Its weight is also remarkable: nearly 7000 tons. The eight superconducting coils, which are 26 m long and 5 m wide, will produce a toroidal field of 4 T. Nearly 2000 persons have participated to the realization of ATLAS, from more than 150 institutes all over the world.

CMS [CMS Collaboration, 1994] is also a general purpose detector with the same physics goals as ATLAS, but different technical solutions and design (see Figure 1.5). It is built around the world's largest superconducting solenoid, producing a uniform magnetic field of 4 T in a free inner space of 5.9 m in diameter and 13 m in length. Its total weight is around 12500 tons. More than 2000 people work for CMS, from nearly 200 institutes.

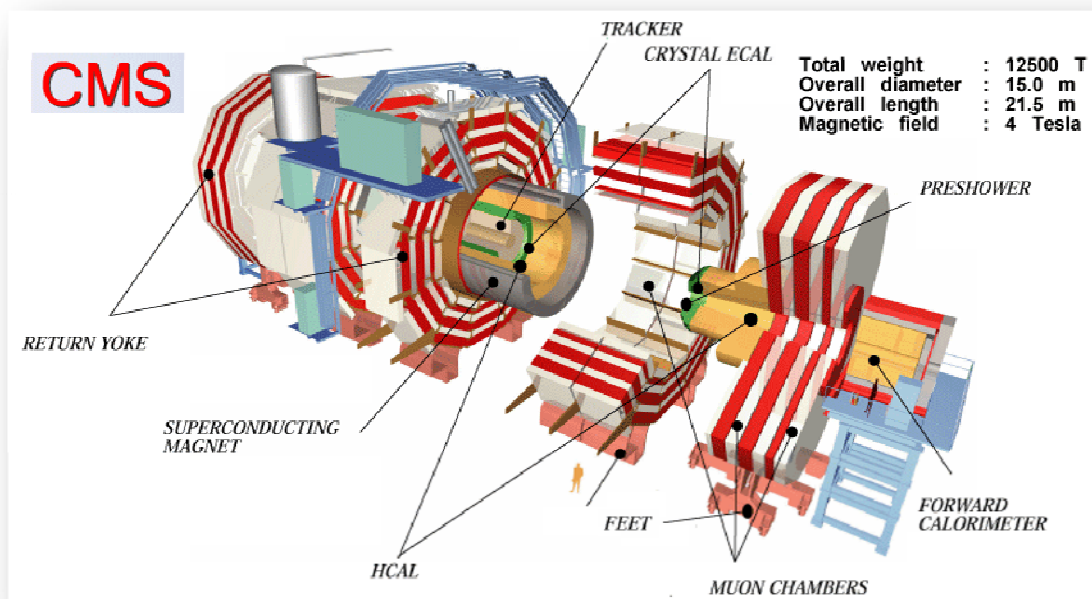


Figure 1.5_ The various slices and components of CMS.

ALICE [ALICE Collaboration, 1995] is a detector specialized in analysing lead-ion collisions. It will study the properties of quark-gluon plasma, a state of matter where quarks and gluons, under conditions of very high temperatures and densities, are no longer confined inside hadrons. Such a state of matter probably existed just after the Big Bang, before particles, like protons and neutrons, were formed.

LHCb [LHCb Collaboration, 1998] will specialize in the study of the slight asymmetry between matter and antimatter present in interactions of B-particles (particles containing the b quark). Understanding it should prove invaluable in answering the fundamental question: “Why is our Universe made of the matter we observe?”

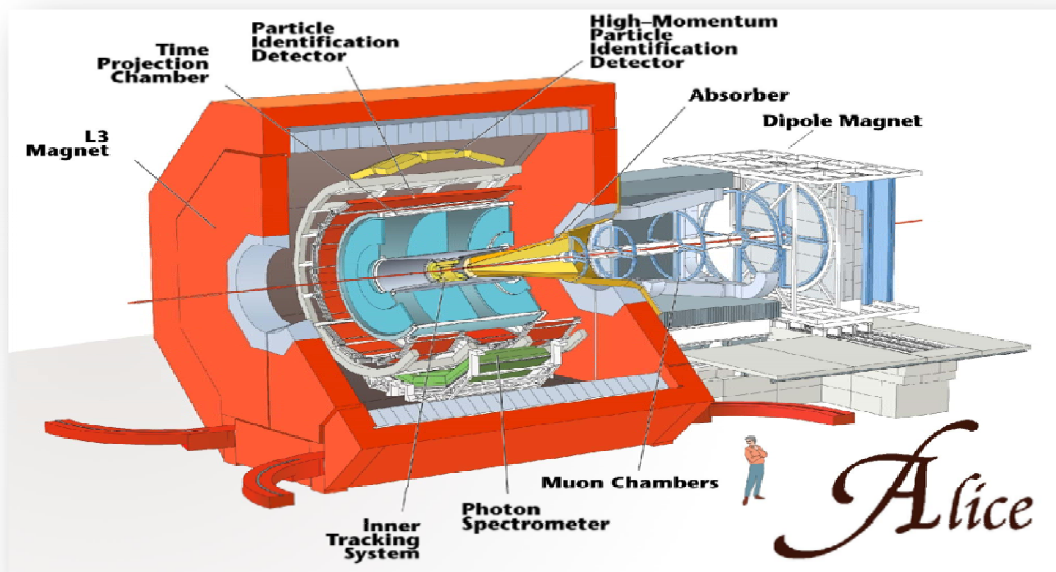


Figure 1.6_ ALICE with a detailed view of its components.

TOTEM will measure the effective size of the proton at LHC. It follows a long-standing tradition at CERN by measuring the effective size or cross-section of particles, especially protons. The TOTEM experiment, modest in size compared to the other LHC experiments, will be installed near the interaction point used by CMS. It will have detectors in three different locations. In particular, silicon sensors will be installed in special sections of the vacuum chamber in the LHC tunnel some 200 m away from CMS.

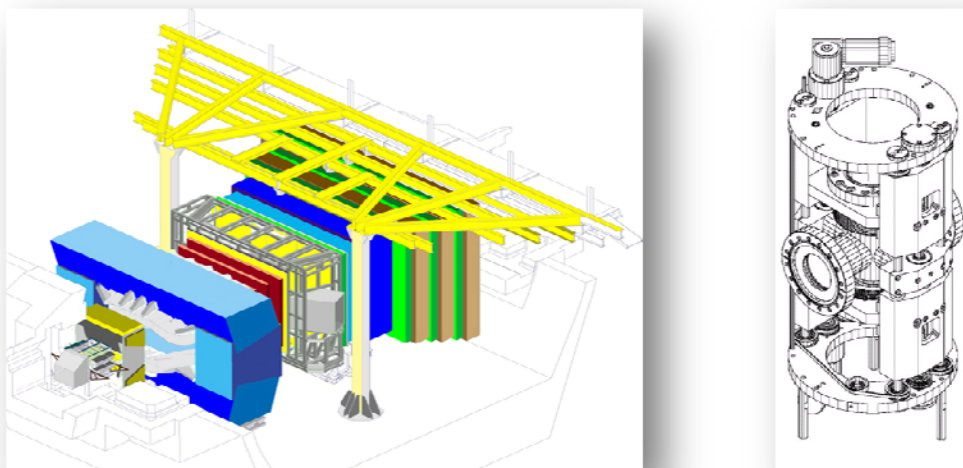


Figure 1.7_ LHCb experiment (on the left) and the small TOTEM (on the right).

BIBLIOGRAPHY

- ALICE Collaboration, “*ALICE Technical Proposal*”, CERN-LHCC-95-71.
- ATLAS Collaboration, “*ATLAS Technical Proposal*”, CERN-LHCC-94-43.
- Boussard D., Linnecar T., “*The LHC Superconducting RF System*”, Cryogenic Engineering and International Cryogenic Material Conference, Montreal, Canada (1999), and LHC Project Report 316.
- CMS Collaboration, “*CMS Technical Proposal*”, CERN-LHCC-94-38.
- Goddard B., Gyr M. and Uythoven J., “*LHC Beam Dumping System: Extraction Channel Layout and Acceptance*”, CERN-LHC Project Report 654 (2003).
- Lamm M.J., “*US Accelerator Contribution to the LHC*”, Proceedings of 2005 Particle Accelerator Conference, Knoxville, Tennessee, 184-188 (2005).
- LHC Design Report, Vol. I “*The LHC main ring*”, CERN-2004-003, June 2004.
- LHCb Collaboration, “*LHCb Technical Proposal*”, CERN-LHCC-98-004.
- Rabi I., from a resolution of UNESCO (1950).
- Rubbia C., “*The discovery of the W and Z bosons*”, Phys. Rep. 239 (1994) 241-284.
- Wille K., “*Synchrotron Radiation*”, Joint Universities Accelerator School, Archamps (2006).

CHAPTER 2

THE LHC DIPOLE MAGNETS

2.1. AT THE EDGE OF TECHNOLOGY.

2.1.1. The need for superconducting magnets.

LHC makes an extensive use of the superconducting technology. It is not the first example, but it is certainly the one where NbTi has been used to its optimum capabilities: the LHC dipole magnets are in fact able to produce a magnetic field of up to 9 T, in a central aperture of 56 mm. Only superconducting magnets can generate such an intense magnetic field (a standard iron yoke magnet cannot normally generate a magnetic field of more than 2 T, due to the saturation of the iron). But why the superconducting magnets have been used in LHC?

If we take equation (1.2) and suppose that a particle is moving under the effect of a uniform magnetic field only, perpendicular to its trajectory, we may write:

$$\vec{F} = q \cdot \vec{v} \times \vec{B} \quad (2.1).$$

Comparing the intensity of the Lorentz force with the centripetal force on a circular orbit of radius ρ , we get:

$$qvB = \frac{mv^2}{\rho} \quad (2.2).$$

Simplifying and expressing the particle momentum in GeV/c, we obtain:

$$B\rho[Tm] \approx \frac{p[GeV/c]}{0.3} \quad (2.3).$$

$B\rho$ is called the *magnetic rigidity* and measures beam's stiffness in the bending field. From equation (2.3), if we want to increase the energy of the particle, either we increase the bending radius or we increase the magnetic field. Since, for LHC, the radius was imposed by the LEP tunnel, the only way to increase the energy, while keeping the particles on their orbit, was to increase the magnetic field.

The choice of the superconducting material, to be used in winding the magnets, fell on the most reliable and easy-to-produce NbTi. This can be considered a conservative solution, if we think, for example, of the better performance of Nb₃Sn^a, but it represented in any case both an innovation with respect to the energy levels of other accelerators (see, for comparison, the data relative to the most important accelerators in Table 2.1) and a challenge despite the contemporary failure of a less ambitious project (SSC was in fact planning to use a magnetic field of 6.79 T in a simpler magnet structure).

^a The relative performance of these two types of superconductors will be treated in more details in the next paragraph.

TABLE 2.1 _ MAIN PARAMETERS OF MOST IMPORTANT PROTON MACHINES [RUSSENSCHUCK, 2005].

Accelerator	Tevatron (USA)	HERA (Germany)	UNK (Russia)	SSC (USA)	RHIC (USA)	LHC (CH)
Laboratory	FNAL	DESY	IHEP	SSCL	BNL	CERN
Commissioning	1983	1990	cancelled	cancelled	2000	2007-8
Circumference (km)	6.3	6.3	21	87	3.8	27
Proton beam energy (TeV)	0.9	0.82	3.0	20	0.1	7.0
Nominal dipole field (T)	4.0	4.68	5.0	6.79	3.4	8.33
Number of dipoles per ring	774	416	2168	3972	264	1232
Aperture (mm)	76.2	75	70	50	80	56
Magnetic length (m)	6.1	8.8	5.8	15	9.7	14.3
Filling factor	0.75	0.58	0.59	0.68	0.67	0.65

2.1.2. Fundamentals of superconductivity.

The importance of superconductivity in modern physics is today widely recognized. Since its discovery in 1911 by Kammerlingh Onnes it has found plenty of applications, not last in magnets for accelerators. As stated in [Rossi, 2007] and [Wilson, 1999] accelerators and superconductivity have been good companions for many years, from the first large scale application (the Argonne bubble chamber) to the present, never before achieved, applications in the giant and most powerful ATLAS and CMS.

It is not within the scope of this thesis to provide the reader with an exhaustive explanation on the phenomenology and the theoretical origin of superconductivity (for this, we send the reader to specialised works, as [Rose-Innes, 1969] and [Wilson, 1983]), but the sake of comprehension imposes nevertheless to introduce the fundamentals of this discipline.

First of all, when we speak about superconductivity we refer to the physical phenomenon by which a material, under certain conditions, presents a zero resistance and the capacity of expelling a moderate magnetic field from its interior. If we imagine a 3-dimensional space where temperature, current density and magnetic field are the main axes, a superconductor would keep its non-conventional characteristics only when its coordinates don't overcome a critical value; all possible combinations of these values define a surface (called *critical surface*), inside which the superconductor may conduct current without dissipation. Outside the critical surface, the material becomes normal conducting or not conducting at all. The transition from one state to the other is normally called a *quench*.

The superconducting materials which have found large applications in physics, because of their capacity of conducting very high current densities, belong to the so-called type-II family,

mainly characterized by a composite material and a mixed state. The best known superconductors of this family are NbTi and Nb₃Sn, whose characteristics in terms of critical current density versus magnetic field are shown in Figure 2.1, together with those of the most used companions.

The commonly used NbTi has a critical temperature of 10 K and a critical magnetic field of about 14.5 T, well below those of Nb₃Sn, that can have an extrapolated magnetic field of up to 30 T in industrial samples. The latter presents nevertheless a limitation: after the heat treatment, which produces the metallic compound, the result is a material extremely brittle and sensitive to stress, which limits its applications, especially in winding magnets^b. For its economical advantage and its ductility, NbTi was therefore selected to build the LHC magnets. The enormous progress done in production of cables and in stress management for Nb₃Sn magnets, have nevertheless recently raised the possibility for an upgrade of the LHC based on this technology (see for example [Devred, 2005]).

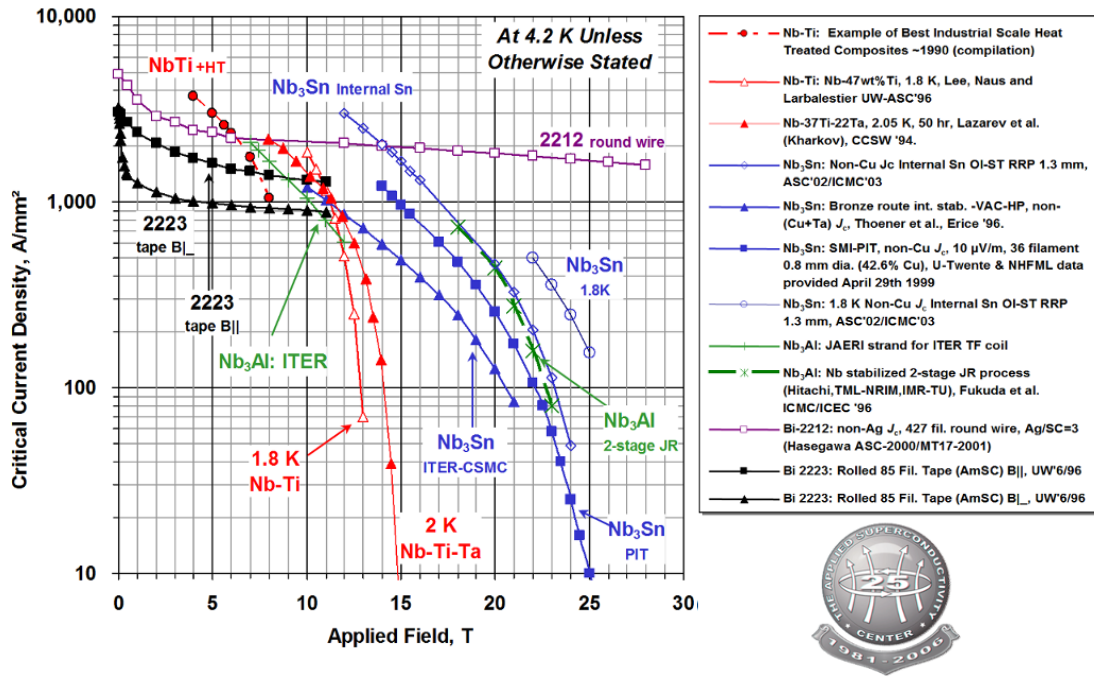


Figure 2.1 _ Superconductors for accelerators: status of the art.

A different attention has to be given to the High Temperature Superconductors (HTS), that show critical temperature and magnetic field well above those of NbTi and Nb₃Sn. LHC represents the first large scale application of these superconductors in an operating device, by using 1180 current leads, all based on Bi-2223. The HTS are nevertheless not yet well developed to be used in winding magnets, both for the cost of the production as for the incapacity of production in long pieces.

^b The problem may be reduced by applying the *wind-and-react* technique instead of the traditional *react-and-wind* one.

2.1.3. Why superfluid helium.

It appears evident that there is a pay-off in winding magnets with superconducting material: the need for cooling down the whole structure to very low temperatures.

As already mentioned, the critical temperature of NbTi at zero field and current is nearly 10 K. The only practical coolant which is liquid at this temperature is helium, whose boiling point is equal to 4.2 K; this is why He is used to cool-down the LHC magnets. Moreover, magnets in arcs, dispersion suppression regions and inner triplets will be immersed in a pressurized bath of *superfluid helium* at about 1.3 bars and a maximum temperature of 1.9 K. The reason is double. First of all, at 1.9 K, NbTi has a critical current curve versus magnetic field enhanced by 3 T, with respect to the 4.2 K status; the actual gain in field that can be obtained in a magnet is 2 T. Secondly, at 1.9 K, He possesses peculiar characteristics, the most amazing of which is the absence of viscosity; superfluid helium can permeates the smallest interstices, thus improving the, otherwise low, global heat transfer. In fact, the specific heat of superconducting alloys and their copper matrix reduces abruptly with decreasing temperature and the use of superfluid helium is of great advantage.

Moreover, as shown in Figure 2.2, the thermal conductivity of helium has a clear maximum around 1.9 K, around 3000 times larger than that of cryogenic-grade OFHC copper: superfluid helium may have a powerful stabilising action on thermal disturbances.

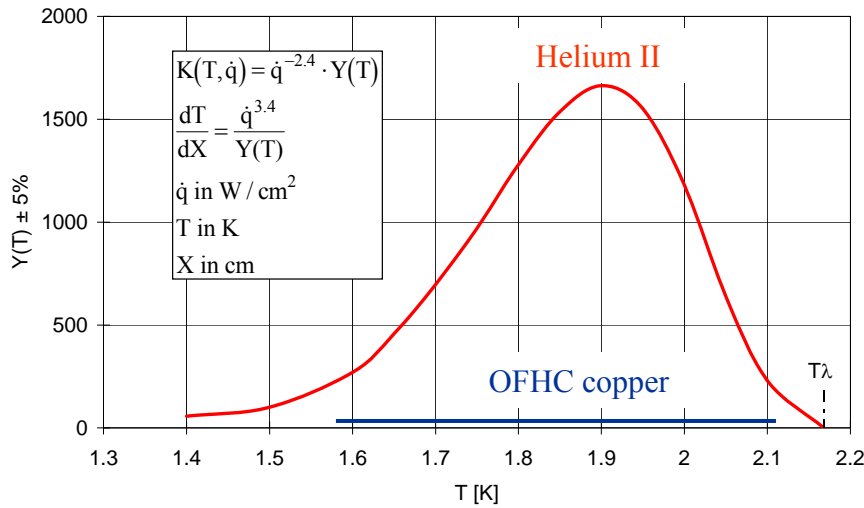


Figure 2.2 _ Effective thermal conductivity of superfluid helium versus OFHC [Bon Mardion, 1979].

120 tons of helium will be needed for cooling the LHC and 32 MW will be the total electric consumption of the complex cryogenic system [CERN, 2004] and [Gubello, 2006]. In Figure 2.3, a section of the cryogenic distribution system and the superconducting magnets is shown, together with the operating temperatures of the different pipes and components.

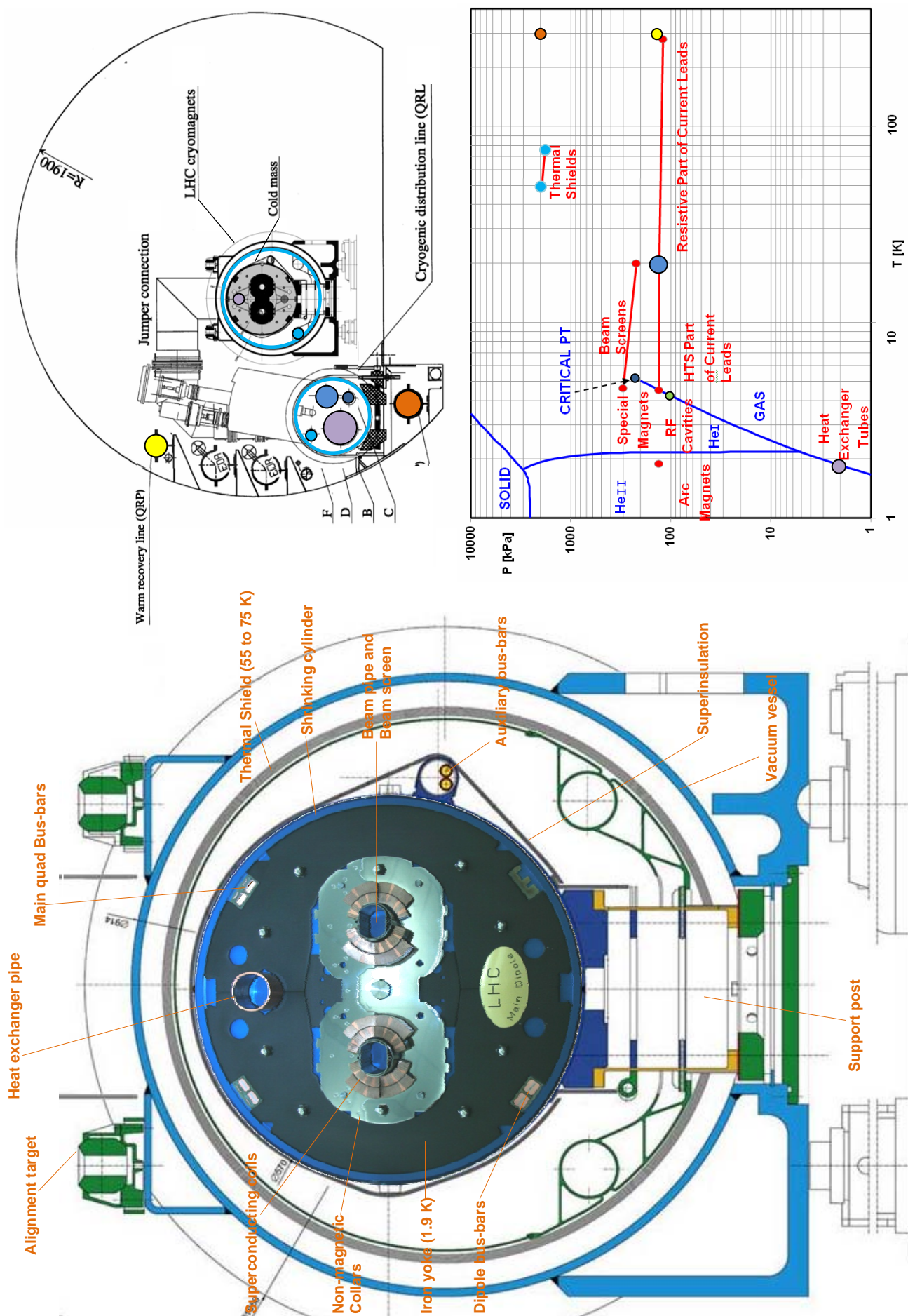


Figure 2.3 _ Cross-section of the LHC dipole and scheme of the cryogenic system plus details of the operating temperatures shown on the He phase diagram.

2.2. TEN YEARS OF MAGNET DEVELOPMENT.

2.2.1. The R&D program.

A total of 1232 dipole magnets will be used in the accelerator, which fill more than 2/3 of the ring, providing a magnetic field, at nominal collision energy, of 8.33 T; the possibility of running up to an ultimate field of 9 T is also offered by these magnets. Due to the machine design (the series connection of all dipoles, in particular), the poor performance of one dipole cannot be compensated by better performance of another one: the weakest dipole will eventually determine the energy performance of the whole machine. As it will be also shown in chapter 4, instead of getting excellent performance in few components, the effort was therefore concentrated in having a uniform production, with a bending strength of all magnets equal to within ~ 100 ppm; this was not an easy task, also because the magnets were built by three different producers, but the goal was achieved through a detailed and rigorous quality assurance program on magnet (see chapter 4) as well as on cable productions. The critical current density of all cables was measured [Verweij, 2007] and proven to be conform to specifications, together with a reduced magnetization, the absence of defects and a controlled inter-strand resistance. A review on the R&D activity and the provision of the nearly 7400 km of superconducting cables is presented in [Leroy, 2006].

For what concerns the LHC dipoles, they found their definitive shape after several years of development, between 1988 and 2001. The necessity of accommodating the magnets in a limited space finally lead to the so-called two-in-one configuration, where the apertures for the two counter-rotating beams are hosted inside the same mechanical structure; this is used not only as a magnetic flux confinement region, but also to support the associated enormous electromagnetic forces. The investigation of this and other technical issues required the construction of several short models and full scale prototypes, which served to refine the mechanical and magnetic design; three generations of geometry were developed, which mainly differ on the number of the coil blocks, the width of the cables used, the material of the collars and the length of the cold mass. In particular [LHC Design, 2004], the first generation was using an electro-magnetic design with six coil blocks per quadrant, around a 50 mm bore, and the two layers were wound with a 17-mm-wide cable; the collars were in aluminium alloy and the cold mass length was 10 m. This generation of prototypes ended successfully and the first three dipoles would have been perfectly acceptable for the machine, according to the present technical specifications. However, the design was changed, before they were even tested, because of a change in the bore aperture, from 50 to 56 mm, and the consequent reduction of the cable width, moved to 15 mm. These modifications, together with a change of coil block number from six to five, led to a reduction of the central field and to a consequent compensating increase of magnet length, brought to 15 m. The results provided by this second generation were lower than expected; this is why further changes were applied to dipole cross-section and magnetic design.

2.2.2. The final design.

With the third and last generation [Wyss, 1999], a pre-series production of 30 dipoles was assigned to each of the three producers at the end of 1999, which ended up with the series production of all dipoles. A schematic view of final design LHC dipole is shown in Figure 2.4, with a detailed description of the main components of the magnet. The list of the main parameters characterizing these magnets is also shown in Table 2.2.

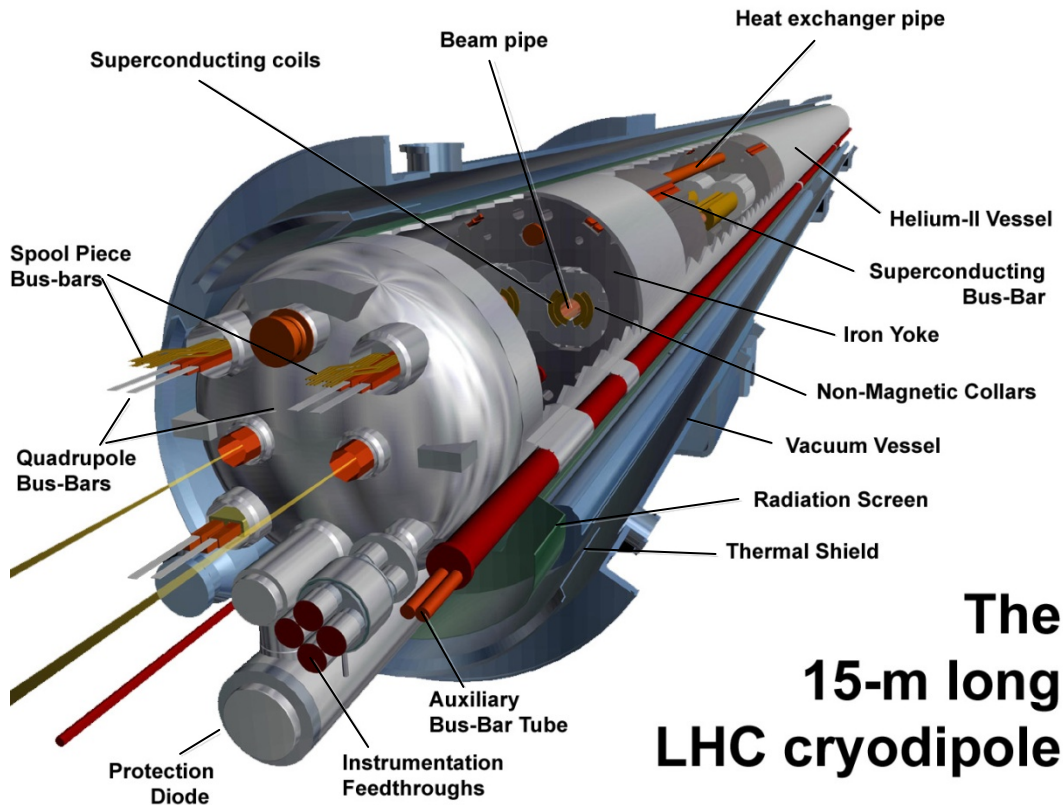


Figure 2.4 _ Schematic view of the LHC dipole.

With respect to the previous generation, the final design goes back to the six blocks structure, with a better block distribution, leading to a partial reduction of the quench^c activity. The cables used for the coils are 15.1 mm wide, for both outer and inner layer, but with different thickness in the two layers, and also dissimilar filament and strand diameter, number of filaments and strands, copper-to-superconductor ratio and critical current (see Table 2.2). A cross-section of the LHC dipole is shown in Figure 2.3.

^c The definition of quench for a magnet will be given in chapter 4, whilst the statistical treatment of quenches for the LHC dipole magnets will be provided in chapter 5.

TABLE 2.2 _ MAIN PARAMETERS OF THE DIPOLE COLD MASS.

	Value		Unit
Injection (nominal) field - 0.45(7) TeV beam energy	0.54 (8.33)		T
Current at injection (nominal) field	763 (11850)		A
Inductance at nominal field	98.7		mH
Stored energy (both apertures) at nom.(ult.) field	6.93 (8.11)		MJ
Ultimate field	9.00		T
Current at ultimate field	12840		A
Maximum quench limit	9.7		T
Operating temperature	1.9		K
Magnetic length at 1.9 K and nominal field	14312		mm
Distance between aperture axes at 1.9 K	194.00		mm
Cold mass sagitta at 293 K	9.14		mm
Bending radius at 1.9 K	2803.98		m
Total mass	27.5		t
Inner coil diameter at 293 K	56.00		mm
Strand	Inner layer	Outer layer	
Diameter	1.065	0.825	mm
Copper to superconductor ratio	1.65	1.95	-
Filament diameter	7	6	μm
Number of filaments	~8900	~6500	-
RRR	≥ 150	≥ 150	-
Critical current [at 1.9 K and 10T(in)/9T(out)]	≥ 515	≥ 380	A
Cable			
Number of strands	28	36	-
Mid-thickness at 50 MPa	1.900	1.480	mm
Thin edge	2.064	1.598	mm
Width	15.10	15.10	mm
Inter-strand cross contact resistance	≥ 15	≥ 40	$\mu\Omega$
RRR	≥ 70	≥ 70	-
Critical current [at 1.9 K and 10T(in)/9T(out)]	≥ 13750	≥ 12960	A

Looking at Figure 2.3, it is possible to distinguish the 6 blocks of cables separated by copper wedges and split into two layers. A detailed description of all components is given in Appendix 1, where the assembly of the cold mass, till the pre-collaring phase, is described. The superconductor layers are blocked and kept in position with austenitic steel collars, which are common for the two apertures. Around the collars, the laminations of the iron yoke are

also supporting the cryogenic pipes and the bus-bars for other magnets. The whole magnet length is curved with a slight sagitta (9 mm over the entire length) by welding curved half-shells in a press. After adding several layers of MLI (multi layer insulation) around the cold mass, the two supporting posts (which are composite structures with a high mechanical resistance and low thermal conduction) are installed and the structure is then cryostated.

The magnetic length is conclusively fixed to 14.3 m. The two big changes, with respect to previous models, are the presence of nested laminations on the extremities and the use of austenitic steel collars (see below). Near the magnet ends, for 370 mm, the laminations are composed of an outer shell of low carbon steel, like the main body, and with an inner shell, 20 mm thick of special austenitic steel. The latter is non magnetic and its mechanical properties, namely the thermal contraction, have been selected in order to fit exactly that of the iron. These nested laminations, are designed to lower the peak field on the coil end (always a quench risk region) while preserving the maximum magnetic length and reducing the quadrupole field component coming from aperture coupling at the end.

For what concerns the austenitic steel collars, their material has a very low magnetization ($\chi_m < 0.005$) under operating conditions [Bajko, 2000] and they are obtained by fine blanking according to a shape that ensures the wanted coil cavity under stress and cold conditions. With respect to the previous aluminium version, the austenitic steel collars allow a more comfortable margin in the construction and assembly tolerances [Fessia, 1999]. And by means of their rigidity, they mainly contribute in limiting conductor movements: an important issue in superconducting magnets, both for beam dynamics considerations and for magnet stability concerns. Since magnet stability is the key argument at the basis of this thesis, elucidating this point is compulsory.

Regarding beam dynamics, it is evident that, for superconducting magnets, the proper cable positioning is fundamental for a stable beam. In fact, differently from the traditional resistive magnets, where the conductors are distant and the shape of the magnetic field is dominated by the machining of the iron yoke, in superconducting magnets, the conductors are placed close to the bore in order to reach a high magnetic field in the region where the beam passes: the shape and the quality of the magnetic field strongly depends on the position of the conductors. This is the reason why the magnetic field errors must be controlled at levels of the order of less than 10^{-4} of the main field. This means that the position of the conductors must be controlled with a precision of tens of μm .

For the same reason, the conductors must be constrained during the ramp-up of the magnetic field. In fact, the high magnetic field provokes strong Lorentz forces, which increase with the square of the field. If the stress applied to the conductor was not enough to guarantee that its position is maintained unchanged during the powering of the magnet, the position of the conductors, and hence the magnetic field quality, would change during the ramp-up of the current. On the contrary, the stress exerted on the conductor cannot be too high, to prevent damages to the conductor as well as to its insulating layers. Managing the stress is therefore crucial during the different phases of the life of a magnet: the assembly, the

cool-down and its powering. The mechanical rigidity of the components has to be selected with care, in the same way as their relative thermal contraction has to be kept into account.

Identical remarks on conductor mechanical stability must be extended to the thermodynamic stability of magnets. In fact, due to the poor presence of stabilizer, to the very high current density and to the small operational margin^d, the quench energy for the LHC dipoles is very small, ranging from tens of μJ to mJ [Ghosh, 1999]. In such conditions, even the energy released by the friction generated in tiny movements of a few μm can trigger a quench [Iwasa, 1992]. The conductors must be, therefore, perfectly constrained inside their mechanical structure, and their compaction has to be assured.

Conductor positioning and coil stresses are consequently fundamental for an optimised field quality and acceptable quench performance.

It appears now evident that collars and collaring procedure play a relevant role in magnet manufacturing. They have been carefully optimised to have an average compression of about 70 MPa for the inner layer and 75 MPa for the outer one at the end of the process; to obtain such values, the coils are compressed up to 115 to 135 MPa during the collaring process. At ambient temperature also the iron yoke participates in keeping under stress the collared coils. The iron yoke is split in two in the plane of vertical symmetry; it is made of 6-mm-thick low-carbon-steel laminations and it is used for flux return, but it also adds about 15% to the field^e. Welding the shrinking cylinder, the iron yoke vertical gap is closed and the cylinder is welded with a tensile stress of 150 MPa; this stress is increased during cool-down, reaching a value of 335 MPa. At cryogenic temperatures, nevertheless, the contact between collars and yoke is almost lost due to the different thermal contractions of the materials. The pre-stress in the coil decreases by between 25 MPa and 40 MPa, as a result of the higher contraction of the coils with respect to the collars. During excitation, the coils reach minimum compression at their top ($\sim 5 \text{ N/mm}^2$) increasing at the mid plane up to $\sim 70\text{-}80 \text{ MPa}$. It is, in this case, the iron yoke which limits, with its contact, the deformation of the coils, thus avoiding the appearance of unwanted harmonics.

A superconducting magnet is therefore a complex mechanical-magnetic system, where both the stresses and the geometry of the coil must be precisely controlled in order to get, in the operational conditions, the nominal stresses and the design coil shape. And this is even more difficult for the LHC dipole magnets, where controlling conductor motion requires a stronger force-retaining structure than in earlier magnet designs.

^d The concept of temperature margin will be introduced in chapter 4.

^e An iron-free design would have only few percent less of central field, at the price of a much higher operating current, making more difficult operation and protection, in addition to the severe problem of high stray field.

BIBLIOGRAPHY

- Bajko M., Fessia P. and Perini D., “*Statistical Studies of the Robustness of the LHC Main Dipole Mechanical Structure*”, IEEE Trans. on Applied Superconductivity, Vol.10, no.1: 77-80 (2000).
- Ballarino A., “*High Temperature Superconducting Current Leads for the Large Hadron Collider*”, IEEE Trans. on Applied Superconductivity, vol. 9, no. 2: 523-526 (1999).
- Bon Mardion G., Claudet G. and Seyfert P., “*Practical Data on Steady-State Heat Transport in Superfluid Helium at Atmospheric Pressure*”, Cryogenics, Vol.19: 45-47 (1979).
- Devred A., “*Status of the Next European Dipole (NED) Activity of the Coordinated Accelerator Research in Europe (CARE) Project*”, IEEE Trans. Applied Superconductivity, Vol.15, no.2: 1106-1112 (2005).
- Fessia P., Perini D., Russenschuck S., Völlinger C., Vuillermet R., Wyss C., “*Selection of the Cross-Section Design for the LHC Main Dipole*”, IEEE Trans. Appl. Supercond. 10 , 1 (2000) 65-8.
- Ghosh A.K., Prodell A. and Sampson W.B., “*Minimum Quench Energy Measurements on Prototype LHC Inner Cables in Normal Helium at 4.4 K and in Superfluid He at 1.9 K*”, IEEE Trans. Applied Superconductivity, Vol.9, no.2: 257-260 (1999).
- Gubello G., Serio L. and Soubiran M., “*The Circuits of the LHC Cryogenic System*”, Engineering Specification, LHC-Q-ES-0004 rev 1.0, EDMS no. 710799 (2006).
- Iwasa Y., “*Mechanical Disturbances in Superconducting Magnets – A Review*”, IEEE Trans. on Magnetics, Vol.28, no.1: 113-120 (1992).
- Leroy D., “*Review of the R&D and Supply of the LHC Superconducting Cables*”, IEEE Trans. on Applied Superconductivity, Vol.16, no.2: 1152-1159 (2006).
- LHC Design Report, Vol. I “*The LHC main ring*”, CERN-2004-003, June 2004.
- Rose-Innes A.C., Rhoderick E.H., “*Introduction to superconductivity*”, Pergamon, 1969. - 245 p. (Internat. Ser. Mono. Solid State Phys., 6).
- Rossi L., “*The Large Hadron Collider and the Role of Superconductivity in One of the Largest Scientific Enterprises*”, IEEE Trans. on Applied Superconductivity, Vol.17, no.2: 1005-1014 (2007).
- Russenschuck S., “*Electromagnetic Design and Mathematical Optimization Methods in Magnet Technology*”, e-book, Geneva 2005.
- Verweij A. and Gosh A.K., “*Critical Current Measurements of the Main LHC Superconducting Cables*”, IEEE Trans. on Applied Superconductivity, Vol.17, no.2: 1454-1460 (2007).

Wilson M. N., “*Superconductivity and Accelerators: the Good Companions*”, IEEE Trans. on Applied Superconductivity, Vol.9, no.1: 111-121 (1999).

Wilson M. N., “*Superconducting Magnets*”, Oxford UK: Clarendon Press (1983).

Wyss C., “*LHC ARC Dipole Status Report*”, Proceedings of the 1999 Particle Accelerator Conference, New York, 1999, pp.149-153 (1999).

CHAPTER 3
MECHANICAL STABILITY AND
QUENCH ORIGIN

3.1. MAGNET PERFORMANCE LIMITATIONS: QUENCH.

3.1.1. Quench phenomenology and magnet protection.

According to a classical definition (Wilson [1983] and Ašner [1999]), a *quench* in superconducting magnets represents the transition from the superconducting to the normal state of a part or the whole of a magnet. From an operational and practical point of view, the quench can be a catastrophic event, responsible for the sudden release of the energy stored in the magnetic system and eventually leading to the destruction of the magnet itself. In the case of accelerator magnets, when the quench happens with circulating particles, the consequences can be even worse, but it is not the magnet designer's concern to deal with this effect.

From a phenomenological point of view, since superconducting magnets for accelerators are normally operated very close to their critical current limit, it can happen that even minute perturbations can drive a small volume of the superconducting coil to the normal, resistive state. If the amplitude of these perturbations is such that the adiabatic and dynamic stability conditions are overwhelmed and the capacity of coolant is exceeded (that is, all passive and active systems of stabilization are not effective in recovering from the local transition), the high current flowing through the resistance-dominated zone, just created, can produce an intense local increase of the temperature. As a consequence, the temperature of the transition region and of the surroundings can rise far above the critical temperature. This phenomenon, also referred to as *thermal runaway*, causes the entire stored energy $\frac{1}{2} LI^2$ of the magnet to be dissipated as heat. If we suppose to switch off the power supply, we may equate the stored energy with the time integral of the Joule power, from the beginning of the quench up to the time t_f needed to dissipate the entire magnet energy in the growing resistance:

$$\int_0^{t_f} RI^2 dt = \frac{1}{2} LI^2 \quad (3.1).$$

The smaller the resistance, the longer the time needed to dissipate the magnetic energy. According to the so-called MIITS relation (Ašner [1999]),

$$\int_0^\infty I^2(t) dt = A_{Cu} A_{tot} \int_0^{T_{max}} \frac{\sum C(T)}{\rho(B, T)} dT \quad (3.2),$$

(where A_{Cu} and A_{tot} are the copper area and the total area, respectively, $C(T)$ and $\rho(B, T)$ the thermal capacity and the resistivity of all coil components) this means that the higher will be the hot spot temperature, T_{max} , in the quenching zone. Equation (3.2) explains why copper is so important for stabilization: it increases the term on the right of the equation, due to high C and low resistivity, thus reducing T_{max} , and protect the magnet from overheating after a quench (with only NbTi a magnet would burn out after just 1 ms).

The energy stored in each LHC dipole (nearly 7 MJ at nominal field), but commonly in most superconducting magnets, is so high that the time t_f would be large enough to produce drastic damages to the quenching portion of the superconducting coil, if the normal zone (*i.e.* the resistance) was not increased faster than what is due to the simple quench propagation; this is the reason why, as soon as a quench is detected, the temperature of the whole coil is rapidly increased by means of *quench heaters*, to drive more fraction of the coil to the resistive state. These are stainless steel strips, partially plated with copper to reduce their resistance and to allow for their electrical connection; co-laminated in a sandwich of 2x75- μm -thick polyimide insulating foils, they are put in contact with the coil and are powered by capacitor bank discharge power supplies. Many analyses were carried out to determine the optimum parameters for the quench heaters to be used in the LHC dipoles (Rodriguez-Mateos [2000, 2001]) and finally their dimensions were set to 25 μm in thickness and 15 mm in width. The position of the quench heaters for the LHC dipoles is schematized in Figure 3.1.

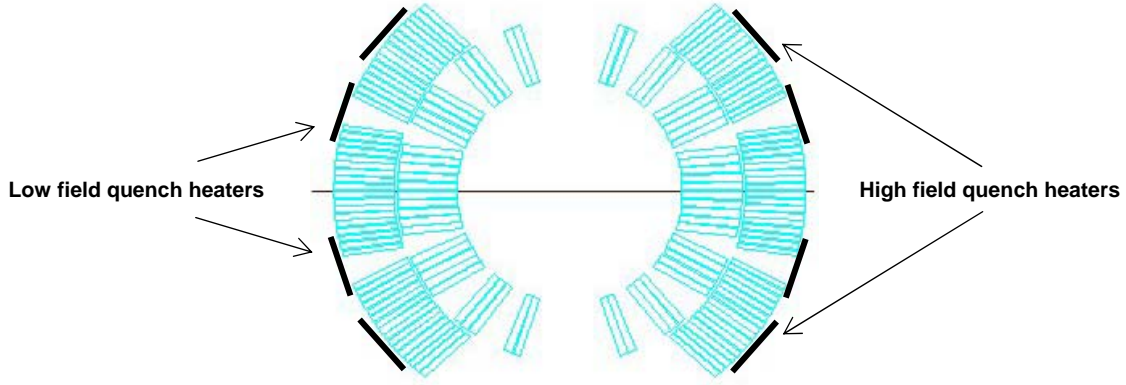


Figure 3.1 _ Position of the quench heaters in each aperture; they are distinguished in high and low field QH's according to the field in the nearby cables.

The risk for degrading magnet integrity during a quench does not only arise from the fast increase in temperature: when a resistive region is appearing, a high voltage is also developed across the terminals of the quenching magnet. According to Wilson [1983] and looking at Figure 3.2, we can write the voltage across the quenching zone (V_Q) as the sum of the resistive and the inductive part:

$$V_Q(t) = I(t)R_Q(t) - M \frac{dI(t)}{dt} \quad (3.3),$$

where R_Q is the resistance of the quenching/normal zone, I the (time dependent) current circulating in the circuit and M is the mutual inductance between the normal zone and the rest of the magnet. At the same time, considering the voltage drop across the converter (V_{PS}) small, we can equate the inductive and resistive components within the whole magnet:

$$\frac{LdI(t)}{dt} = I(t)R_Q(t) \quad (3.4),$$

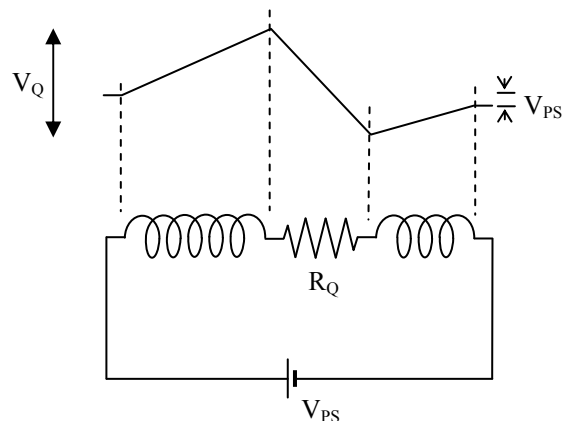


Figure 3.2 _ Equivalent circuit of a quenching magnet.

with L representing the inductance of the whole magnet. Equation (3.3) and (3.4) lead to:

$$V_Q(t) = I(t)R_Q(t)\left(1 - \frac{M}{L}\right) \quad (3.5).$$

As for temperature, high internal voltages are avoided by spreading the normal zone as widely as possible and by making M large.

The danger of high voltage generation on the magnet integrity is amplified by the sudden mechanical force release. In a few tens of milliseconds, while the temperature is rapidly increased by tens of Kelvin, the electromagnetic forces (that at full current tend to ovalize the coil along the mid-plane) disappear. It may happen that weak insulation points, under the combined effect of high stresses and high voltages, fail, possibly provoking serious damages to the magnet. In Figure 3.3, the result of such destructive phenomenon is shown during the power test of a magnet: after several quenches, and during the last one of these, an inter-turn short circuit appeared in one of the apertures, due to the high voltage developed in a place where the insulation was probably defectuous.



Figure 3.3 _ Effect of an electrical short.

The electric arc created between the short-circuiting parts was so energetic that it rapidly increased the temperature well above the melting point of the superconductor, which was burst and expelled by the high pressure boiling helium through the collar interstitials and a hole produced in the cold bore tube: the hole in the right hand picture of Figure 3.3 is the result of such event. As can be seen in this picture, the short circuit originated at the aperture mid-plane, where the Lorentz force tends to compress the coil at maximum energization.

The LHC dipole insulation integrity had always been carefully checked, but since this episode, the criteria to detect faults were tightened to avoid similar cases in the future: insulation breakdowns (coil-to-ground as well as coil-to-coil) were since then tested up to 600 V at warm and 2000 V at cold with negligible current leakage (200-300 nA maximum), to ensure durable operation of the magnets.

3.1.2. Protection for the LHC magnet strings.

We have seen that, by means of the quench heaters, we spread the energy released in a quench over a large volume, thereby reducing the maximum temperature increase. This is often sufficient to protect a single magnet; however, the energy stored in the other magnets, which are connected in series, might be too large to be absorbed. In this case, as much current as possible has to be routed around the quenching magnet by relying on a diode working at cryogenic temperatures, mounted in parallel to the magnet coils. This diode has a low temperature turn-on voltage of a few volts: once a quench has generated enough resistance in the magnet and the corresponding voltage exceeds the turn-on voltage, the diode starts to conduct. But the diode itself would be overheated and possibly burned out if the current was not dumped on an external resistor; on top of that, dumping the energy in the diodes takes a very long time. Therefore all major energy dumping systems have an external switch, bypassed by a dump resistor (Dahlerup-Petersen [2000]): once a quench is detected, the switch opens and the current is dumped on the resistor.

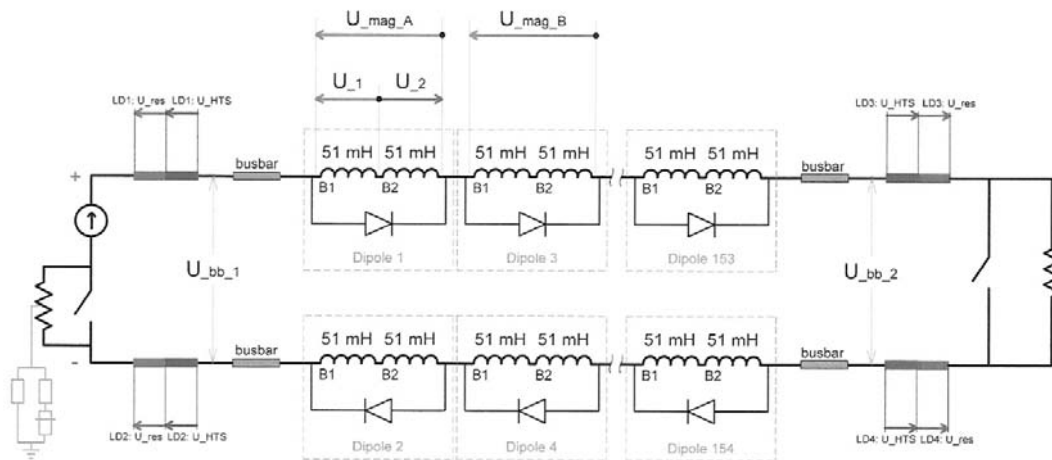


Figure 3.4 _ Schematization of a main dipole magnet string.

In Figure 3.4, the electrical circuit of a main dipole magnet string is modeled. The 154 main bending (MB) magnets per arc are alternately connected^a: the odd magnets form a string connected to the string of even magnets through two switches and two dump resistors. In the figure, the diodes bypassing each dipole are also shown, together with some signals used for the protection and the warm cables which connect the switches and dump resistors with the superconducting circuits.

An example of the energy extraction resistors and the mechanical switches are shown in Figure 3.5.



Figure 3.5 _ Dumping resistors for the main dipole magnets (left) and detail of the switches (right).

The energy extraction impacts other systems in the power circuit. Voltage waves are created by the opening of the switches, sweeping through the magnet strings. If not attenuated, the amplitudes of the waves would exceed the ramping voltage by far. For MB strings, 100 m Ω resistors connected across the dipole terminals serve this purpose. The effect on the precision of the current due to the leakage during current changes is negligible.

When a magnet quench occurs, the diodes conduct a current pulse of up to 13 kA which decays exponentially with a time constant of about 100 s. This leads to a temperature rise inside the diode of up to 300 K.

^a The reason for this alternate connection mainly resides in the reduction of propagation of quench between neighboring magnets.

3.1.3. Experimental characterization of a quench.

From the definition of quench as the transition of a superconductor to the normal state, it is clear that the most important experimental evidence of this phenomenon is the appearance of a resistance, growing in accordance with the spreading of the normal zone. It is for this reason that magnets are normally equipped with voltage taps to detect any anomalous voltage increase as an indication of a resistive transition. The LHC dipoles, in particular, were provided with voltage taps at the extremities of each pole, which permit a pole-to-pole (upper with lower) compensation and a proper discrimination of the resistive signal with respect to the inductive one in conditions of changing current. Especially, during ramping of the current to the nominal operating field (a nominal ramp of 10 A/s is foreseen for it), the nearly 25 mV inductive signal developed in the 25-mH-inductive pole would cover by far the beginning of the resistive transition and render its detection dangerously slow. On the contrary, with this compensation, a safe criterion for quench detection was established, which considers the start of the transition when a *voltage threshold* of 100 mV for a time larger than 10 ms has been attained. When the voltage threshold and the *validation time* are exceeded, all the active protection systems are triggered (in particular, the quench heaters are fired).

Two examples of the voltage signals at quench in a dipole magnet, recorded during cold test at the Superconducting Magnet Test Plant SM18 (Siemko [2004]), are presented in Figures 3.6 and 3.7, at an helium temperature of 1.9 K and 4.4 K, respectively. Both kinds of quenches are treated in details in the next paragraphs, but we nevertheless address the main features here. Let us point out, in particular, what are the differences in the three key phases of the quench dynamics: the origin of the transition, the quench propagation and the firing of the quench heaters; in fact, in both cases, the quench originated in the first aperture (positive *D1-D2* signal) but dissimilar behaviours in the three phases can be observed.

First of all, for the quenches at 1.9 K, it is explained in § 3.1 that the start of the quench is always accompanied by a high mechanical activity, well evidenced by the spikes at the beginning of the transition in Figure 3.6, a clear signature for a thermally-induced quench. The situation for the quench around 4 K is entirely different: the superconducting limit has been reached and the transition from the superconducting to the normal state is experienced macroscopically as a smooth transition. Moreover, the slope of the voltage rise in the second case is nearly 10 times larger than in the former one, during the first ms after quench starts (100 mV/ms vs 12 mV/ms). To understand the difference between the motion-originated quench and the conductor-limited quench, we need to recall the fact that for the quench around 4 K the whole cable, and not only a portion of it, is close to its current limit. At 1.9 K, the training quenches are due to the settlement of the magnet mechanical structure occurring under the effect of the huge Lorentz forces: these drive only a portion of the cable to quench, because of frictional heating, and the remaining of the cable is far from transition which implies that it takes some time for the quench to propagate.

In both cases, the quench heaters are fired at the same threshold voltage level (and there is therefore the same time delay from quench detection to energization of the quench heaters, visible as a chaotic disturbance at 2 ms on the charts), but different values of voltage are reached before the activation of the quench heaters, in accordance to the different slopes.

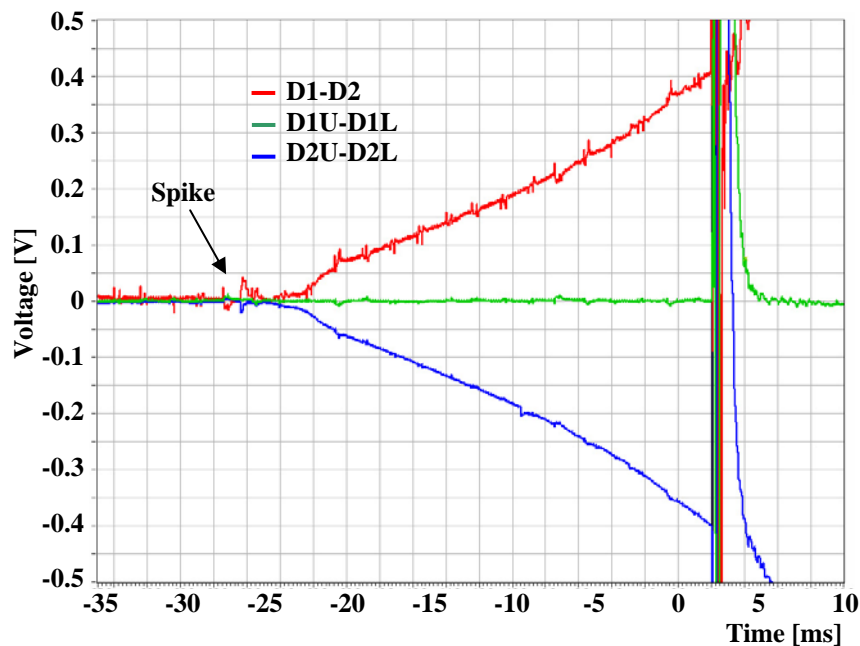


Figure 3.6 _ Signal record of voltage taps during a mechanically-induced quench at 1.9 K.

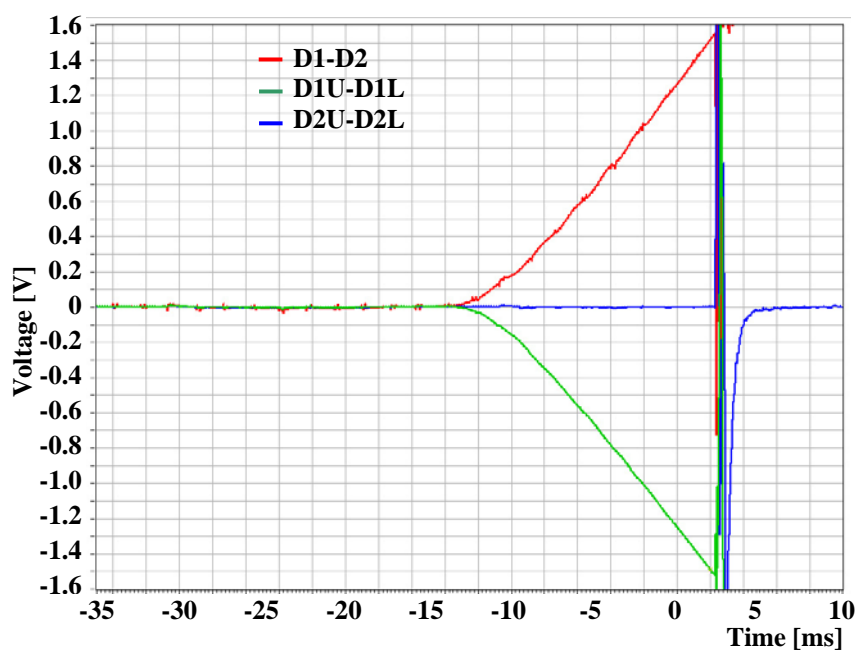


Figure 3.7 _ Signal record of voltage taps during a conductor-limited quench at 4.4 K.

Due to the reduced number of voltage taps each magnet is instrumented with, they offer the possibility to only distinguish the pole where the quench originated. For a longitudinal detection of it, a more accurate instrument is used, the *quench antenna*: a shaft, composed of 13 electrically insulated modules, whose cross-section is presented in Figure 3.8.

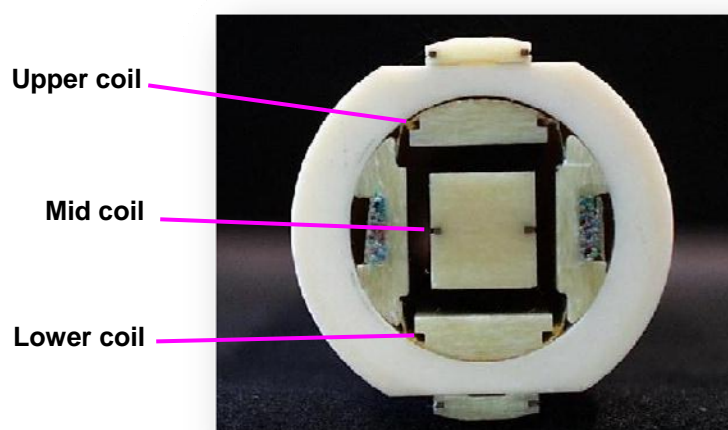


Figure 3.8 _ Quench antenna cross-section.

Each module is 1152 mm long and is separated from its neighbours by 108 mm. As can be seen in Figure 3.8, it is made up of three parallel pick-up coils, two tangential and one in the center of a vitroc ceramic tube; the coils are wound with several hundreds of very thin wires to increase the voltage signal produced by the variation of the concatenated flux (fluxmeter method, Henrichsen [1997] and Bottura [2002]). It is in fact important to underline that, in the case of the quench antennas, the signal recorded is not a direct measure of the resistance appearing inside the superconductor, but it is produced by the flux variation following the redistribution of current inside the superconducting cable. A detailed description of the twin rotating coil system (one system per magnet aperture) is given by Billan [2000].

The pick-up coil shafts were mainly built for the identification of the magnetic field perturbations (see Leroy and Krzywinski [1993]), through a harmonic analysis of the induced signal recorded during the rotation of the shafts in the fixed external field, but they found an important application in localization of the quench origin. This was especially important during the prototyping phase and at the beginning of magnet production, where identification of the weak points in the magnets was instrumental.

Analysis of the quench signals recorded via the quench antennas can also be used to deduce important parameters for the magnet protection, as, for example, the quench propagation velocity along the superconducting cable. Figure 3.9 shows the same quench as the one displayed in Figure 3.7 but recorded by the pick-up coils. In this case, we can recognize the quench origin in sector S09 and then the quench front propagating from one sector to the nearest ones (S10 first and S08 a bit later). This enables a precise longitudinal

localization of the quench origin and a direct estimate of the quench propagation velocity from the time delay between the appearance of the quench and its propagation to the nearby sectors. In this specific case, a value around 65 m/s is obtained (values around 25-30 m/s are normally found at 1.9 K).

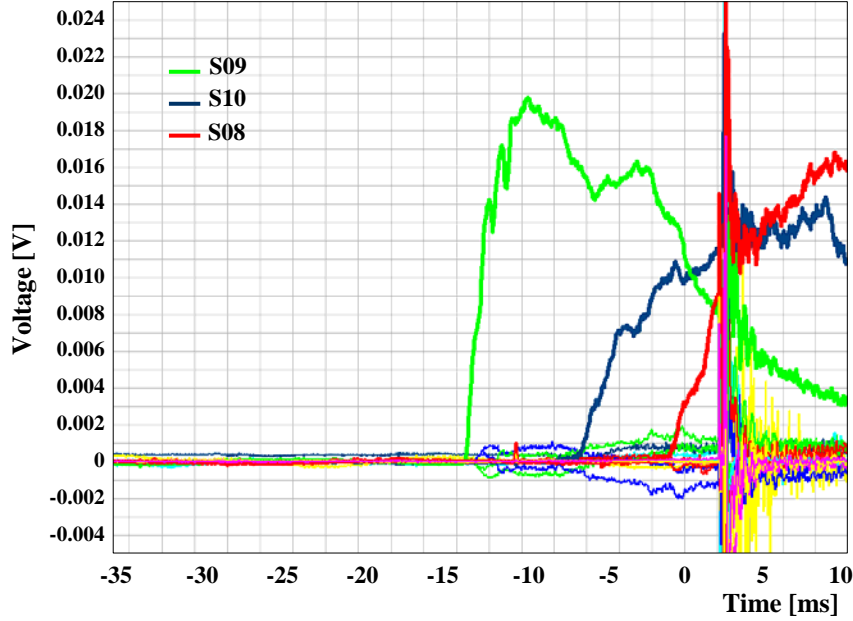


Figure 3.9 _ Quench antenna signals for the same quench at 4.4 K as in Figure 3.7.

As for the voltage taps, the signals analyzed here are the result of a differential combination of those coming from two independent coils, which enables a reduction of the noise produced by current oscillations and an increase in measurement sensitivity.

3.1.4. Quench origin.

If we look at the design parameters of the LHC dipoles, and keeping in mind the critical surface of NbTi, it is obvious that these magnets are normally designed to operate with a safe margin. This means that the quench performance of a superconducting magnet is not only determined by the critical current of the conductor from which it is wound. There are several other (eventually concomitant) phenomena which are responsible for magnet quenches. Considering a magnet wound with a superconducting cable with a given critical current, we can distinguish between quenches which have a technical limitation and quenches with an operational limitation. In the first class, we include the quenches originating in magnets with a local degradation of the conductor (this is the case of a pole whose cable presents cold welds) or bad cable joints, which can be the origin of thermally induced quenches and/or non-uniform current redistribution (BICC's, see Verweij [1995]).

The second category includes the quenches appearing in magnets where the critical temperature is exceeded because of frictional heating from mechanical disturbances (conductor motion under the effect of the Lorentz forces) or energy deposition, due to beam losses.

The conductor-limited quenches, treated in the next paragraph, provide a useful tool for detecting the defects at the origin of the first type of quenches. They can also be used to deduce an important magnet parameter: the *temperature margin*, *i.e.* the difference between bath temperature and critical temperature at the design field and current; in this sense they are a useful instrument to evaluate magnet capability to cope with both dynamic and static losses. In fact, as shown in Table 3.1, the minimum requirement for temperature margin is around 1.4 K, which accounts for measurement errors, continuous Joule heating (even if very low, a resistance is always present at a splice interface), transient AC losses inside the conductor and beam energy deposition. The last term, in particular, represents the largest fraction of the required temperature margin (see Lefèvre and Pettersson [1995]).

TABLE 3.1 _ TEMPERATURE MARGINS REQUIREMENTS FOR DIFFERENT EFFECTS.

Phenomenon	ΔT
J_c measurement precision	± 0.05 K
Dissipation at $\rho=10^{-14}$ Ωm	0.27 K
Beam losses	1.12 K
Ramping losses at 1200 s	0.02 K
TOTAL	~ 1.4 K

Temperature margins for several magnets from different producers were measured and they proved to be sometimes only slightly above the 1.4 K needed for a safe operation, which means that there is limited space for uncontrolled heating effects.

Solid friction and heat generation have an important effect on the magnet quench performance; we show in the following that the training (that is the “progressive improvement in performance after repeated quenching”, Wilson [1983]) all the magnets undergo, during cold tests, helps in reducing the impact on magnet performance during operation. Excessive instability during cold test is, on the other side, unacceptable and it became a selection criterion for magnet rejection.

3.2. CONDUCTOR-LIMITED QUENCHES.

In the framework of the series tests of the superconducting dipole magnets for the LHC (Bottura [2002], Siemko [2004]), a special procedure was developed to perform quenches at temperatures around 4.4 K. Unlike the training at 1.9 K, where the quenches are usually motion-originated events (Devred [1990], Pagnat [2001]), the appearance of a resistive signal in the dipoles at higher cryogenic temperatures (and, in any case, well below the critical temperature of NbTi) is driven by approaching the maximum superconductor current. If we look at the critical surface (Wilson [1983]), in fact, increasing the temperature means reducing the maximum transport current of the superconductor, which, in turn, means a lower Lorentz force. The experience gained on 1-meter-long models and full-scale dipole prototypes demonstrated that when the magnet powering is limited to current values around the 4.4-K short sample limit of the conductors, the mechanical activity of the winding is indeed reduced. To further stabilize the coils of LHC main dipoles, their training was accomplished at 1.9 K before tests around 4.4 K.

This kind of investigation was particularly used at the beginning of the production of LHC dipoles, to validate the integrity and the in-situ performance of the conductors and, also, to estimate the margin of each magnet in terms of temperature at the nominal operating conditions of the machine (later on, this became a part of the test procedure for those magnets showing an insufficient performance at 1.9 K). The procedure consisted in comparing the quench current values with the critical currents measured on short samples of the cables used in winding the magnets.

Combined with a precise localisation of the beginning of the transition using quench antennas, as described in the previous paragraph, these quenches allow to detect and to identify possible degradation of the conductor performance or faulty electrical connections between the superconducting cables of the inner and the outer layers. Precise diagnostics of the quench origin of the main superconducting magnets is an important quality control step. Any drift in production or critical fault in the manufacturing process must be detected and precisely identified to allow the manufacturers to take appropriate corrective actions.

3.2.1. Mechanical stabilization of coil and cryogenic transition.

As just mentioned, before performing the conductor-limited quenches at temperatures around 4.4 K, the magnet had to be mechanically conditioned at 1.9 K through a successful training up to the ultimate field of the LHC, equal to 9 T. This step is particularly important to improve the mechanical stability of the winding. We speak about it and the memory effect in more details in the next paragraph; for the sake of comprehension, it is just sufficient to mention that once reached a certain current/force value any magnet ‘keeps the memory’ of this value, at least within more or less 10%.

Thanks to the rigorous procedure followed, a quench current reproducibility at a level of 0.2% was attained for the quenches at 4.4 K (whereas the uncertainty in current measurements is typically in the 10 ppm range).

A short description of the CERN Superconducting Magnet Test Plant (SMTP) is given by Siemko [2004]. Cryo-dipoles are connected to Cryogenic Feeder Units (CFU) which are thermally-insulated vessels containing the helium pipe work and helium-cooled high-current busbars (Benda [2000]). On test benches, the cool-down of the magnet is performed first by using helium gas, from room temperature to about 80 K, and then with liquid helium (LHe). At 4.4 K, the magnet is filled with about 300 liters of LHe and is cooled down to 1.9 K by pumping on the bath in the gas-liquid heat exchanger tube, which extracts the heat from the cold mass all along its length. The magnet warm-up from 1.9 K to 4.4 K was initially obtained by stopping the pumping on the heat exchanger tube. This warm-up, mainly driven by the cryo-magnet heat in-leak, is a slow, quasi-adiabatic, process (Figure 3.10-a), which takes 2 or 3 hours. However, it was proven in different ways that the time needed for reaching equilibrium between bath and magnet, after the desired temperature had been approached, was about 20 min; for example, in one case, the quench performed after 20 min, was repeated after having waited for more than three hours and the current was found equal within the temperature error. To ensure a stable temperature and to shorten the needed time in the framework of series tests, a different procedure was nevertheless developed. A quench at 3 kA was provoked with quench heaters to produce the global heating that was just sufficient to increase the magnet temperature up to 4.4 K (Figure 3.10-b).

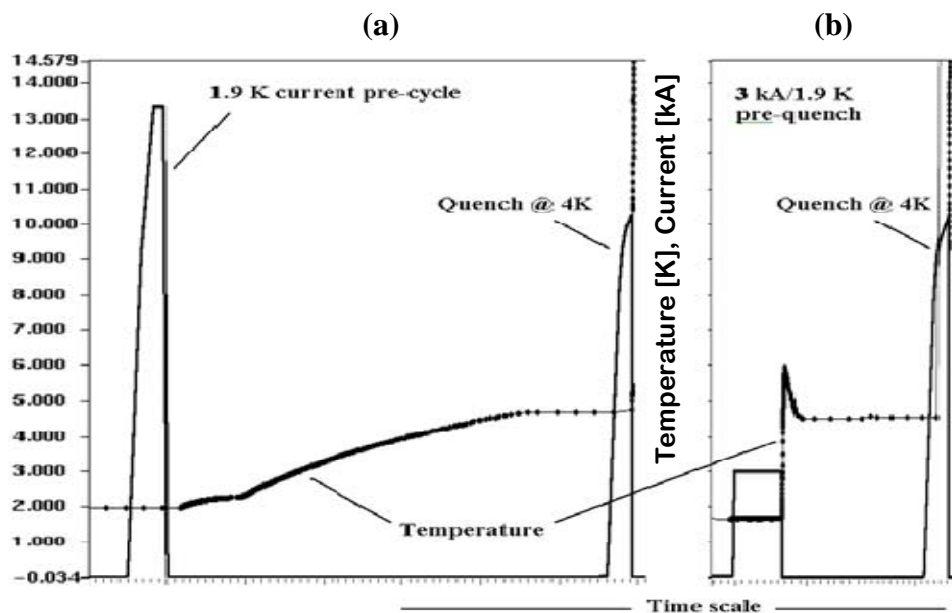


Figure 3.10 _ Procedure for raising magnet temperature from 1.9 K to 4.4 K. In (a) the magnet warm-up is naturally driven by the heat in-leak, in (b) a 3 kA provoked quench produces an accelerated warm-up.

The study of conductor-limited quenches of a superconducting magnet requires an accurate determination of the coil temperature. For the data presented in this study, three inputs were used, two coming from Cernox™ temperature sensors and one from the helium gas pressure measured above the bath. One of the temperature sensors was located at the middle of the cold mass and the other one at the outlet of the magnet LHe supply. Both were calibrated to guarantee a measurement uncertainty within ± 10 mK. A detailed study showed a systematic difference of about 23 ± 5 mK between the temperature determined from the pressure measurement and the one given by the thermometers. This corresponds, taking into account the accuracy of the sensors, to the hydrostatic pressure of the LHe column inside the CFU. Conductor-limited quenches were performed in stable pressure and temperature conditions within an overall uncertainty of ± 15 mK.

3.2.2. Comparison with critical current.

It was already explained that for the safe operation of the machine, a minimum margin for the superconductor has to be guaranteed, to compensate for energy deposition and Joule heating at the splice level (and possibly also for inefficient cooling). This translates into a minimum specified critical current value, defined in the *Technical Specification* for the strands [1997], as shown in Table 3.2.

TABLE 3.2 _ MINIMUM ACCEPTABLE I_c FOR DIPOLE INNER AND OUTER LAYER STRANDS.

		Cable 1 (28 strands)	Cable 2 (36 strands)
I_c @ 1.9 K	Virgin	515 A @ 10 T	380 A @ 9 T
	After cabling	491 A @ 10 T	360 A @ 9 T
I_c @ 4.222 K	Virgin	532 A @ 7 T	387 A @ 6 T
	After cabling	505 A @ 7 T	367 A @ 6 T

The minimum acceptable overall currents are 14140 A (at 7 T and 4.222 K) and 13212 A (at 6 T and 4.222 K) for the inner layer and outer layer cables, respectively. For each dipole, at the beginning of the production, the critical current of a short sample of the cable used in the winding was measured, with an uncertainty of ± 2 %. The objective was to compare this measurement with the quench current obtained at 4.4 K; the comparison of the quench current I_q with I_c must be performed at the same magnetic field and temperature. For this purpose, the following formula was used:

$$I_c[T_q, B_q] = \{I_c[4.22K, 7T] - s \cdot (B_q - 7)\} \cdot \frac{T_c[B_q] - T_q}{T_c[B_q] - 4.22} \quad (3.6),$$

which is a linear interpolation, in temperature and field, of the short sample critical current. In equation (3.6), T_q is the temperature of the magnet at quench, B_q the quench field on the conductor, given by the transfer function measured on each magnet and corrected by the peak field coefficient (+3% more or less), and the slope s of the $I_c[4.22\text{K}, B]$ variation was deduced from two measurements of I_c at 6 and 7 T; $T_c[B]$ expresses the field dependence of the critical temperature (inverse Lubell formula [1983]):

$$T_c[B] = T_{c0} \cdot \left(1 - \frac{B}{B_{c20}} \right)^{1/1.7} \quad (3.7),$$

where, for NbTi, $T_{c0} = 9.2$ K and $B_{c20} = 14.5$ T.

Figure 3.11 shows a comparison between the quench current values at three different temperatures (with the ± 15 mK error bar) for magnet 1002 and the extrapolated cable critical current (blue upper line); also shown in red, in the lower part is the extrapolation of the minimum cable specification.

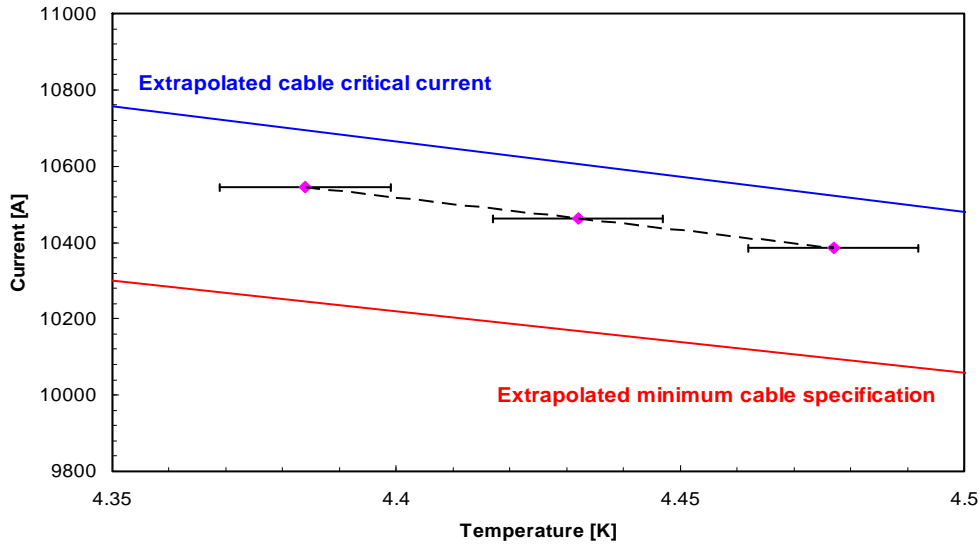


Figure 3.11 _ Results of conductor-limited quenches performed on the dipole 1002. Two quenches were performed at 4.385 K with a current difference of 1 A.

It appears, from this figure, that the quench current is well above the minimum acceptable value, but also around 5% below the value deduced from the critical current measurement.

It has to be noticed that Eq. (3.6) only contains linear terms (save for Eq. (3.7)), whereas we have seen that the critical current has a non-linear dependence on B and T ; it is consequently not exact. Nevertheless, the error in such approximation is very small for fields not far from the 6-7 T range and for temperature close to 4.22 K, and in any case smaller than the 2% error in I_c measurements.

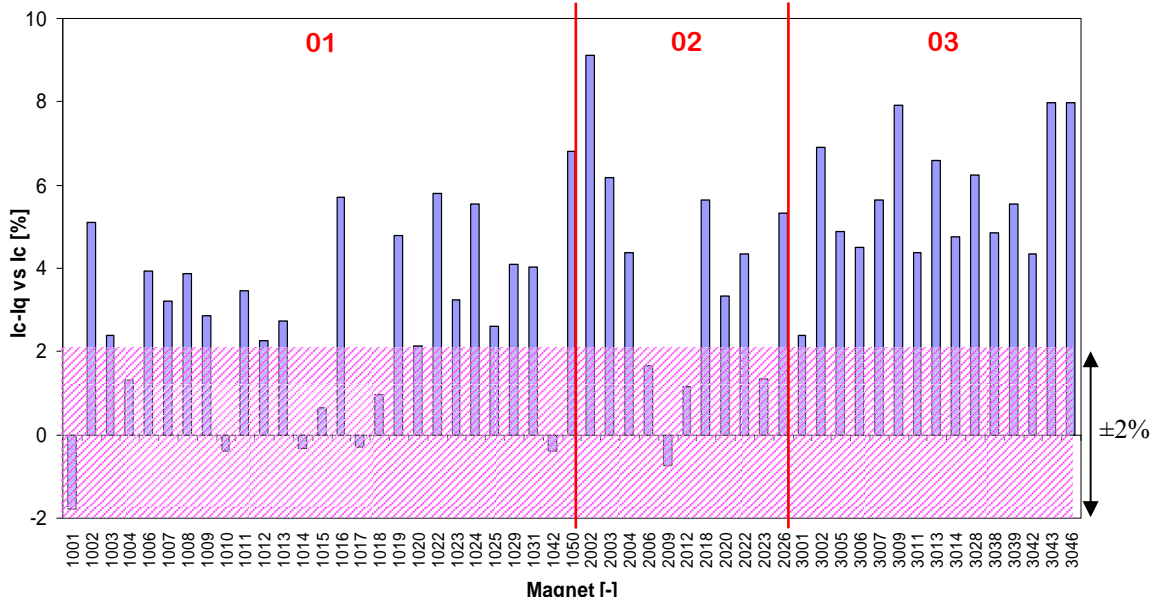


Figure 3.12 _ Relative difference between I_c and I_q at 4.2 K for LHC dipoles produced by the three manufacturers. Each bar was obtained as an average of 2, 3 or even 4 quench current values.

The relative difference observed between quench current and critical current are given in Figure 3.12 for 53 LHC dipoles, delivered by the three manufacturers and cold-tested. The results are summarized in Table 3.3 and the following comments can be made before discussion:

- i) I_q appears to be systematically lower than I_c by up to 6 to 8%;
- ii) the results are clearly manufacturer dependant.

It is important to observe that the quench current and the critical current are different entities. In fact, I_c is defined as the current for which the resistivity of the superconductor exceeds $10^{-14} \Omega\text{m}$, while the I_q is the runaway current, defined at a quench detector threshold of 200 mV. It is quite difficult to establish a numerical relationship between the two (although some attempts have been carried out, which can explain quench current values in the order of 3% larger than I_c), but, nevertheless, it can be asserted that the quench current should always exceed the critical current and can be thus considered an overestimation of it. This is therefore in contradiction with the observed quench values, whose explanation can be looked for in the difference of test conditions. In fact, I_c measurements are performed in conditions of uniform field, while inside the magnet the cables are subjected to a field gradient, which can produce a current decrease (BICCs and non-uniform sweep rate, Verweij [1998]). Inside the dipole, the cables are subjected to a maximum field gradient of 1.13 T/cm, whereas for I_c measurements, the non-uniformity only comes from the self-field distribution.

If we neglect the difference in detection method, and take the field gradient as the limiting factor for quench current, it cannot, nevertheless, explain the differences between producers. Excluding the case of producer 02, which showed an anomalous behavior addressed below, the significant difference between the averaged values related to the superconducting dipoles assembled by firms 01 and 03 supports an interpretation that considers a degradation of the in-situ performance of the superconducting cables with respect to the I_c measurements. This degradation depends on the cold mass manufacturer (Table 3.3) and not on the cables producers, since the cable producers provide cables indifferently to all three magnet assemblers.

TABLE 3.3 _ RESULTS FOR THE THREE COLD MASS PRODUCERS.

<i>Producer</i>		01	02	03
<i>No of magnets</i>		27	11	15
$I_c - I_q$ vs I_c [%]	<i>Average</i>	2.76	3.79	5.66
	<i>Stand. Dev.</i>	2.22	2.81	1.61
	<i>Min</i>	-1.79	-0.74	2.38
	<i>Max</i>	6.81	9.11	7.99
<i>T margin [K]</i>	<i>Average</i>	1.53	1.56	1.52
	<i>Stand. Dev.</i>	0.04	0.06	0.05
	<i>Min</i>	1.46	1.44	1.38
	<i>Max</i>	1.63	1.64	1.59

Regarding company 02, several magnets delivered by this company showed abnormal quench results at 4.4 K: all these quenches originated at approximately the same location, about 350-500 mm from the non-connection side end. This is the position where the inter-layer splice and the layer jump are placed (see Figure 3.13). There is no particular reason why the quenches should be concentrated in one region, especially in magnet ends. In fact the field is reduced by nearly 9% in the ends, by the use of nested laminations; this reduction starts at 86 mm from the end of the layer jump, as shown in the figure, and the field changes quite abruptly from the nominal to the reduced value. This reduction was adopted at the end of the prototype phase to consolidate magnet's extremities: lowering the field means decreasing the Lorentz force and increasing the temperature margin. Quenches at 1.9 K in the extremities were greatly reduced, while they should be absent at 4 K.

The predominance of quenches at the splice/layer-jump level suggested a repetitive damaging of the conductor or a faulty connection between inner and outer layer cables. Investigations were launched to check the mechanical tolerances of the tooling used for soldering the splice at the firm, as well as detailed analysis on all the control parameters and

thermal treatment procedure to detect differences with the other producers. In particular, tests of the splice resistance on several samples were performed by Verweij [2006], using mock-ups coming from the different producers. The results of this measurement campaign are shown in Figure 3.14: the various splices produced by firm 02 had resistance values lower than the specification of $0.6 \text{ n}\Omega$ and not different from those of the other two companies (the slightly higher resistance found in one case is not enough to account for the drastic increase in temperature which would produce the reduction in performance that were found in some magnets).

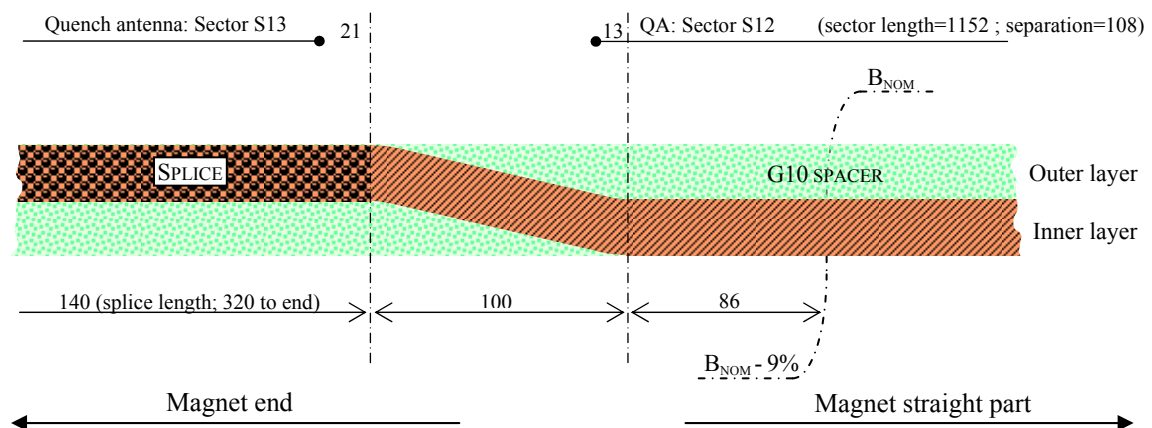


Figure 3.13 _ Schematic of the splice between inner and outer layer cables; four of such joints are present in a magnet, in the non-connection side end (distances are in mm).

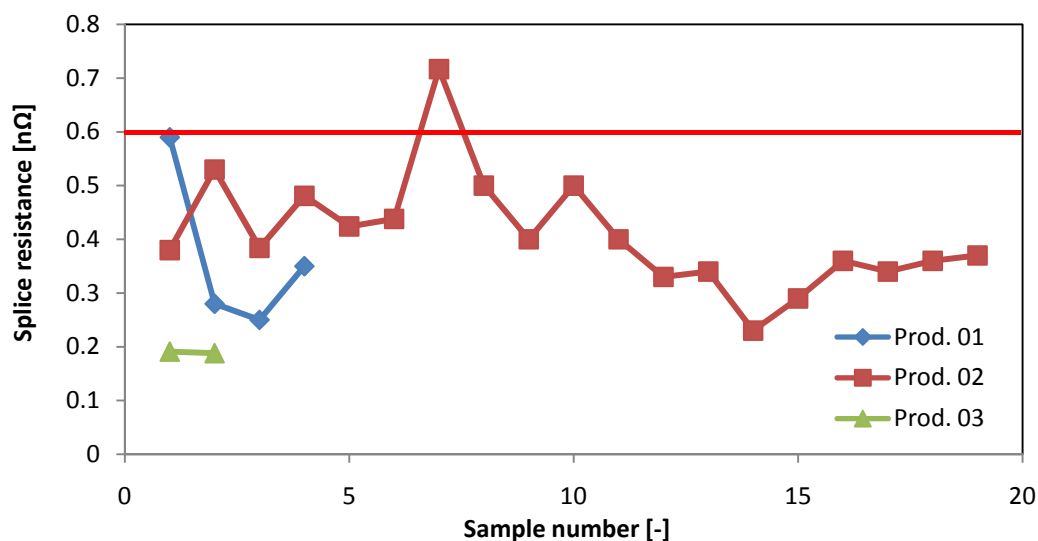


Figure 3.14 _ Comparative resistance measurements performed on splice samples produced by the 3 firms.

The experimental results support the evidence that the origin of the quench performance degradation has not to be found in the temperature increase due to Joule heating, but in the abnormal distribution of current at the junction between the two cables combined with the increasing field when moving from the splice, through the layer jump, to the high field region.

Although the exact origin was never pinned down, sometimes major faults were observed (see, for example, the mechanical deformation of the G10 support of the layer jump in Figure 3.15) and, in any case, the warning given to the firm was enough to trigger the improvement of the controls during production and, thereby, the quality of the splices.



Figure 3.15 _ Fracture of G10 support for the layer jump.

Because these faults have no practical influence on the magnet operational quench performance, the dipoles were accepted by CERN and it was recommended allocating them to special positions in the LHC tunnel where the beam losses are smaller.

3.2.3. Algorithm for temperature margin estimate.

The temperature margin (ΔT_s) of a superconducting magnet is in general defined at nominal current as the difference between the current sharing temperature of the conductor at the design peak field (B_p) and the bath temperature (T_b). If we refer to Figure 3.16, with a local linear extrapolation of the I-T characteristics, we can derive the relation:

$$\frac{I[T_b + \Delta T_s, B_p]}{I_q[T_b, B_p]} = \frac{T_c[B_p] - (T_b + \Delta T_s)}{T_c[B_p] - T_b} \quad (3.8),$$

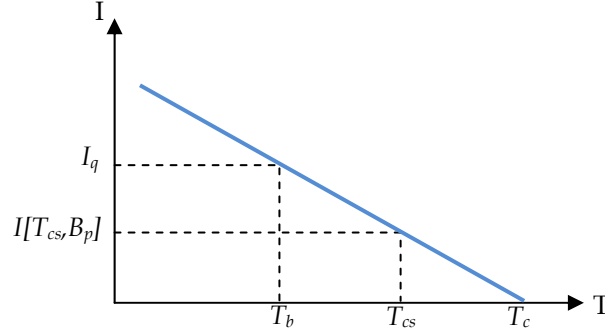


Figure 3.16 _ Linearization of I-T characteristics.

where $T_b + \Delta T_s$ is the current sharing temperature, T_{cs} , and $T_c[B_p]$ is the same as given by Eq. (3.7). From Eq. (3.8) we get:

$$\Delta T_s[T_b, B_p] = (T_c[B_p] - T_b) \cdot \left(1 - \frac{I[T_b + \Delta T, B_p]}{I_q[T_b, B_p]} \right) \quad (3.9),$$

with $I[T_b + \Delta T, B_p]$, nominal current of the LHC, equal to 11850 A, $T_b = 1.9$ K and $B_p = 8.58$ T. The quench current at 1.9 K and peak field, $I_q[T_b, B_p]$, is calculated in the following way:

- the critical current at 4.2 K and 7 T, measured for each cable, is linearly extrapolated at 1.9 K and 10 T,

$$\frac{I_c[1.9K, 10T]}{I_c[4.2K, 7T]} = \text{const} \pm 0.1\% \quad (3.10),$$

different for each producer;

- from $I_c[1.9K, 10T]$ and the B_{c2} value (average quantity for the cables produced from each producer), we get, by linearization,

$$\frac{I_c[1.9K, B_p]}{B_p - B_{c2}} = \frac{I_c[1.9K, 10T]}{10T - B_{c2}} \quad (3.11);$$

- the quench current is obtained from the value $I_c[1.9K, B_p]$ calculated in (3.11), after correction by the corresponding percentage values of Figure 3.12.

In this way, the temperature margins of several dipoles produced by each company were deduced from conductor-limited quenches. The average and minimum/maximum values are reported in Table 3.3. All, but one value, are larger than the 1.4 K minimum requirement for the inner cable to balance all terms contributing to the heat generation at nominal conditions of the LHC, including beam losses. In the only case where a slightly lower value

was found, it could be attributed to the use of a cable produced according to older and less stringent specifications.

There is a last point that deserves to be added to what we said for conductor-limited quenches: the different cooling conditions during magnet operation (1.9 K helium) with respect to the cryogenic conditions of cold tests (temperatures around 4 K). In fact, the use of superfluid helium largely increases the heat removal capacity through the coolant. On the opposite, reducing the temperature by more than a factor of two has the detrimental effect of reducing the heat capacity of the cable by almost an order of magnitude. For a given temperature margin, the energy deposition that can trigger a quench can be therefore substantially different.

It would clearly be more correct to estimate the temperature margin from conductor-limited quenches performed at 1.9 K, but this is impossible, as we said, because of the huge Lorentz forces acting on the coils and the mechanical limitations that prevent the magnets from reaching their limits at this temperature.

Nevertheless, the quenches around 4 K provide complementary information for the performance evaluation of each dipole and were proposed to be used to sort out and position the magnets in the LHC to optimize their performance.

3.3. SOLID FRICTION AND HEAT GENERATION.

3.3.1. Stick-Slip phenomenology.

It has been noted in §1.2 that the quenches at 1.9 K are almost always characterized by voltage signals like the one presented in Figure 4, where the beginning of the transition is accompanied by a rapid, localized change in magnetic flux, responsible for a fast oscillation in the voltage induced in the pick-up coils (namely, a “spike”), either in a quench antenna or in the magnet coil itself. This phenomenon has been widely investigated in past and present times and it is commonly thought to be the proof of a sudden release of the electro-mechanical energy stored in the coils. Friction, and in particular the solid friction acting between rigid bodies, are the key to the interpretation of such phenomena.

A basic explanation of solid friction has been for a long time the one provided by the Amonstons-Coulomb laws [1699, 1785], whose description can be assisted by the simple model of a spring attached to a mass that lays on a plane, as sketched in Figure 3.16-a.

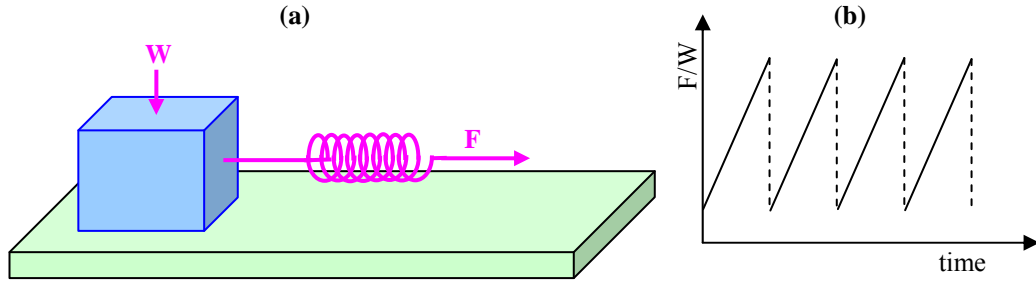


Figure 3.17 _ (a) The mass-spring model for solid friction explanation. (b) Friction coefficient vs time in a typical stick-slip phenomenon.

In this setup the mass (whose weight is W) is attached to a coiled spring being pulled by a tension force (F) so that the spring moves at a constant velocity.

According to the classical interpretation, no motion of the block occurs as long as F is smaller than a finite threshold F_s ; once occurring, sliding is dissipative and the corresponding dynamical friction force, F_d , is constant and equal to F_s . A simple relation can be established through the friction coefficient:

$$\mu_{s/d} = \frac{F_{s/d}}{W} \quad (3.9).$$

This is a simplified description, where a static threshold and a velocity-independent dynamic force are used. Various deviations from it have been observed, the most salient of which are the following:

- in general, the static friction coefficient, μ_s , is larger than the dynamic one, μ_d ;
- μ_s is not a mere number, but a slowly increasing function of the so-called *waiting-time* t_w , *i.e.*, the duration of static contact prior to sliding;
- when measured in stationary sliding, μ_d is not constant.

What happens in the real case is in fact that, for low enough velocity and when the coefficient of dynamic friction is less than the coefficient of static friction, non steady sliding of the block on the plane is observed, with the tendency for the motion to be intermittent rather than smooth. In fact, when the spring is pulled, the block will start to move if the tension is enough to overcome the force of the static friction; in other words, the two contact surfaces will stick until the sliding force reaches the value of the static friction. The surfaces will then slip one over another. Because the dynamic friction is far less than the static friction, the block moves at a velocity higher than that of the spring, rapidly restoring the spring to its unstretched length and causing the block to come to rest again. The entire process starts again, with the result shown in Figure 3.16-b. This mechanism of friction is known as *stick-slip*, and it has been widely analysed in the literature (see for example Heslot [1994] and Baumberger [2005]).

By performing this run at various spring velocities and making plots of position versus time, the trend we begin to see is that, the faster the spring velocity, the less jerky is the motion of the mass. The same is true when the two coefficients of friction approach the same value. Now, the case of the mass and spring may seem like a much localized case of stick-slip motion, but the fact is that even a stiff rod has some amount of elasticity and will stretch when it is pulled. Although the stick-slip mechanism may not be clearly visible to the eye, it will still occur at a reduced microscopic level.

The case of a magnet is identical. Every coil turn is held in place by frictional forces from neighboring turns; at a certain level of current and magnetic field, the electromagnetic force acting on this turn becomes greater than the restraining force: the turn will start to slip and the frictional rubbing of the turns provokes the stored energy to be dissipated in the form of a local pulse of heat (the movement of a turn or strand inside the magnetic field gradient may be itself responsible for current redistribution and possibly drive a local resistive transition). The same happens inside the cable, where we have to deal with a 90% compaction factor, which leaves the strands a 10% of free space to move through. It may be calculated that even a movement of few micrometers can generate enough heat to locally increase the temperature above the superconductor margin, leading to a quench (Wilson [1983]). It is important to observe that an intense electromechanical activity is always recorded in magnets during the current increase (as demonstrated by the continuous vibrations recorded by the quench antenna in Figure 3.6), which implies that there exists a threshold for quench activation.

It is now evident why the quenches at 1.9 K are always preceded by a spike, and what is the meaning of it: looking closer at the beginning of the resistive transition in Figure 3.6, we may recognize a rapid oscillation in the voltage, produced by a moving element in the coil (the damped elastic oscillation generated by the slipping superconductor has been emphasized by a blue line in Figure 3.17).

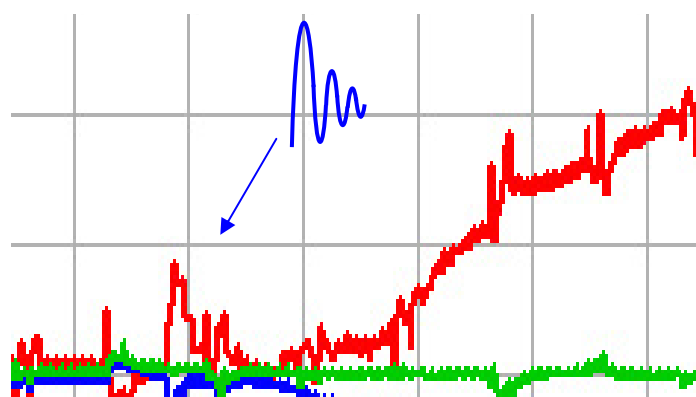


Figure 3.18 _ Beginning of a quench, preceded by what is interpreted as a rapid superconductor slipping oscillation.

To prevent the release of the electromagnetic energy and limit training, high pre-stresses in the collared coils are applied to the superconducting cables by means of the collars and a proper shimming on the separate layers; they are effective in reducing the degrees of freedom of all the strands, at least in the straight part. On the other hand, it may be argued that a certain degree of freedom for the coils could be an advantage, leaving them free to elastically adapt to the collar cavity, thus limiting the abrupt movements when a threshold current is reached. Rigidly limiting the freedom of the cables is nevertheless also a necessary requirement from field quality point of view, and this was chosen as the main criterion for the collaring pre-stress application.

Regardless of the precision used, it is however impossible to wind coils with a micrometric matching between all components, and the geometry itself poses sometimes serious problems on the compactness of the whole: filling materials have to be used in empty spaces between turns, such as glass fiber-reinforced epoxy or stycast. But several limitations are posed by their application, mainly because they are brittle and have a different thermal contraction than the superconductor. This means that cracks can be produced under the combined effect of cooling and energization, and the cracks can rapidly propagate in brittle materials and at the interfaces between organic materials and metals. It implies that we have to deal with the thermal strain energy besides the electromagnetic strain energy. For this reason, it is advisable to use impregnants which have a high work of fracture, with fillers or fibrous reinforcements to reduce thermal contraction and prevent crack propagation [Hartwig, 1984].

The mechanical activity of superconducting magnets was recorded many times in the past in the form of acoustic emissions produced during, for example, the formation of a crack. In recent times more sophisticated investigations were performed by Devred [1991], using the compensated voltage signals from the coils to record the wire motion during energization and determine the energy released by these events. After the application of quench antenna to the quench analysis, more detailed investigations could be performed; emblematic in this sense is a paper by Wilson [1997] on the calculation of the minimum quench energy.

Coming to LHC dipoles, Pugnât [2001] and Calvi [2004, 2006] provided statistical collections of the mechanical activity of superconducting coils, which justify the identification of quench origins in the mechanical instabilities associated to the frictional regime of these events. The charts representing the number of spikes with amplitude larger than a given threshold as a function of the threshold value show, for example, the same logarithmic behavior as in the case of friction experiments (Levent-Demirel [1996]).

Also the growing of the mechanical activity with increasing current and the memory each magnet preserves of the previous states (*i.e.*, once reached a certain level of current, lower excitation states are more stable and show a markedly reduced mechanical activity) reflect the solid friction regime and the friction memory phenomenon, first observed in stick-

slip motion by Kaiser [1950], and by Levent-Demirel and Hayward [2000] later on. The Kaiser effect indeed states that a material under load emits acoustic waves only after a primary load level is exceeded. During reloading, these materials behave elastically before the previous maximum load is reached. If the Kaiser effect is permanent for these materials, little or no acoustic emission will be recorded before the previous maximum stress level is achieved. Exactly the same effect was recorded on the LHC dipole magnets, exhibiting a behaviour similar to the one shown in Figure 3.18 (Calvi [2005]).

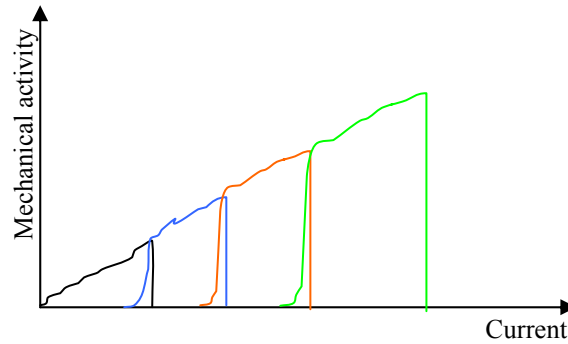


Figure 3.19 _ Example of Kaiser effect observed on the LHC dipoles.

All the observations and experimental results we have just mentioned justify the almost universally recognised belief that the stick-slip process is at the basis of the training phenomenon observed in superconducting magnets.

3.3.2. Mechanical constraints failure: one real case.

In this section, one case is presented where the mechanical constraints applied to the coils were overwhelmed by the strong electromagnetic forces and the magnet showed a lower than expected performance.

Following the poor quench performance exhibited by magnet 1026 (see Table 4) and the issued non-conformity report for cold tests and measurements, it was decided to disassemble this magnet to investigate possible assembly defaults or damages which could explain such a performance. After the disassembly of the cold mass of 1026 had been carried out by the producer, up to the de-collaring and separation of the two apertures, we decided to join the team at the premises to assist with the final stage of removal of the ground plane insulation and separation of the poles.

We first analysed all the non-conformities issued during the assembly of this magnet, and found no correlation between the faults detected on the poles during manufacturing in industry and the localization of the quenches during cold power tests.

TABLE 4 _ QUENCH TEST RESULTS FOR MAGNET 1026.

Test Sequence	Current [A]	Central B [T]	Aperture	Pole	Section
Training Quench#1	11441	8.05	D2	L	S01
Training Quench#2	11622	8.17	D2	L	S01
Training Quench#3	12096	8.49	D2	L	S13
Training Quench#4	12107	8.50	D1	U	S13-12
Training Quench#5	12385	8.69	D1	U	S13-12
Training Quench#6	12450	8.73	D2	L	S12
Training Quench#7	12572	8.81	D1	L	S01
Thermal cycle					
Training Quench#8	11662	8.20	D2	L	S01
Training Quench#9	12017	8.44	D1	L	S01
Training Quench#10	12502	8.77	D2	L	S01
Training Quench#11	12606	8.84	D2	L	S01
Training Quench#12	12698	8.90	D2	L	S12
Training Quench#13	12670	8.88	D2	L	S12
Training Quench#14	12796	8.96	D1	U	S13-12
Ramp to 9 T	12850	9.00	No quench		

Then, we began with the inspection of the poles, starting with the aperture D2 where all the quenches at low field values had been detected. We followed a systematic procedure for disassembly, and all the components were identified and stored. We performed a dimensional and number check for all the protection and insulating layers, and everything was found conformed to the specifications apart from some minor defects (Figure 3.19), not critical for the quench performance.

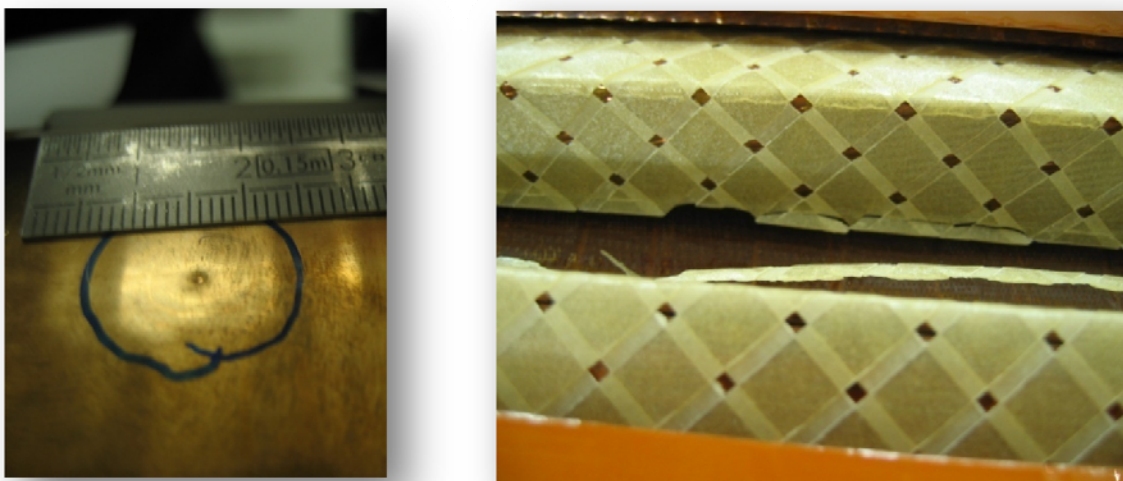


Figure 3.20 _ Example of defects detected upon disassembly of magnet 1026: deformation of the coil protection sheet (on the left) and breakages on the inter-layer spacer due to excessive azimuthal length.

Nonetheless, the breakages on the inter-layer spacer (due to an excessive azimuthal length) were then discovered to be the cause of the deformations of the cold bore tube during collaring, which were observed at 80 points along this magnet.

After removing all the insulation layers, the coil heads were free and we could observe the presence of a number of fractures in the Stycast between the G11 spacers on both heads and both poles. These fractures were either longitudinal (along the cables) or transversal (across the cables), as illustrated in Figure 3.20.

The same procedure was followed for the other aperture and similar fractures were observed in the Stycast.

Besides, some metrology observations were done which revealed a possible displacement of the G11 end spacers. We therefore asked to perform additional and more accurate measurements of the coil end dimensions (and we took this opportunity to review the measurement procedure).

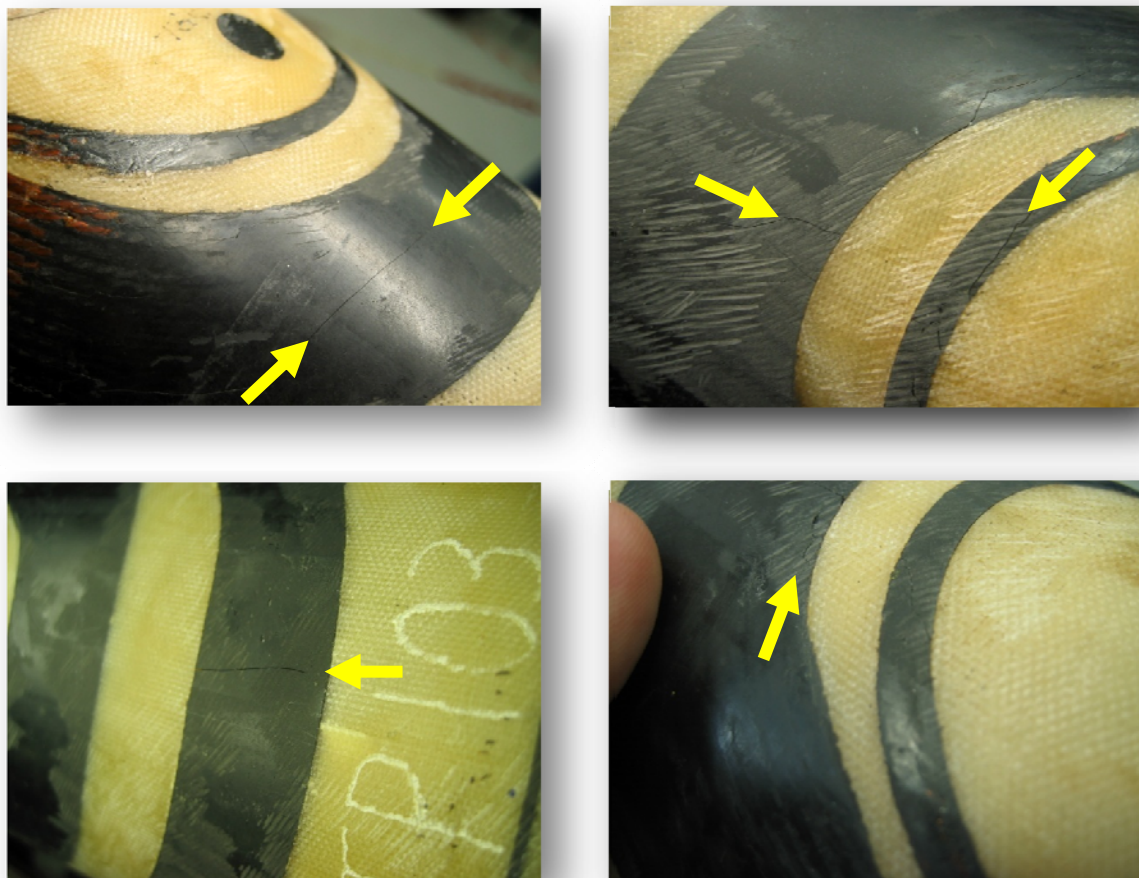


Figure 3.21 _ Fractures, observed on pole heads, on the stycast between G11 spacers.

The press relies on a cavity into which each pole is inserted (inner plus outer layers) and each side of each layer is measured independently. Measurements are carried out at three locations over 10 cm, centred in the middle of the head (90 mm away from the end). These three values are averaged and a global shim is evaluated for the coil end. Furthermore, to ensure a smooth transition between the ends and the straight section, the shim is graded in three diminishing steps, starting from coil end.

For each pole produced, a pressure-displacement curve is measured at different pressures to extrapolate the value at 30 MPa, which corresponds to the nominal pressure applied by this manufacturer over the coil ends. The objective of this measurement is to determine the shim to be added so as to reach 30 MPa. The result of this exercise was that, in some cases, for coils which had dimensions much smaller than the nominal ones or where the determination of the value at 30 MPa was not univocal, the extrapolation was not precise. In these cases, the procedure defined by the producer was to apply a nominal shim of fixed thickness (0.375 mm).

In order to cross-check the thicknesses of the shims, we systematically re-measured the heads of the four poles of magnet 1026 and we recomputed all the shims. The difference between the shims that were implemented in the magnet and the shims recomputed from the data, after disassembly, for each side of each aperture, was quite small for the inner layers, but a bit large (up to 1 mm) for the outer layers. This might indicate that the target of 30 MPa was not achieved during collaring or that the standard shim (applied to all four outer layers) was not adapted to the present case.

The most striking observations were made when we separated the two layers at the non-connection side end to inspect the inner surface of the outer layer and the outer surface of the inner layer. First, we observed on some poles that there were unexpected Stycast deposits on the inner surface of the outer layer. These deposits were likely to come from the fact that the mold used for resurfacing was not tightly closed, thereby resulting in over-thicknesses and preventing the pole assembly to assume its nominal shape.

Second, we clearly observed some cracks in the Stycast or deep delaminations between the first and second cable, or second and third cable, or even third and fourth cable, as illustrated in Figures 3.21. The depth of the delamination was, in some cases, estimated to exceed 10 mm. The extent of the delaminations was clearly exacerbated by the stresses applied to the layers to separate them, but were not caused by the separation and were present from the beginning.

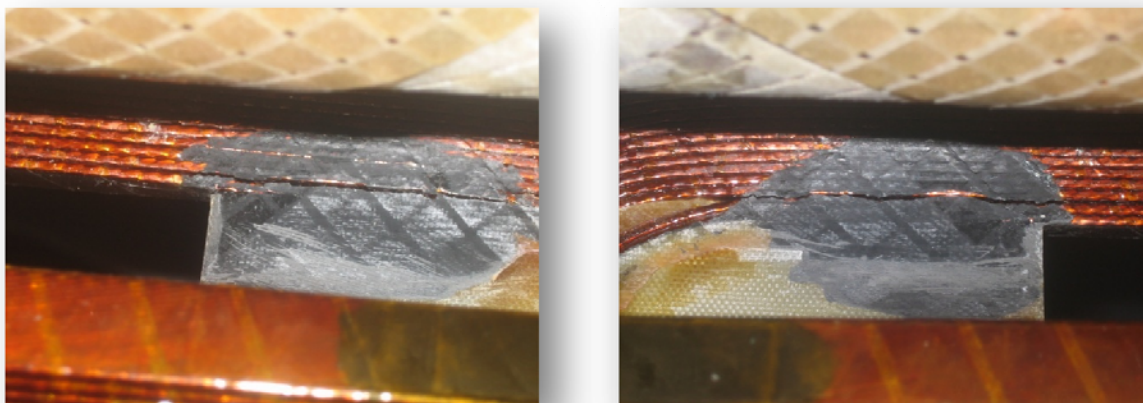


Figure 22 _ Defects discovered during separation of the poles used in magnet 1026.

3.4. SOME REMARKS.

Performance and safety are intimately related in the LHC dipoles. The energy stored in the magnets is so huge that even a small defect can have dramatic consequences on the hardware. Preventing or limiting the quench activity is, therefore, vital; as well as detecting and understanding the dynamics at the origin of a premature quench is fundamental.

The solid friction, with the associated energy release, is at the basis of the quench phenomenon at 1.9 K: the coils must be tightly constrained to tolerate the high Lorentz forces, and detailed assembly procedures, with precise pre-stress values, must be applied. Not complying with these criteria leads to serious limitations in magnet performance and eventually to material damages.

Also, the quenches performed around 4 K have demonstrated to be a valuable instrument to detect assembly faults, and have confirmed the budget in temperature margin for the operation. They have, nevertheless, highlighted the systematic difference between critical current and quench current, whose origin is not easy to determine differently from degradation in magnet assembly.

BIBLIOGRAPHY

- Amontons G., “*Histoire de l'Académie Royale des Sciences avec les Mémoires de Mathématique et de Physique*”, p.206, 1699.
- Ašner F., “*High Field Superconducting Magnets*” Oxford University Press, 1999.
- Baumberger T. and Caroli C., “*Solid Friction from Stick-slip to Pinning and Aging*”, arXiv:cond-mat/0506657v1, Jun 2005.
- Benda V. et al., “*Experience with a Pre-series Superfluid Helium Test Bench for LHC Magnets*”, in Proc. ICEC18, Mumbai, India, 2000.
- Billan J. et al., “*Twin Rotating Coils for Cold Magnetic Measurements of 15-m Long LHC Dipoles*”, IEEE Trans. Appl. Supercond., vol. 10, no. 1, pp. 1422–1426, March 2000.
- Bottura L. et al., “*Performance of the LHC Final Prototype and First Pre-series Superconducting Dipole Magnets*” IEEE Trans. Appl. Supercond., vol. 12, no. 1, pp. 211–214, March 2002.
- Bottura L. and Henrichsen K.N., “*Field Measurements*”, CERN LHC/2002-20. Lecture given at the CAS School on Superconductivity and Cryogenics for Particle Accelerators and Detectors Erice, Sicily, 8-17 May 2002.
- Calvi M. et al., “*Statistical analysis of conductor motions in the LHC dipole magnets*”, IEEE Trans. Appl. Supercond., vol. 14, no. 2, June 2004.
- Calvi M., Private communication [2005].
- Calvi M., Agrisani L., Bottura L., Masi A. and Siemko A., “*On the Use of Wavelet Transform for Quench Precursors Characterization in the LHC Superconducting Dipole Magnets*”, IEEE Trans. on Appl. Supercond., Vol. 16, No. 2, June 2006.
- Coulomb C. A., “*The Theory of Simple Machines*”, Mem. Math. Phys. Acad. Sci., 10: 161-331 (1785).
- Dahlerup-Petersen K. (CERN), Kazmine B., Popov V., Sytchev V., Vassiliev L. and Zubko V. (IHEP), “*Energy Extraction Resistors for the Main Dipole and Quadrupole Circuits of the LHC*”. EPAC 2000, Vienna, Austria.
- Devred A., “*Quench Origins*”, US Particle Accelerator School - Physics of particle accelerators, Berkeley, CA, Upton, NY, Cambridge, MA and Hilton Head, SC, USA, 19 - 30 Jun 1989; 24 Jul - 4 Aug 1989; 11 - 22 Jun 1990 and 7 - 14 Nov 1990 - pages 1262-1308.
- Devred A., Ogitsu T. and Tsuchiya K., “*Investigation of Wire Motion in Superconducting Magnets*”, IEEE Trans. on Magnetics, vol.27, No.2, March 1991.
- Hartwig G., Knaak S., “*Fibre-epoxy composites at low temperatures*”, Cryogenics ISSN 0011-2275 CODEN CRYOAX, vol. 24, no11, pp. 639-647 (1984).
- Hayward V. and Armstrong B., “*A New Computational Model of Friction Applied to Haptic Rendering*”, Experimental Robotics VI, Lecture Notes in Control and Information Sciences, volume 250, pages 403–412. Springer Verlag, Heidelberg, Germany, 2000.

- Henrichsen K.N., “*Overview of Magnet Measurement Methods*”, CERN 98-05 CAS, Anacapri, Italy 11-17 April 1997.
- Heslot F., Baumberger T., Perrin B., Caroli B. and Caroli C., “*Creep, Stick-slip, and Dry-Friction Dynamics: Experiments and a Heuristic Model*”, Phys. Rev. E 49, 4973 - 4988 (1994).
- Kaiser J., “*Untersuchungen über das auftreten Geräuschen beim Zugversuch*”, Ph.D. thesis, Technische Hochschule, Munich (1950).
- Lefèvre P., Pettersson T. *et al.*, “*The Large Hadron Collider – Conceptual Design*”, CERN/AC/95-05 (LHC), Geneva 20 October 1995.
- Leroy D., Krzywinski J., Remondino V., Wakckiers L., Wolf R., “*Quench Observation in LHC Superconducting One Meter Long Dipole Models by Field Perturbation Measurements*” IEEE Trans. on Appl. Superconductivity, Vol. 3, No. 1, pp. 781-784, March 1993.
- Levent-Demirel A. and Granick S., “*Friction Fluctuations and Friction Memory in Stick-slip Motion*”, Phys. rev. lett., vol. 77, no21, pp. 4330-4333, 1996.
- Lubell M.S., “*Empirical Scaling Formulas for Critical Current and Critical Field for Commercial NbTi*”, , IEEE Transactions on Magnetism 19, p. 754, 1983.
- Pugnat P., Khomenko B., Rijllart A., Sanfilippo S. and Siemko A., “*Statistical Diagnosis Method of Conductor Motions in Superconducting Magnets to Predict their Quench Performance*”, IEEE Trans. on Appl. Supercond., vol. 11, no. 1, pp. 1705–1708, 2001.
- Rodriguez-Mateos F. *et al.*, “*Quench Heater Experiments on the LHC Main Superconducting Magnets*”, EPAC 2000, Vienna, Austria.
- Rodriguez-Mateos F. and Sonneman F., “*Quench Heater Studies for the LHC Magnets*” in Proceedings of the 2001 Particle Accelerator Conference, Chicago, USA, pp. 3451–3453.
- Siemko, A. *et al.*, “*Quench Performance and Field Quality of the LHC Pre-series Superconducting Dipoles*” IEEE Trans. Appl. Supercond., vol.14, no. 2, pp. 165–168, 2004.
- “*Technical Specification for NbTi Superconducting Cables for LHC Superconducting Long Dipole Models*” – IT 2483/LHC/LHC-May 1997.
- Verweij A.P., “*Electrodynamics of Superconducting Cables in Accelerator Magnets*”, Ph.D. thesis, Univ. Twente, The Netherlands, 1995.
- Verweij A.P., “*Review on boundary-induced coupling currents*”, Adv. Cryog. Eng. 44B, pp.1059–1068 (1998).
- Verweij A.P., private communication, 2006.
- Wilson M. N., “*Superconducting Magnets*”. Clarendon Press – Oxford, 1983.
- Wilson M.N. and Wolf R., “*Calculation of Minimum Quench Energies in Rutherford Cables*”, IEEE Trans. on Appl. Supercon., Vol.7(2), pp. 950-953, 1997.

CHAPTER 4
STATISTICAL TREATMENT OF
SERIES DIPOLE QUENCHES

4.1. TECHNICAL SPECIFICATION FOR THE SUPPLY OF THE COLD MASSES.

4.1.1. Room temperature acceptance tests.

A technical specification for the assembly and supply of the cold masses of the dipole magnets [LHC Project, 2001] was prepared at CERN to manage the series production, both as a guideline and a definition of the assemblers' responsibilities. As such, it contains the definition of all magnet parameters, their tolerances and the criteria for the magnet acceptance. In particular, since the successful operation of the machine is based on the good reproducibility of their magnetic characteristics, it is stated that the relative variations of the integrated field and the field shape imperfections can not exceed the order of magnitude of 10^{-4} and that their reproducibility must be within a fraction of 10^{-4} . As we mentioned in chapter 3, these high precision are attained by means of accurate coil geometry, reproducible and symmetric to within a few hundredths of millimetre. To achieve this accuracy, tolerances ranging from $\pm 2 \mu\text{m}$ to $\pm 20 \mu\text{m}$ were fixed on the dimensions of coil components, tolerances of $\pm 0.03 \text{ mm}$ on the average transverse dimensions of the finished coils and $\pm 0.02 \text{ mm}$ on the critical dimensions of the fine-blanked austenitic steel collars, surrounding and supporting the coils.

To reach this high precision, rigorous procedures and systematic checks were applied to all production phases, both on the single components and during the assembly of the cold masses, followed by a series of final verifications on the completed cold masses, which include, in particular, the following steps:

- verification of the integrity of the electrical insulation and impedance of various circuits;
- geometrical measurements accurate to within 0.1 mm r.m.s. of horizontal curvature, vertical straightness, position of the ends of cold bore tubes and of other outlets for magnet interconnection, position of the support bases, minimum inner diameter of cold bore tubes;
- the measurement of tilt of the magnetic mid-planes, parallelism of the field direction in the two apertures;
- the measurement of magnetic field quality and integrated field strength, to allow the possibility of fine tuning the magnetic length (changing the number of magnetic laminations in the yoke blocks);
- examination of welded joints;
- room temperature pressure and leak tests.

After successful completion of the provisional room temperature acceptance tests and cryostating, the cryo-magnets were submitted to a series of acceptance tests at liquid helium temperature; they, again, first concern the verification of the electrical insulation integrity and the optimal magnetic characteristics of the assemblies, but also aim at verifying the structural stability of the magnets, that is the absence of any coil movement causing quenches, or, at least, the presence of a reduced training. This is, once more, important for magnets operated at 1.9 K, where the material exhibits little effective heat capacity and any energy dissipated must be removed via superfluid helium.

4.1.2. Acceptance tests at liquid helium temperature.

All the intermediate tests which are summarized in a defined Inspection and Test Plan (a part of the Quality Assurance plan, the manufacturers have to comply with) had the objective to detect defects as early as possible during the assembly stages, to give the possibility of applying the proper corrective actions and saving time and material. The magnetic field measurements at room temperature are also a powerful tool to control the quality of the production and to steer the field quality towards the beam dynamics target. It is based on these controls (and the warm-cold correlations) that the cross-section of the dipole aperture was changed twice, modifying the shape of one copper wedge in the inner layer and increasing the shimming on the mid-plane, to reduce out-of-tolerance multipolar components [Ferracin, 2001 - Todesco, 2003].

Magnetic field quality measurements are also performed during the acceptance tests at liquid helium temperature, to draw, at the beginning of the production, a correlation between warm and cold measurements and to check its stability in the course of production. The acceptance tests are nonetheless performed to ensure the safe and reliable operation of the magnets, assuring that the working limit defined for the machine can be attained with a reduced effort.

The acceptance checks performed at cold mainly consist in:

- hydraulic tightness and cold leak test;
- integrity and impedance measurements of instrumentation and power circuits, which include the inter-turn and ground electrical insulation of the windings;
- performance of the quench heaters;
- measurement of the transfer function, linking field strength to current;
- quench performance tests.

The quench performance tests qualify magnet performance in terms of the number of training quenches necessary to reach the nominal (8.33 T) and the ultimate (9 T) field levels,

and of the magnet property to keep a “memory” of the training process after a thermal cycle. The acceptance criteria which were fixed at the beginning of the series production are the following:

1. the cryo-dipole shall reach the ultimate field after no more than eight quenches
2. cryo-dipoles that reach the ultimate field with a number of quenches between three and eight may be submitted to a thermal cycle after which they shall reach the field of 8.6 T without any quench.

The threshold values and the maximum number of quenches were established based on the experimental results obtained on the first prototype magnets, which had proven that the operation of the machine at nominal field is feasible and that the commissioning without beam should not take too long.

As already mentioned in chapter 3, quenches at temperatures around 4 K were also used as a qualification instrument, to identify possible impoverishment in critical current of the cables used to wind the magnets, or degradation of the splices joining poles and layers.

The quench acceptance criteria were reviewed at different moments during magnets production and streamlined in a reduced test program. In March 2004, due to a delay in cold testing of the magnets and the accumulation of a backlog of nearly 100 units, it was decided to speed up the reception tests; the quench criteria were modified as follows:

1. cryo-dipoles reaching 8.4 T within two quenches are accepted and the cold tests stopped
2. cryo-dipoles reaching 9 T with a maximum of eight quenches are accepted and the cold tests stopped
3. if 2. and 3. are not satisfied, temperature will be raised to 4.2 K and quench attained;
 - i. if eventual faults of cable or splices are detected, reject the magnet
 - ii. if no problem is detected, go on with thermal cycle.

The relaxation of some constraints with respect to the previous version (i.e., acceptance of magnets reaching 8.4 T, without having attained 9 T) was the compromise between the requirement of proving the capability of magnets to work at least at the nominal field^a and the necessity of reducing the time spent on test benches: the thermal cycle was in this formulation required only for magnets showing unsatisfactory quench performance and as a diagnostic instrument.

In 2005, a three quench criterion was finally defined with a field threshold of 8.6 T and the same rule to perform additional training quenches after the thermal cycle.

^a The limited training of the magnets should not be a concern for the commissioning of the machine, thanks to the good memory effect, which guarantees that the 8.33 T should be reached without retraining.

4.1.3. Diagnosis of non-conformities.

In Table 4.1, a list of non-conformities [Tommasini, 2007], discovered in industry and at CERN on the LHC dipoles, is shown; it is the result of the quality assurance policy established for the production of these magnets.

TABLE 4.1 _ LIST OF NON-CONFORMITIES FILED
FOR THE LHC DIPOLE MAGNETS.

Type of non-conformity	Number of NC
Factory	3385
Electrical	583
Mechanical	1181
Quench performance	94
Vacuum vessel	1609
Other	356
TOTAL	7208

The checks performed in industry, at the different stages of production, made it possible to identify the problems and their origin in an early phase, leading to a solution of most of these non-conformities in a very short time; the acceptance of the magnets was therefore achieved with minor cost and time delay. In some cases, the deviation of the magnetic components, measured in the assembled collared coils, lead to effective corrective actions. Quite rarely, the coils had to be discarded due to faults in assembly.

In other cases, special instruments for diagnosis were developed to investigate weak points or anomalous behaviours. It is the case, for example, of the analysis of poles where the winding resistance dropped sharply during collaring: an inter-turn short-circuit was developed. Conventional diagnostic instruments did not fit the requirement of a precise localization of the fault, and an ad hoc electro-mechanical model was developed [Bellesia, 2006] to identify the position with a few centimetres precision, helping in efficiently and cheaply repairing the fault.

Different is the case, mentioned in chapter 3, of the destructive quench originated from an inter-turn short, where the fault was unfortunately discovered too late; it was, nevertheless, useful to identify a weakness in the procedure, up to that moment applied, for the high voltage insulation qualification.

Another example of post-mortem analysis, whose diagnosis served the correction of a factory fault, concerned the quench heater circuit of one of the first pre-series dipoles (magnet 2002): after the first cool-down and during the electrical continuity test, an electrical fault was

detected. During the discharge of the quench heaters up to the nominal 900 V, in fact, a weak insulation was detected in the circuit. Resistance and inductance measurements were performed at liquid helium temperature and at warm conditions [Pugnat, 2002] to identify the fault position, followed by the disassembly of the magnet at the manufacturers' premises. The result of this autopsy is shown in Figure 4.1: the quench heater appears to be burned and the insulation is consequently heavily damaged. Further investigations lead to the idea that a mechanical over-tensioning of the quench heater on magnet end, due to an excessive and point sharp transition of the shimming in this part, had torn one quench heater strip; the following energization was responsible for the burning of the quench heater and for the damage of the insulation layer. Also in this case, an important feedback on shimming procedure and insulation test parameters, were drawn by this accident. The same magnet was reassembled and successfully tested.

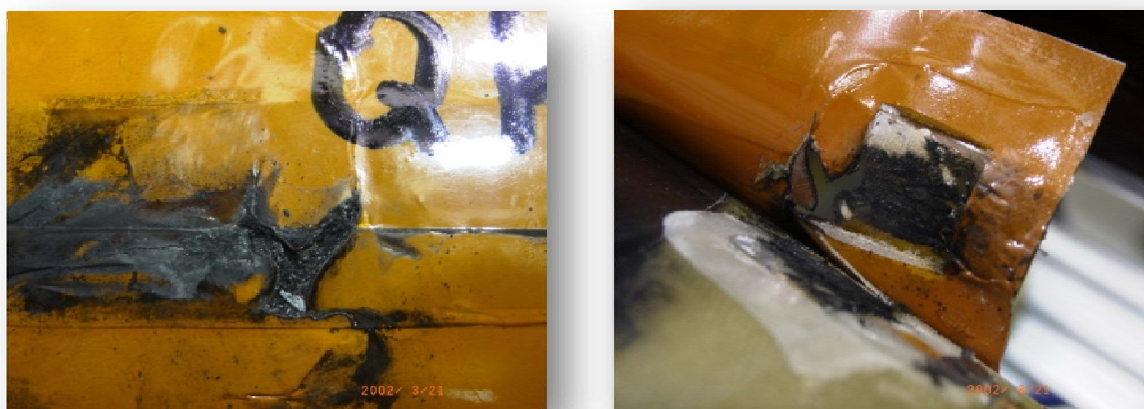


Figure 4.1 _ Quench heater accident on magnet 2002: one QH strip was torn and burned during energization.

Many other cases could be mentioned (as the high contact resistance found in the diode bus-bars connections [Floch, 2003]), but the necessity of a detailed quality assurance process has already become evident.

4.2. QUENCH RESULTS FROM THE COLD TEST OF 1261 DIPOLES AT 1.9 K.

In the following paragraphs, the results on quench performance of all magnets produced in industry in the period 2001-2006 and tested at CERN until the beginning of 2007, are shown. The distinction between a global performance statistics, taking into account all magnets, and the analysis of only those magnets selected for the machine, is done; the first one being of relevance for production statistics analysis, the second one bearing an important role in the assessment of the operation of the machine.

4.2.1. Global magnet performance.

The number of non-conformities of Table 4.1 may appear very large if we don't think about the complexity of the mechanical and electrical design of the magnets. Indeed, the performance of series production is quite remarkable. In particular, when we look at the quench performance of the dipoles, we can notice that only nearly 1.4% of tested magnets were rejected because of bad or reduced performance: to select the 1232 dipoles to be installed in the tunnel, a total of 1261 magnets were tested. This does not mean that 29 magnets were thrown away: the poles (and above all the superconductor they are made from) constitutes, in fact, nearly half of the price of a cold mass; whenever possible, and always when the dipole was not performing well for reasons not related to the conductor, its poles were used in another collared coil, after having solved its electrical or mechanical problems.

Among the discarded magnets, not all of them had degraded characteristics: 3 were used in the String2 experience [Bordry, 2002], magnet 3004 had the problem of weak insulation we have several times mentioned, one had to be re-assembled due to an accident during storage and a few magnets had instrumentation problems; magnet 1011 was selected for reference magnetic measurements, since its performance were very good and it was successfully trained up to 13 kA (9.11 T). The others (18 in total) were sent back to the producers, because of a long training, or an excessive detraining, or again their incapacity to reach 8.4 T rapidly after the thermal cycle. Another one, which had already been installed in the tunnel, was replaced in September 2007: an *a posteriori* analysis of the quench data taken in SM18 revealed, in fact, a possible fault of the insulation similar to the one at the origin of the problem of magnet 3004; to prevent any risk, its replacement was carried out.

Among the rejected magnets, only one (1005) was discarded because it was not able to reach the nominal field level: it was in fact limited to 6.1 T. By means of the quench antennas, the exact localisation of the quench start position was detected and found to be identical for all quenches; a post mortem analysis of the disassembled magnet revealed a conductor cold weld at the basis of the current limitation.

The tests of 7 more magnets were stopped right before the cool-down or at the end of it, due to the occurrence of short-circuits or because of instrumentation problems. All of them were opened and repaired.

The global performance of all tested magnets in terms of the number of quenches to reach 8.33 T and 9 T, before and after the thermal cycle, is given in Table 4.5 to Table 4.8, for the three producers separately (01, 02 and 03) and for the sum of them. In these tables, the first value in each cell refers to the dipoles installed in the LHC tunnel only, while the second one takes into account also the discarded magnets. The same values can be found in the charts presented in Figure 4.2 to Figure 4.5. A quantitative analysis will be given in the next paragraph only on the 1232 magnets installed in the machine, due to their relevance for the accelerator commissioning.

In addition, Figure 4.6 to Figure 4.8 show all quenches during the first powering of all dipoles from the three producers, plus the first two quenches after thermal cycle, if any. Looking at these charts, it is possible to observe the difference between the three firms: firm 01 has a very good stability in production, evidenced by the small fluctuations of the running averages (over ten points) of the first and second quench during first cool-down; which is not the case for the other two, especially for firm 03, where the fluctuations are continuous and wider. Secondly, producer 01 has also a better compaction of quenches towards high field values, with a minimum field of 7 T in the worst cases. Producer 03 has instead the widest distribution of first quench points, with many magnets that first quenched at values closed to 6 T. In all three cases, nevertheless, the running average of the first and the second quench follow each other, indicating that magnet geometry and its constraints are very stable and only slightly perturbed by the seismic motion of a quench. This is probably at the origin of the reduced training and of the good memory effect of the LHC dipole magnets.

It would be certainly possible to try and reconstruct the faults at the origin of sudden changes in production (as it is the case, for example, of magnet 1026 and its neighbouring, which we have treated in chapter 3) but, as we have seen, the link between quench performance and mechanical defects is not always so easy to draw.

4.2.2. Performance of the magnets selected for the machine.

Even if, from a purely statistical point of view, small is the difference between the analysis of the whole production of dipoles and of the group of those installed in the LHC tunnel, only the last ones will have an importance during the commissioning and the operation of the machine. It is to this sample that every statistical analysis has to be therefore referred. And it is to the first value of each cell in Table 4.5 to Table 4.8 that one has to look at.

In particular Table 4.5 and Table 4.6, together with Figure 4.2 and Figure 4.3 are relevant for this purpose. Figure 4.2 shows that 80% of magnets reached 8.33 T within a single quench (more or less half of them without any quench). Statistically, this is mainly due to the good performance of producer 01, for which nearly 55% of the magnets reached 8.33 T without quench. This proportion is also evident from the results listed in Table 4.2, which contains the average value of the distribution of quenches for the three producers at the different field levels: producer 01 has the distribution of quenches to attain 8.33 T centred on 0.60 (i.e. 0.6 quenches in average to reach nominal field for this firm); producer 02 is the worst according to this criterion, with an average value of 1.1 quenches per magnet. Furthermore, and more important, only 4% of all magnets needed 3 quenches or more to reach 8.33 T.

These considerations, together with the fact that only one magnet in general was not able to reach 8.33 T (but only because of conductor limitations and discarded because of them), prove that the nominal field selected for the accelerator is well managed by this technology; and this with a fairly reduced training. It is even more evident when we look at

the results after thermal cycle: nearly 83% of the magnets submitted to a second cool-down, reached nominal field level without quenching. This is also confirmed by the average value, which reduces to 0.21 quench per magnet. Differently from the first powering, after thermal cycle the magnets produced by firm 03 are those needing the longest training.

The small percentage value, indicating those magnets needing training, is really promising for a rapid commissioning of the dipoles in the tunnel, keeping nevertheless in mind that a big amount of them (1116 dipoles) were not submitted to a second cool-down.

Different is the case of the 9 T field value, limit up to which the LHC dipole magnets were designed to work. Very few magnets, in fact, reached ultimate field without quenching and nearly 55% required 1 or 2 quenches; but, above all, 35% needed a longer training and 10% of the magnets that were pushed up to the maximum of nine quenches, never reached the ultimate field during the first cool-down (for more than 40% of the magnets, in fact, the criterion of stopping the training once attained 8.33 T was applied). The situation is even worse if we take the values of Table 4.8: 64 over 116 magnets submitted to a thermal cycle did not reach 9 T within at least two quenches. It does not mean that 9 T cannot be obtained with these magnets, but they would certainly require a long training.

With the aim of further verifying their capability of keeping the memory of the field level reached, 21 magnets were submitted to a third cool-down: they confirmed that, once trained, they can attain the nominal field level without training; but they also provided more evidence that the ultimate field could only be achieved with a sometimes long training. One magnet was also submitted to this third cool-down after one year of outdoor storage, to check the possible relaxation of pre-stress and de-training effects: the results [Seyvet, 2006] show that, a part from a minor reduction of the first quench, the structure perfectly maintains its geometrical characteristics over time, which is important for a machine designed to work for over 20 years.

This discussion is obviously missing one element, which is essential when speaking about particle accelerators: the circulating beams (with energy deposition via beam losses) will degrade the performance of the superconductor, rendering the achievement of the nominal 7 TeV energy even tougher. It is anyway not the objective of this thesis to discuss about beam-related problems and we send the reader to more specialized writings.

TABLE 4.2 _ CENTRE VALUE FOR THE QUENCH DISTRIBUTION FOR THE THREE PRODUCERS WITH RELATIVE ERRORS.

Field level (1.9 K)	Total	01	02	03
8.33 T	0.87±0.93	0.60±0.78	1.09±1.04	0.91±0.95
9 T	2.54±1.59	2.32±1.52	2.75±1.66	2.50±1.58
8.33 T ATC	0.21±0.45	0.14±0.38	0.18±0.43	0.31±0.56
9 T ATC	1.26±1.12	0.85±0.92	1.39±1.18	1.43±1.20

4.2.3. Statistics on longitudinal distribution of quenches.

One of the main improvements in the design of the LHC dipoles during the prototype phase was the change from five to six sectors in one quadrant cross-section of the aperture; this was, indeed, effective in reducing the quenches in the straight part along the magnet length, where they were previously concentrated due to a higher peak field on the superconductor. At the same time, to avoid quenches on magnet ends, special yoke laminations were implemented over the last centimetres of both collared coil sides, which replace normal iron laminations with others having the central part made of stainless steel. This trick enables a reduction of the field on magnet ends, where electro-mechanical stability is an issue, due to the complex structure made of several superconductor-vetronite interfaces. The result of these two design solutions can be seen in Table 4.3 for the LHC dipole series production.

In fact, thanks to the quench antennas that sometimes^b instrument the magnets (to measure the multipolar components of field and to identify the longitudinal position of quench starting point), it is possible to analyse the distribution of quenches along both magnet apertures. If we look at Table 4.5, some interesting conclusions can be drawn on quench distribution and on the relative concentrations. First of all, differently from the 5 sectors design, the quenches are mainly concentrated in the extremities, but they are not completely absent from the straight part. Secondly, there is a great difference between the three producers on the distribution of quenches in ends: firm 01 has, indeed, an equal distribution on both sides, while the proportion changes to 1-to-2 for firm 02 and 1-to-4 for firm 03, where more quenches are located in the non-connection side than in the connection side end, despite the greater complexity of the latter, which includes cables connection and the layer jump. This could indicate that, in the case of firm 02 and 03, the pre-stress application on the connection side end is better managed than on the non-connection side.

TABLE 4.3 _ NUMBER OF QUENCHES AT 1.9 K AS A FUNCTION OF THE LONGITUDINAL POSITION.

Sector	1 (n-c s) ⁱ	2	3	4	5	6	7	8	9	10	11	12	13 (c s) ⁱ
Firm 01	114	1	2	2	4	5	0	1	14	1	4	18	114
Firm 02	137	5	5	5	3	3	2	0	0	4	1	20	77
Firm 03	209	13	1	3	1	0	1	0	2	1	1	9	53

ⁱ *n-c s* and *c s* stand for *non-connection side end* and *connection side end*, respectively.

^b At the origin of the production, all magnets were instrumented with quench antennas; the reduction of test time lead also to the decrease of magnets tested for magnetic measurement and therefore instrumented with the antennas.

A number of quenches appear also located in sector 12, where the layer jump starts and the field decreases. This position was also identified as a weak point during quenching at 4 K, possibly due to the transition from low to high field.

Another important information can be extracted from the analysis of the number of quenches per aperture and per pole, in both magnet ends. The main result is that there is no particular asymmetry in quench distribution between one aperture and the other, neither between upper and lower poles (with an almost exact quench concentration). This is true for the sum of all quenches as well as for the quenches divided by ranges of field. This means that there is apparently a perfect symmetry between all four poles, as could be expected. Unfortunately, a right/left asymmetry in each aperture (which could be produced by the geometrical and magnetic differences between facing and opposite parts of the winding, or by the presence of the splices) could not be identified, due to the absence of orthogonal pick-up coils in the quench antennas.

TABLE 4.4 _ DISTRIBUTION OF QUENCHES AT 1.9 K BETWEEN APERTURES AND POLES ON MAGNET ENDS.

B range	Firm	D1				D2			
		S01		S13		S01		S13	
		U	L	U	L	U	L	U	L
< 7	01	0	0	0	0	0	0	0	0
	02	0	0	1	0	2	1	0	1
	03	2	1	0	0	0	2	0	1
7-8	01	2	3	0	1	3	0	1	3
	02	11	6	2	3	8	5	6	4
	03	10	5	2	2	8	4	3	0
8-8.33	01	5	10	1	3	1	7	2	5
	02	4	3	2	6	6	6	4	6
	03	4	4	2	1	13	6	0	2
8.33-8.60	01	8	10	5	7	1	6	6	9
	02	10	2	2	9	6	8	2	4
	03	6	8	5	2	24	5	2	3
8.60-9	01	19	12	18	18	11	16	14	21
	02	16	16	6	8	13	14	3	8
	03	24	27	11	8	33	23	6	3

TABLE 4.5 _ NUMBER OF QUENCHES AT 1.9 K TO REACH **8.33 T**.

No of quenchs	Total	01	02	03
0	478 / 484 ^a	224 / 227	87 / 88	167 / 169
1	515 / 522	142 / 144	222 / 225	151 / 153
2	190 / 200	32 / 35	84 / 90	74 / 75
3	33 / 35	9 / 10	11	13 / 14
4	10 / 12	2	3 / 4	5 / 6
5	4 / 5	0	2 / 3	2
6	1	1	0	0
7	1	0	0	1
not reached	0 / 1	0 / 1	0	0
TOTAL	1232 / 1261	410 / 420	409 / 421	413 / 420

^a The first value in each cell refers to the installed magnets, while the second one takes into account all the tested magnets.

TABLE 4.6 _ NUMBER OF QUENCHES AT 1.9 K TO REACH **8.33 T** AFTER THERMAL CYCLE.

No of quenchs	Total	01	02	03
0	96 / 103 ^a	31 / 34	41 / 44	24 / 25
1	16 / 24	3 / 7	7 / 10	6 / 7
2	4 / 5	1	1 / 2	2 / 2
3	0 / 1	0	0	0 / 1
4	0	0	0	0
5	0	0	0	0
more than 5	0 / 1	0	0	0 / 1
No TC	1116 / 1125	375 / 378	360 / 363	381 / 384
not reached	0 / 2	0	0 / 2	0
TOTAL	1232 / 1261	410 / 420	409 / 421	413 / 420

^a The first value in each cell refers to the installed magnets, while the second one takes into account all the tested magnets.

TABLE 4.7 _ NUMBER OF QUENCHES AT 1.9 K TO REACH 9 T.

No of quenches	Total	01	02	03
0	10	3	0	7
1	188 / 191 ^a	53 / 54	41	94 / 96
2	186 / 187	62	76	48 / 49
3	76 / 77	8 / 9	35	33
4	49 / 50	11 / 12	21	17
5	47 / 49	8 / 9	17	22 / 23
6	27 / 28	4	9 / 10	14
7	22 / 23	8	6 / 7	8
more than 7	26 / 28	7	11 / 13	8
not reached	73 / 87	24 / 28	30 / 37	19 / 22
8.4 T criterion	528 / 531	222 / 224	163 / 164	143
TOTAL	1232 / 1261	410 / 420	409 / 421	413 / 420

^a The first value in each cell refers to the installed magnets, while the second one takes into account all the tested magnets.

TABLE 4.8 _ NUMBER OF QUENCHES AT 1.9 K TO REACH 9 T AFTER THERMAL CYCLE.

No of quenches	Total	01	02	03
0	15 / 18 ^a	7 / 10	5	3
1	16	2	8	6
2	12 / 13	3	7 / 8	2
3	5 / 6	1	2	2 / 3
4	2 / 4	0 / 1	1 / 2	1
5	0	0	0	0
more than 5	2	2	0	0
No TC	1116 / 1125	375 / 378	360 / 363	381 / 384
not reached	64 / 77	20 / 23	26 / 33	18 / 21
TOTAL	1232 / 1261	410 / 420	409 / 421	413 / 420

^a The first value in each cell refers to the installed magnets, while the second one takes into account all the tested magnets.

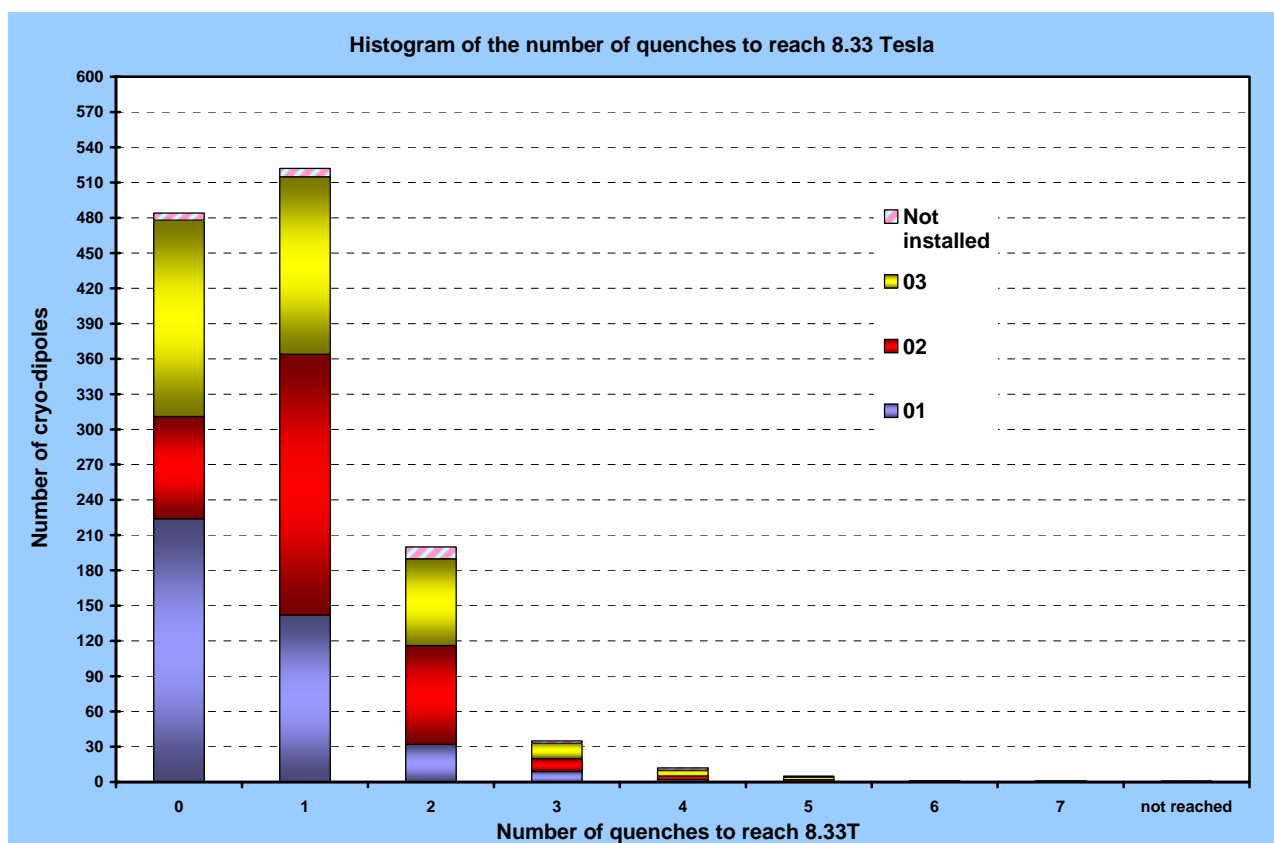


Figure 4.2 _ Cumulative number of magnets as a function of the number of quenches to reach 8.33 T, for the three producers. Those dipoles not installed in the tunnel are also added to the plot.

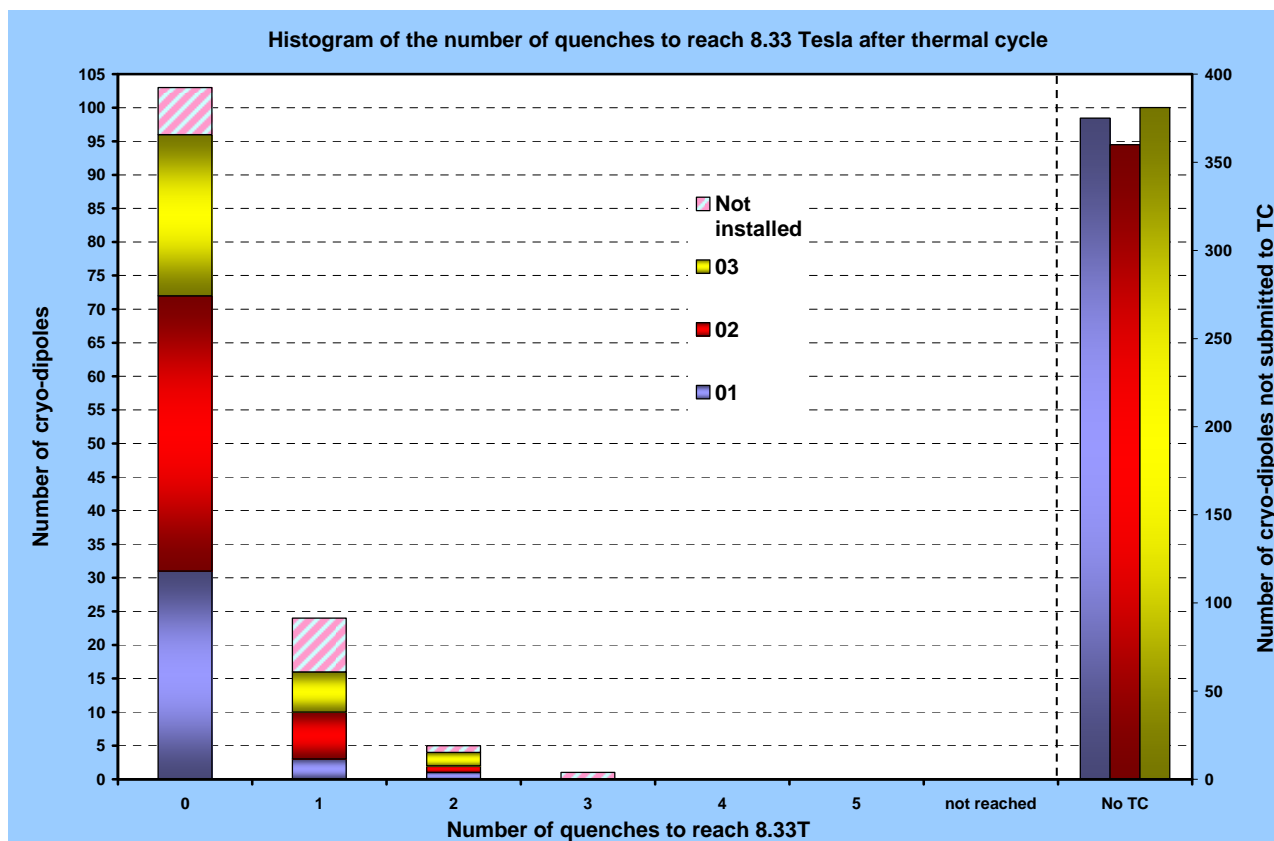


Figure 4.3 _ Cumulative number of magnets as a function of the number of quenches to reach 8.33 T after thermal cycle, for the three producers. Those dipoles not installed in the tunnel are also added to the plot.

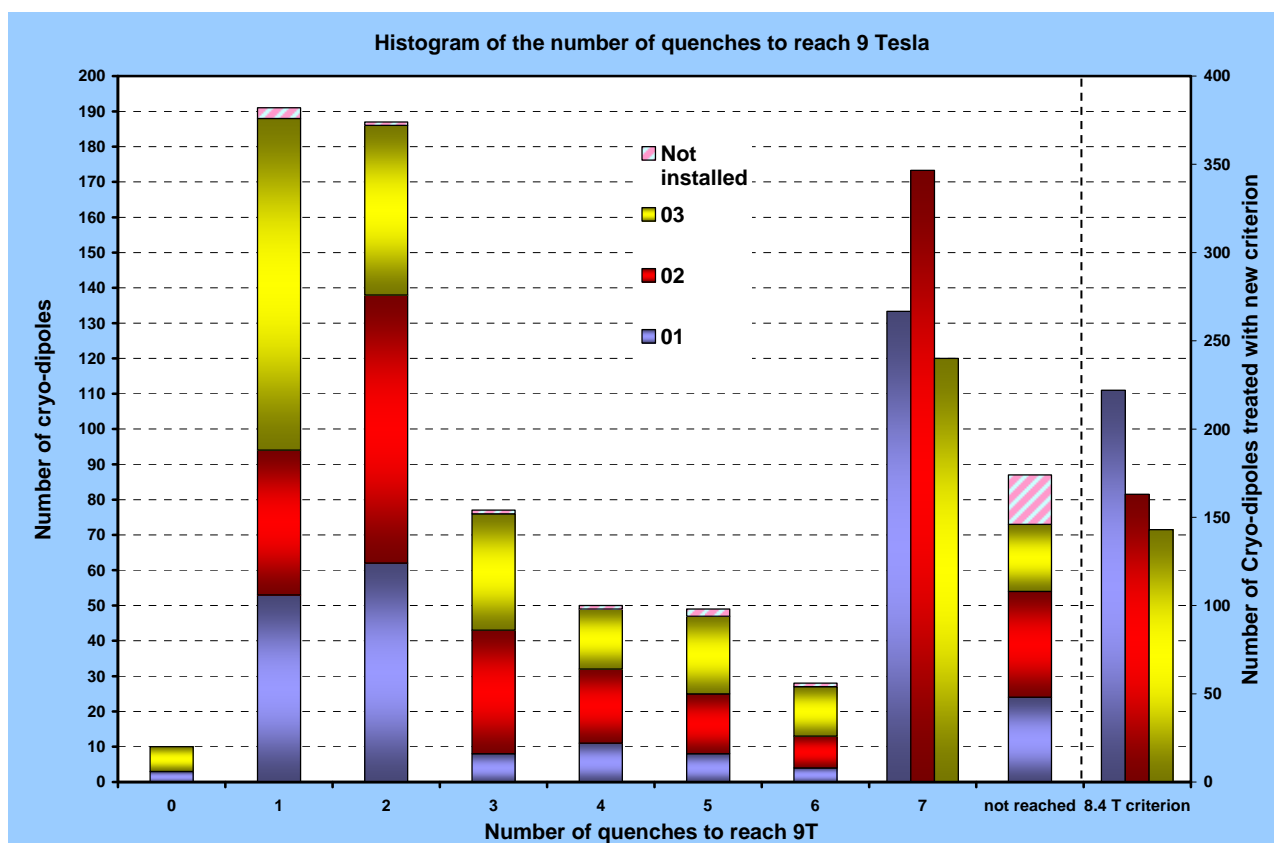


Figure 4.4 _ Cumulative number of magnets as a function of the number of quenches to reach 9 T, for the three producers. Those dipoles not installed in the tunnel are also added to the plot.

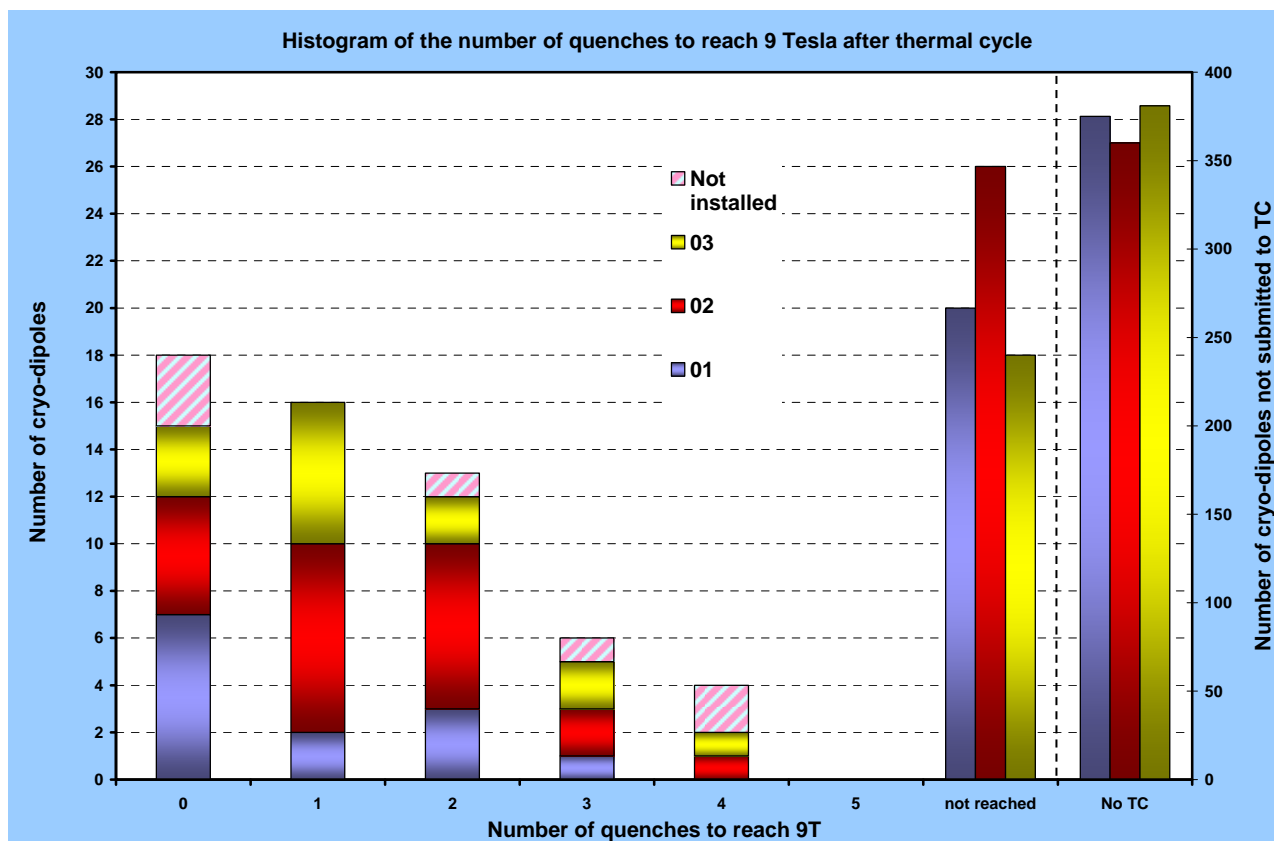


Figure 4.5 _ Cumulative number of magnets as a function of the number of quenches to reach 9 T after thermal cycle, for the three producers. Those dipoles not installed in the tunnel are also added to the plot.

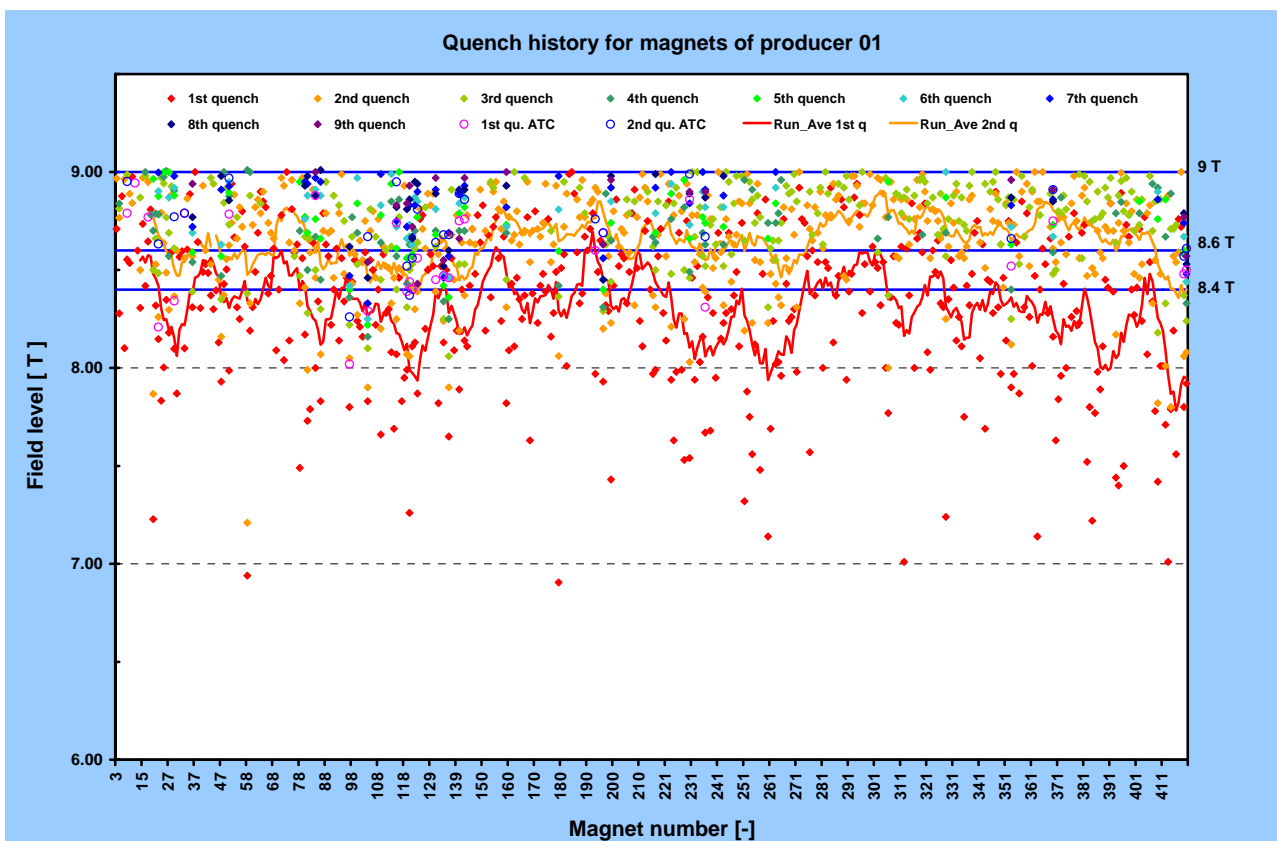


Figure 4.6 _ Quench history for magnets of producer 01: first cool-down quenches (with running average over the last 10 points for 1st and 2nd quenches) and first two quenches after thermal cycle, if any.

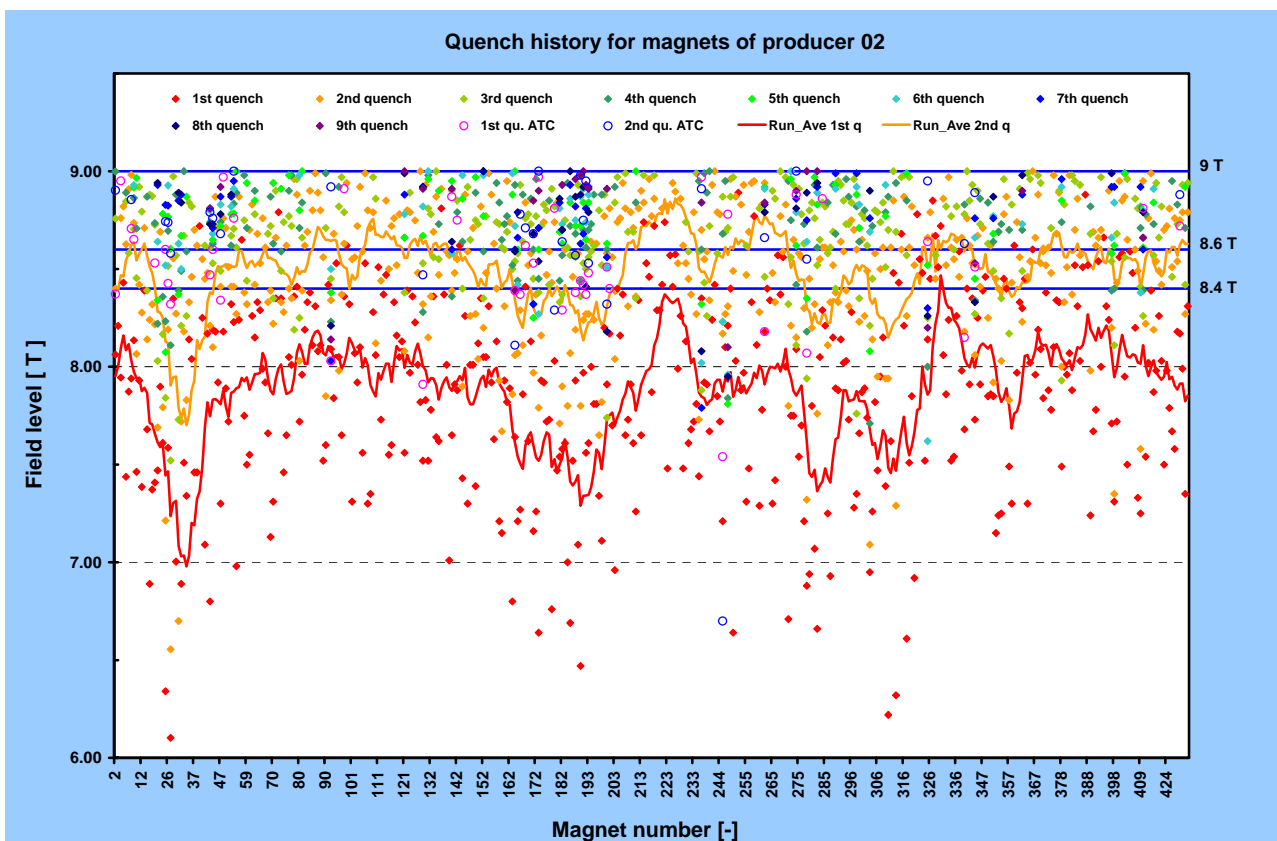


Figure 4.7 _ Quench history for magnets of producer 02: first cool-down quenches (with running average over the last 10 points for 1st and 2nd quenches) and first two quenches after thermal cycle, if any.

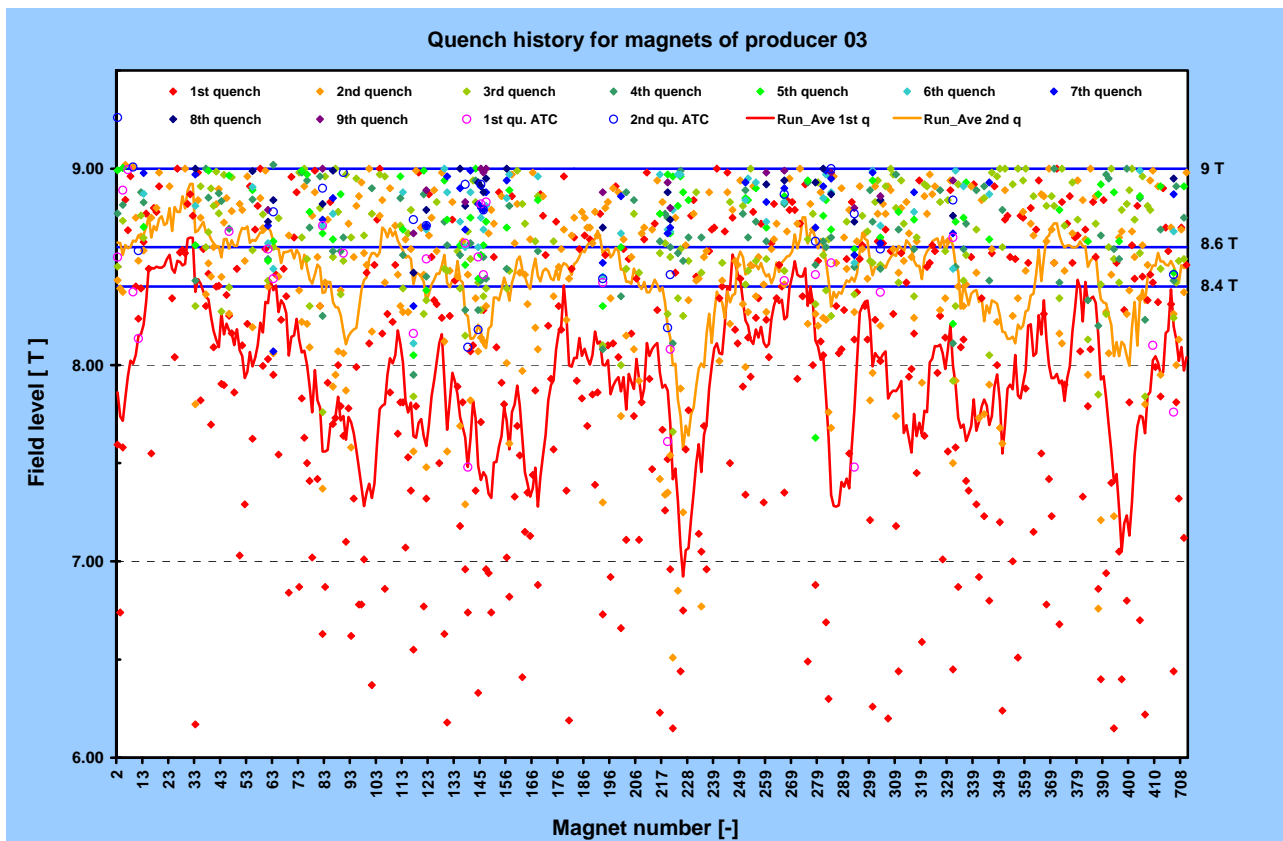


Figure 4.8 _ Quench history for magnets of producer 03: first cool-down quenches (with running average over the last 10 points for 1st and 2nd quenches) and first two quenches after thermal cycle, if any.

BIBLIOGRAPHY

- LHC Project, “*Technical Specification for the Supply of 1158 Cold Masses of the Superconducting Dipole Magnets for the LHC Collider*”, CERN IT-2997/LHC edms no 312601, May 2001.
- Pugnat P., “*Investigation of the Electrical Insulation Problems developed in the Quench Heater Circuits of the LHC Pre-series Cryo-Dipole HCLBBR_000-CR002002*”, Internal Note CERN-LHC-MTA-IN-2002-186.
- Tommasini D., <http://lhc-dipcoor.web.cern.ch/LHC-dipcoor/status.html>.
- Todesco E., Beauquis J., Bellesia B., Bevillard G., Gubello G., Pauletta S., Scandale W., Vollinger C., Wildner E., “*Controlling Field Quality in Magnet Production*”, LHC Performance workshop, Chamonix XII, CERN-AB 2003-008 ADM (2003) 104-10.
- Ferracin P., Pagano O., Redaelli S., Scandale W., Todesco E., “*Control of field quality for the production of the main LHC dipoles*”, CERN LHC Project Report 467 (2001).
- Bordry F., Bozzini D., Dahlerup-Petersen K., Denz R., Puccio B., Rijllart A., Rodriguez-Mateos F., Saban R., Schmidt R., Serio L., Thiesen H., “*First powering of the LHC Test String 2*”, IEEE Trans. On Applied Superconductivity, Vol.12, no.1: 232 – 235 (2002).
- Floch E., Calvi M., Pugnat P., Siemko A., “*Electrical Resistance at Cold of Diode Busbar Connections – First Results Obtained on LHC Main Dipoles and Preliminary Analysis*”, Internal Note CERN-AT-MTM-IN-2003-064.
- Seyvet F., Arnau Izquierdo G., Bertarelli A., Denis O., El-Kallassi P., Fernandez Cano E.D., Fessia P., Ilie S.D., Jeanneret J.B., Letant D., Poncet A., Pugnat P., Savary F., Sgobba S., Siemko A., Todesco E., Tommasini D., Veness R., Vullierme B., Wildner E., “*Long Term Stability of the LHC Superconducting Cryodipoles after Outdoor Storage*”, IEEE Trans. On Applied Superconductivity, Vol.16, no.2: 180 – 183 (2006).
- Bellesia B., Molinari G., Todesco E., “*Room Temperature Magnetic Field Measurements as a Tool to Localize Inter-turns Electrical Short Circuits in the LHC Main Dipole coils*”, CERN-LHC-Project-Report-951 (2006).

CHAPTER 5

THE ANSYS® MODEL

5.1. OBJECTIVES AND DEFINITION OF THE MODEL.

We have seen in the previous chapters which are the mechanisms at the origin of the electro-mechanical instability of the LHC dipole magnets, and of superconducting magnets in general. It was explained how the geometry of the LHC dipole magnets has been iteratively refined, and we pointed out that the final design has taken advantage of an accurate positioning of the cables and a well calibrated applied pre-stress. Although this allowed a reduction of quenches in the straight part of the series magnets with respect to the prototypes, a few magnets still exhibit a lower than expected performance, whose origin is not fully understood. Furthermore, the problem has only been partially solved for the ends, where the majority of quenches originate, with prevalence in the non-connection side end with respect to the connection side end, despite the greater complexity of the latter.

A precise modelling of the LHC dipole cross-section, which takes into account the fine structure of the coils and can give a clear explanation of residual instabilities, had not yet been attempted, due to the great complexity of the problem. The only model of the LHC dipole magnet cross-section, developed at CERN mainly for magnetic analysis, featured a structure by blocks of insulated cables lumped into arc sectors, and friction was neglected (Ferracin [2002]). Enhancing the complexity of the modelization with individual turn segmentation and interaction between matching surfaces is a necessary step towards a better description of reality. This is even more important in the coil ends, where the Lorentz forces tend to stretch the coil axially: the interfaces between insulated cables and G10 end spacers, and the hard bending of the Rutherford-type cables make it rather difficult to provide proper support and mechanically stabilize the coil.

For these reasons, a new model has been developed, relying on the contact capabilities of ANSYS® to represent interfaces between different materials. Differently from the previous model, it was decided to depict individual turn and to implement friction and the non-linear, hysteretic stress-strain behavior of insulated cables. This model describes the LHC dipole coil cross-section in the straight part: it is the simplest section from the geometrical point of view, but it conserves the complexity and all the features of any other part of the magnet. To test the soundness and the feasibility of such model, the coil dimension measurements have been simulated and reproduced, which were performed in industry (prior to collaring) with applied loads up to nearly 100 MPa.

In Figure 5.1, a sketch of a pole cross-section is superimposed to the picture of the mould which was used in industry to measure Young's modulus. This is exactly the configuration we wanted to reproduce: the two coil layers with individual turns, the interlayer spacer in between and the stainless steel mould, which closes and presses onto the pole.

The data of the coil dimension measurements include both increasing and decreasing of the applied pressure, and enable us to validate the algorithm chosen to model the non-linear

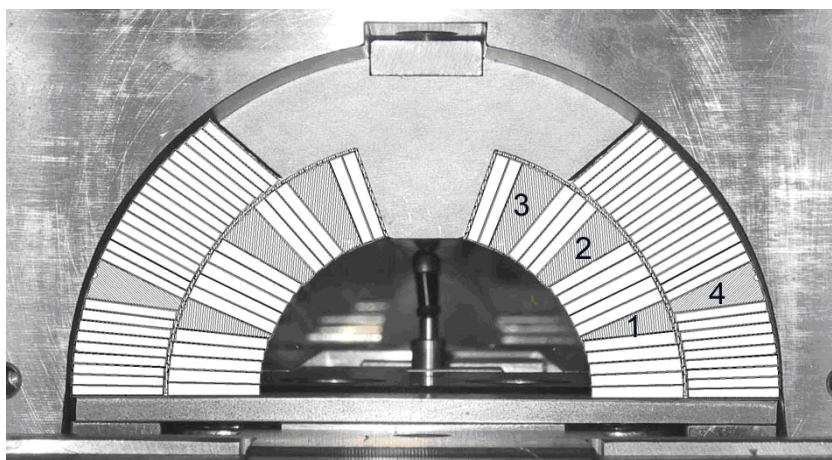


Figure 5.1 _ Schematic representation of a dipole coil during Young's modulus measurements performed in industry.

hysteretic behaviour of the coils, as shown later on in this chapter. This data/simulation comparison constitutes a solid basis for all further developments, even if it is the only witness of coil behaviour: more experimental data, apart from quench results, were in fact not available (and not even easy to obtain, especially in a period where production was at full speed).

After proving the feasibility of the model, and especially its capability of representing contact between different mating surfaces, we tried to reproduce the collaring cycle of the coil: this includes the gradual increase of the collaring pressure from 0 to 160-180 MPa and the following *spring-back* that leaves the coils in a pre-stress condition of around half of the maximum collaring pressure. Once the model was validated by this room temperature comparison, the coil was cooled down from 300 to 1.9 K, which brought it to the proper thermal operating conditions. At this point, a Lorentz force map was applied, to study the response of the structure.

In simple words, what we tried to reproduce was the life cycle of a coil, from which a series of observations on coil stability and mechanical safety conditions could be inferred.

Coming back to the model, it is clear that if we reduce our description to half an aperture (that is a pole) and consider the straight part of the LHC dipole coil, far from the splice region, we can consider as well a vertical symmetry plane, which permits to limit the modeling to one quarter of a dipole aperture (this is no more true if collars and other components were taken into account). Looking in detail at the coil cross-section (Figure 5.2), it is also evident that, by design, there is some interference between few insulated cables and the interlayer spacer; this is the reason why the two layers must be separated in the finite element (FE) model.

This is not a pure geometrical abstraction: even in reality, when the layers are coupled, they don't match perfectly and the first pressure steps just bring them to the design configuration. To be rigorous, it was also decided to build both layers by piling up the cables instead of taking the cable geometrical coordinates from a technical drawing; this was principally done to prevent any accidental interference due to coordinate approximation.

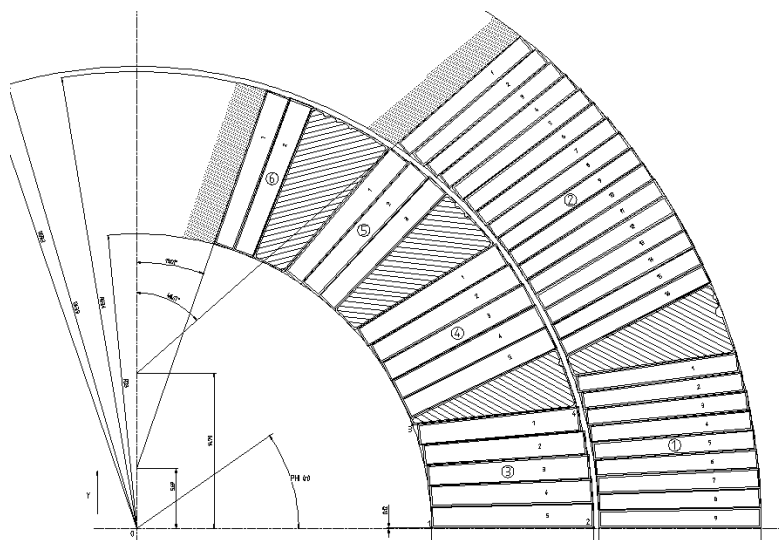


Figure 5.2 _ Conductor distribution within the cross-section of LHC dipole coil straight part.

The cross-section of Figure 5.2 is supposed to provide the nominal coil configuration for both inner and outer layers; according to the LHC Design Report [2004] the cable dimensions were determined for a pressure of 50 MPa applied perpendicular to the broad face of the cables. This means that, under zero stress, the cables have a larger azimuthal dimension and a reduced radial one than those depicted in Figure 5.2. Simulations have been carried out, and will be described in this chapter, to deduce the original, uncompressed dimensions. For what concerns the other components, their dimensions were considered as only slightly affected by pressure.

5.2. ANSYS® CONTACT CAPABILITIES.

5.2.1. Definition of the design and influence of friction.

In practice, any cable (or copper wedge) lays on the cable underneath with a proper reference system whose origin stays on the circumference defined by the nominal winding radius, as represented in Figure 5.3. The Rutherford cables are represented with their keystone angle and sharp corners. The copper wedges have rounded external surfaces. In this way, none of the cables/Cu-wedges have coincident corners (or coincident nodes, if we speak in terms of FE discretization), which means that they cannot be bonded. This leads to the

necessity of defining the contact between any two mating elements via the contact wizard of ANSYS®.

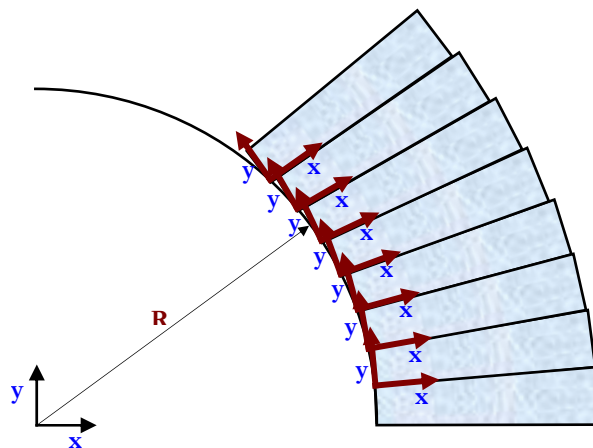


Figure 5.3 _ Example of cable stacking in the model.

Problems involving contact between surfaces are so common in normal life that a univocal dating for the beginning of this kind of studies cannot be fixed. Already in ancient times people had to face with contact and the correlated phenomenon of friction: Figure 5.4-left shows a team of 172 slaves pulling a 60-ton stone statue and one slave is reducing friction by pouring slippery animal fats in front of the sled on which the statue rests; this attempt to overcome friction is nearly 4000 years old!

Even if already Leonardo Da Vinci, during the 15th century, measured the friction force (Figure 5.4-right), it was with Francis Bacon in 1626 that *contact* found a definition as “the state or condition of touching”. It was Euler [1748] who introduced the symbol μ for the friction coefficient, and Coulomb [1785] who developed the well-known law^a

$$F_T = \mu F_N \quad (5.1),$$

linking the transversal and normal forces (see also the remarks on solid friction in Chapter 3).



Figure 5.4 _ Ancient approach to friction: painting from the tomb of Tehuti Hetep at El-Bershed - c.1880 BC - (left) and original sketches from Leonardo da Vinci on friction experiments (right).

^a The general formulation of the “Classical law of friction” also includes another term on the right that account for the so-called cohesion. For simplicity, the reduced form is usually used in most engineering calculations.

The subject of contact mechanics became known to the scientific community after Heinrich Hertz published his classic paper on the contact of elastic solids in 1882. His theory was restricted to frictionless contact surfaces and non-conforming linear elastic solids but it led, nevertheless, to the establishment of the concept of contact mechanics.

Physically, when solid bodies are brought together they will either be in contact at a point, along a line, or over a surface; in complex loading and geometrical configurations, a combination of these three kinds of contact is possible. The initial contact region may change under the application of a load and the contact behaviour is sensitive to various parameters (among them, bodies' material and morphology); these are the main reasons why contact problems are highly non-linear and time consuming.

This is particularly true when friction is taken into account: frictional response can be chaotic, making solution convergence difficult. The sliding movement in the tangential direction of a point of contact will be restricted by frictional forces (tangential shear stress), which in turn depend on the normal component of the forces (normal stresses) exerted at this point. The relationship between the tangential and the normal components of forces has a non-linear behaviour. In a frictional situation, contact conditions are either *stick* (no relative tangential displacement) or *slip* (sliding against resistance in the tangential direction). [Solid friction and stick-slip have been already treated in chapter 3]

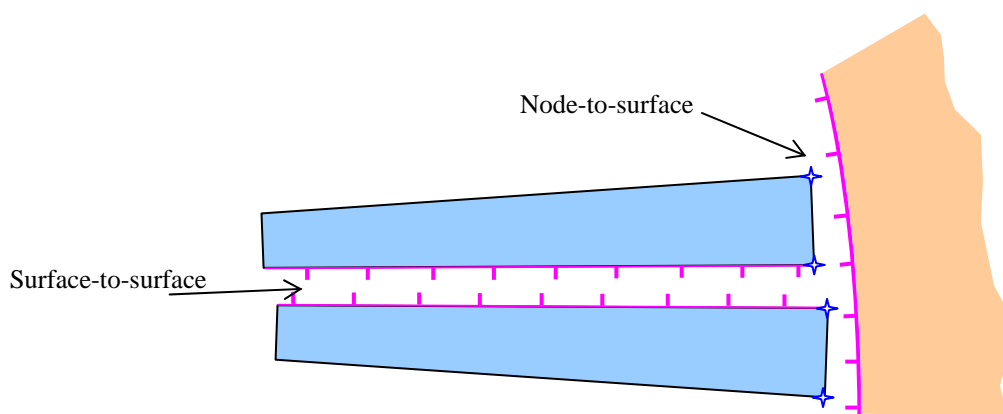
Contact problems are therefore highly non-linear and require significant computer resources to solve. This is even more important for the present application, where the geometry is so irregular and the contact points so numerous that we do not know a priori where the contact is happening. If we speak in terms of contact pairs (that is, the two touching boundaries, which are referred to as the target surface and the contact surface), it is easy to understand the complexity of the 2-D cross-section model where 118 contact pairs have been modelled.

5.2.2. Contact characterization

ANSYS supports three contact models: node-to-node, node-to-surface and surface-to-surface. Because of the choice of leaving any of the components free to move with respect to its neighbours, and the ensuing absence of direct point-to-point link, only the last two types of contacts have been used. Table 5.1 lists selected features of the two types of target-contact pairs under consideration, with their ANSYS names. The most relevant advantage of the node-to-surface contact element is that the exact location of the contacting area is not needed, nor do the contacting components need to have a compatible mesh. This is useful to represent the contact between cable corners and the interlayer spacer or the closing mould. In the other cases, where a planar contact is almost guaranteed, the surface-to-surface contact element is used. An example of such methodology is presented in Figure 5.5.

Table 5.1 _ Contact elements type used in the FE model, with some properties.

	<i>Target</i>	<i>Contact</i>		
<i>Contact element type</i>	Rigid	Flexible		
	Flexible	Flexible		
<i>Surface-to-surface</i>	TARGE169	CONTA171	Large sliding	Both static and transient analyses
<i>Node-to-surface</i>	TARGE169	CONTA175		

**Figure 5.5** _ Example and difference of application of the surface-to-surface and node-to-surface contact elements.

Mathematically, a contact problem requires particular algorithms to be used. In the present case, the augmented Lagrangian method was found to provide a more precise and rapid convergence. For a clear comprehension of the two main types of contact algorithm, we can refer to Man [1994]:

Lagrange multiplier method. It links the degrees of freedom on the two contacting surfaces: if they are in contact, the respective degrees of freedom are related; but if not, they are independent of one another. Extra variables are introduced which represent the normal and tangential forces needed to enforce these displacements constraints. This method is suitable when large displacements are present, so that nodes in the contactor which are not directly opposite a node in the target, at any given stage in the solution, can still be treated. Some indication of whether surfaces are in contact or apart is required. This method has the advantage of accurate surface contact geometry prediction, with nodes sliding considerable distances between the two surfaces without degrading the accuracy or assumptions used. The disadvantages are in deciding when contact occurs, and the fact that the additional degrees of freedom make the system of equations much larger.

Penalty method. In order to model the boundary nonlinearity, penalty methods use element-to-element coupling schemes, in which surfaces are matched topologically to form a potential contact region. This simple coupling scheme is based on gap elements prescribed between two potential contact element pairs. Penetration between two contacting boundaries is introduced and the normal contact force is related to the penetration by an arbitrary penalty factor. The artificially introduced overlap is then removed by an increase in stiffness of the structural matrix and by suitable adjustment in the loading vector with residual loads. The Young's modulus for the gap elements is arbitrarily specified by a user-defined penalty factor. In practice, this technique leads to artificially high structural stiffness, and the presence of stiffness in the gap can markedly affect the results. Furthermore, it does not work for large tangential displacements occurring between contact elements.

In practice, the penalty method uses a contact “spring” to establish a relationship between the two contact surfaces: as soon as the two surfaces of a pair enter in contact, an elastic force is exerted between them, which tends to take the two apart.

The augmented Lagrangian method is based on an iterative series of penalty methods: pressure and frictional stresses are augmented during equilibrium iterations. The spring stiffness is called the contact stiffness (FKN), while the maximum penetration permitted is kept smaller than the allowable tolerance ($FTOLN$).

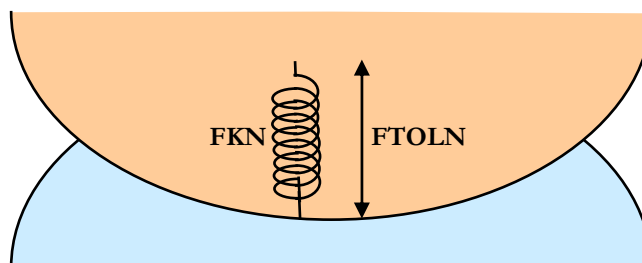


Figure 5.6 _ The elastic interaction of two contacting surfaces.

The amount of penetration between contact and target surfaces depends on the normal stiffness. Higher stiffness values decrease the amount of penetration, but can increase the complexity of the global stiffness matrix and lead to convergence difficulties. Lower stiffness values can lead to a certain amount of penetration and produce an inaccurate solution. Ideally, we want a stiffness that is high enough to limit the penetration and low enough to ensure that the problem will well-behave in terms of convergence.

When the relative sliding of the two surfaces is also taken into account and a non-zero friction coefficient is considered, the complexity increases. ANSYS automatically defines a default tangential contact stiffness that is proportional to the friction, μ , and the normal

stiffness, FKN . In particular, it updates the tangential contact stiffness based on current contact normal pressure and maximum allowable elastic slip, $SLTO$:

$$FKT = \frac{\mu \cdot \text{Pressure}}{SLTO} \quad (5.2)$$

For an exhaustive and rigorous mathematical treatment of contact algorithm, refer to Wriggers [2002], and to Man [1994] for a treatment of FEM-BEM contact mechanics (finite element vs boundary element modelling).

5.3. MATERIAL PROPERTIES AND MELAS FUNCTION.

5.3.1. Stress-strain characteristics for the superconductor

The main quench origin has to be found in the mechanical instabilities of the coils. It has already been underlined how important the perfect positioning of the cables is, to prevent their relative sliding and the heat generation connected to the frictional slipping regime. The more precisely we know the coil mechanical behaviour during assembly, cooling and energization, the more efficiently we can react to limit its lack of compaction, to reduce cable freedom and diminish the risk of a mechanically-induced quench. We have to ensure that the coils are still under compressive stress after cool-down to liquid helium temperature and energization, but on the other side we cannot block the coils with an excessive pre-stress to prevent damage of the conductor or conductor insulation.

In addition, from a magnetic field quality point of view, a perfect positioning of the cables is fundamental; and it becomes even more important to provide the coils a proper pre-stress, to reduce the change of the compression state that the cables undergo during powering, and limit the intolerable field errors resulting from geometry deformation.

These are the reasons why the mechanical characterization and the measurement of the Young's modulus of all the components, and of the superconducting cables in particular, have been always given a great importance, already in the past (Carson [1985] and Markley [1991]). Due to the composite nature of the NbTi Rutherford-type cables, it is in fact very difficult to predict their stress-strain behaviour and it has to be experimentally determined.

Following the definition of the Encyclopædia Britannica [2005]:

Young's modulus is a measure of the ability of a material to withstand changes in length when under lengthwise tension or compression. Sometimes referred to as the modulus of elasticity, Young's modulus is equal to the longitudinal stress divided by the strain:

$$\text{Young's modulus, } E = \frac{\text{stress}}{\text{strain}} \quad (5.3),$$

with the strain being the linear change in dimension divided by the original length; the units of Young's modulus are therefore N/m^2 .

Measurements of the elastic modulus and of the thermal contraction of the LHC NbTi cables were first reported by Védérine [1999] and Reyrier [2001]: within the framework of development of quadrupole prototypes at CEA/Saclay, they restricted the investigation to the type II cable (that is the one used for the dipole outer layer and for the LHC arc quadrupoles – see Appendix 1). Couturier et al. [2001-2002] analysed at CERN both cable types and the results are in good agreement with those of Védérine. Apart from the particular technical solutions chosen, the experimental setup and procedure used by both teams, were more or less identical: a stack of insulated cables (piled up in an alternate way so as to compensate the cable keystoneing) was cured according to the conventional procedures followed for the dipole poles, and was inserted in a U-shaped mould for mechanical measurements.^b The results obtained by Couturier are presented in Figure 5.7, where the stress values are plotted vs the height of the stack measured.

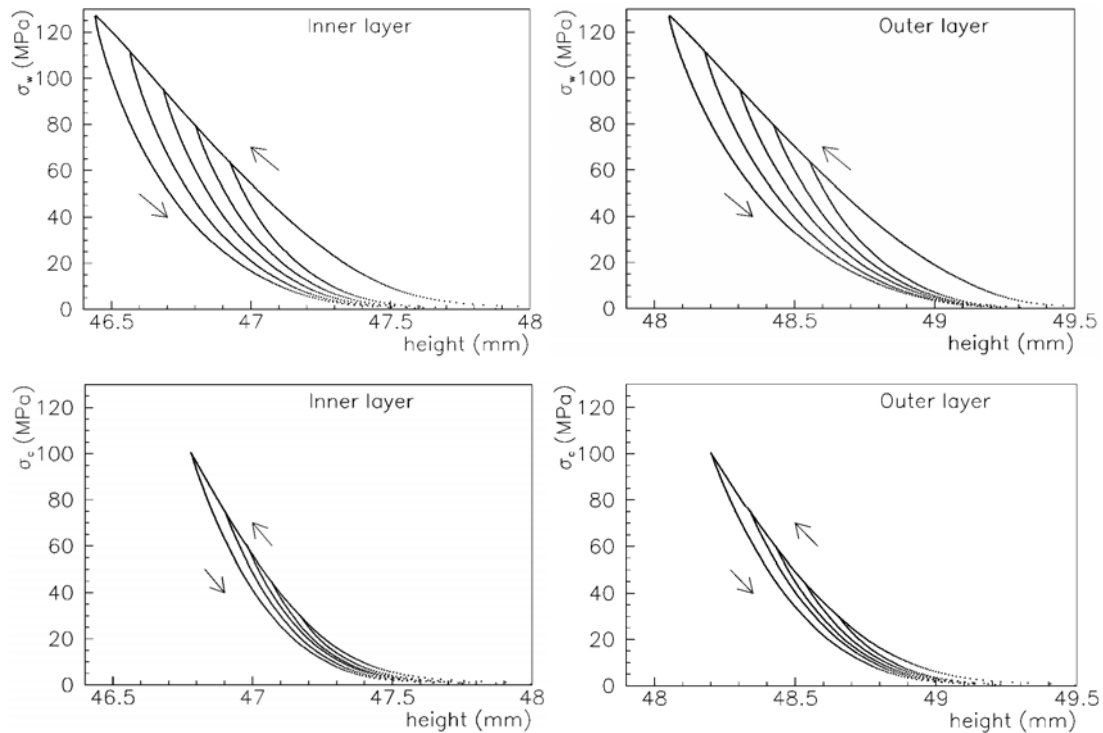


Figure 5.7 _ Stress-displacement characteristics for inner and outer layer cables, measured by Couturier et al. at 300 K and 77 K (on the top and on the bottom, respectively) and with several maximum stress values reached.

^b For what concerns the type and thickness of insulation and the curing cycle parameters refer to chapter 4.

The major features we can recognize from the analysis of the experimental data are the following:

- the stress-strain loading curves are highly non-linear up to around 50% of the maximum applied stress (nearly 60 MPa) and there is a small difference between inner and outer layer cables at room temperature;
- the unloading branches are different from the loading ones (mechanical hysteresis) and the amplitude of this hysteresis depends on the maximum pressure applied during the loading phase;
- the amplitude of the hysteresis diminishes at lower temperature.

As shown in the following, the non-linear and hysteretic behaviour of the Young's modulus was a source of complexities in modelling the superconductor/insulation composite material.

As far as the modelling is concerned and due to the complexity of the cable structure, it is impossible (and probably unnecessarily time consuming) to draw each cable as composed by its sub-elements; this is why they were modelled as quadrilaterals with homogeneous material properties (including insulation). It appears evident how this choice is in perfect agreement with the measurements of the elastic modulus we have just described, in which no concern is given to the hybrid structure of the cable.

Another remark has to be made. The choice of simplifying the measurements by stacking the cables in an alternate way, implies that no difference was made between the thick edge of the cable with respect to the thin one. This leads to neglect the change of ratio between insulation and cable from one side to the other, as well as the higher compaction of the superconducting strands at the thin side. As it was shown with one of the simulations performed, in any case, the resulting error is small compared to other simplifications that are introduced by a finite element modelling (it can also be argued that the two effects, different ratio between components and different compaction, counterbalance one another).

Another issue is whether or not we need to distinguish between the azimuthal and the radial values of Young's modulus. First of all, azimuthal and radial components of the Young's modulus refer to the components that are perpendicular and parallel to the broad face of each cable. According to the procedure followed in performing the measurements on the cable stack, it is evident that only the azimuthal component of the elastic modulus was measured; no information was provided on the difference between the two components or on the value of the Poisson's ratio (i.e., the ratio of transverse to longitudinal strains of a loaded specimen). Goodzeit [2002] indicated that the cables are not isotropic, and that there is a small difference between the elastic moduli in the two directions. (Nevertheless, attempts were done to study the influence of this difference on the simulation results, which proved negligible within the precision of the model^c; this means that the Young's modulus can be considered to a fairly good approximation isotropic.)

^c Measurements on the radial component of the Young's modulus and on the Poisson's ratio had already been planned inside this work activity, but disregarded due to their secondary role on the model results accuracy.

5.3.2. Material non-linearity and hysteresis at room temperature

There are several functions in ANSYS that permit the description of a nonlinear stress-strain material, but only one seemed to have the proper characteristics to represent the piecewise linear elastic properties of the insulated cables: the **Multilinear ELAStic** function (**MELAS**). In practice, a table is provided with a series of stress-strain value pairs, whose incremental ratio locally defines the Young's modulus of the material; the maximum elastic modulus of the material has also to be provided (the **MELAS** function is, in fact, commonly used to represent elongation test results, where the material has a constant Young's modulus in the linear elastic regime, that reduces when further increasing the stress).

Nevertheless, the **MELAS** material behaviour option has some limitations that we had to take into account in modelling the composite superconducting material:

- it describes a conservative (path-independent) response in which unloading follows the same stress-strain path as loading; this means that no hysteresis can be represented by this function (as it will be shown in a while, the hysteresis had to be thus artificially introduced);
- it must have elastically isotropic materials associated, while we have just mentioned that our material is orthotropic.

Concerning the second point, despite the isotropy restrictions in the definition of **MELAS** function, it was proven that it can be used to represent materials with different elastic modulus in the orthogonal directions; this can be done by providing different values for the maximum elastic modulus mentioned above. In fact, testing a FE cubic sample, it resulted a relation linking the two maximum elastic moduli with the Poisson's ratios:

$$\frac{E_{x,\max}}{E_{y,\max}} = \frac{\nu_{xy}}{\nu_{yx}} \quad (5.4),$$

where ν_{xy} refers to x vs y strains ratio, and vice versa. It means that these maximum values have a real impact in modifying the reciprocal rigidities of the material. In case the anisotropy was found relevant for the precision of the model, we could have used this artefact for imposing a different Young's modulus in the two directions.

Another trick had to be found to represent the hysteresis of the superconducting material. In fact, even if we can include friction in the **MELAS** parameters, this does not account for the real dissipative phenomena. The solution chosen was to represent loading and unloading branches with different material curves, and to reconstruct the unloading part with a non unique curve, different for any different maximum stress level reached. It was decided to use a single loading and 36 different unloading paths, with a 10 MPa separation (we will see later that, during collaring at 160-180 MPa, there can exist local stress concentration points with a Von Mises stress value up to 360-400 MPa).

Since the stress-strain characteristics had been measured only up to 100-120 MPa, the first important step needed for the hysteresis reconstruction was the extrapolation of the ramp-up data to 400 MPa; if we suppose to work always in the elastic regime, we can just linearly extend the straight part of the curves shown in Figure 5.7. To find the unloading curves, it was instead necessary to deduce a scaling law from the few unloading curves we possessed. After several attempts, a coherent and simple common fit for these curves was found in the form:

$$\Delta = (k_1 \cdot P_{\max} + k_2) \cdot P^{(k_3 \cdot P_{\max} + k_4)} - (k_5 \cdot P_{\max} + k_6) \quad (5.5),$$

where Δ is the reduction in stack height as the pressure P is applied, P_{\max} is the maximum applied stress and k_1 - k_6 are constant coefficients. The trend that better represents each curve is a pressure power law, and the shape of the terms $k_n \cdot P_{\max} + k_{n+1}$ was chosen according to the necessity of them being maximum-stress-dependent. Solving the 6-parameters fit by minimizing the squared sum of all the residuals (data minus fit), we got in reality a k_3 value close to zero, which means that the power law exponent is maximum-stress independent. The values of all the coefficients for the inner and outer layer cables and for both room and liquid nitrogen temperatures are summarized in Table 5.2.

Table 5.2 _ Values of the fit parameters for unloading curves (room temperature).

		k_1	k_2	k_3	k_4	k_5	k_6
Room T fit parameters	Inner cable	0.255 e-2	0.42	-	0.188	0.8 e-3	-0.974
	Outer cable	0.289 e-1	2.14	-	0.497 e-1	0.306 e-1	1.57
77 K fit parameters	Inner cable	0.293 e-2	1.34	-	0.883 e-1	0.340 e-2	0.923 e-1
	Outer cable	0.248 e-2	2.25	0.3 e-3	0.616 e-1	0.201 e-2	1.58

Figure 5.8 summarizes the procedure followed for a single element:

- the pink curves are the measured stress-displacement characteristics, both for loading and unloading;
- increasing the applied stress above the maximum measured stress value, we linearly extrapolated along the dotted green curve (part 1);
- applying the fit, we reproduced the blue-lined ramp down (part 2) for any maximum stress value;
- in case the pressure was increased again after ramp down, the new loading path would be represented by the unloading branch plus the upper part of the original loading curve, so as to follow path 3.

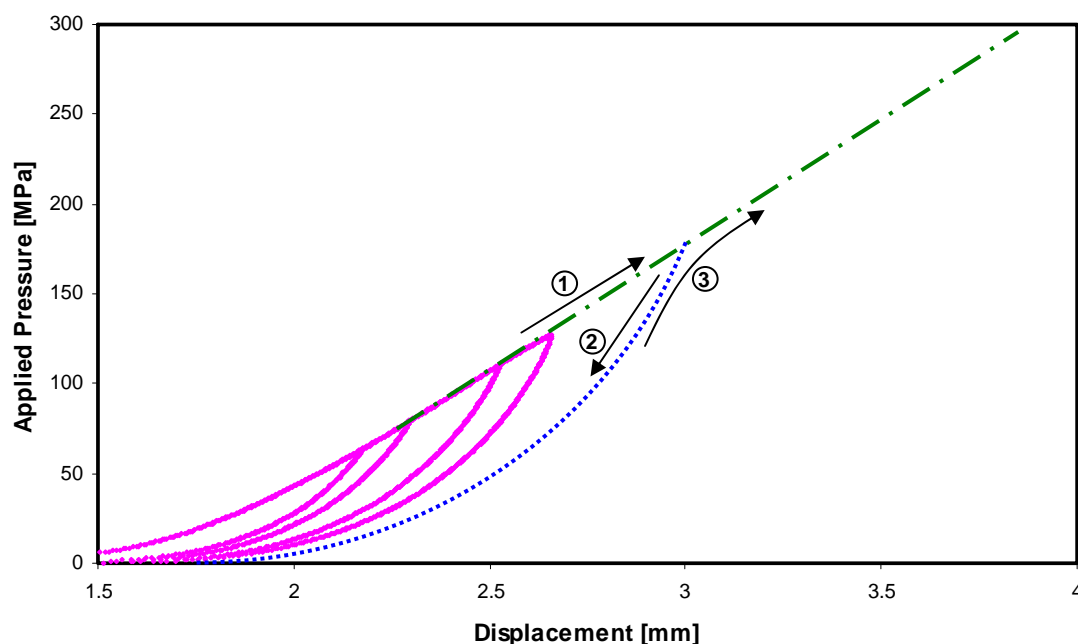


Figure 5.8 _ Pressure cycle for a single element (pink curves are the available measured data).

The change in material properties was done using the function **MPCHG** (change of material number attributes): all the elements with a stress value between x and $x+10$ MPa were selected and the unloading curve corresponding to a peak stress of $x+10$ MPa was attributed to them. This means that any point on the loading curve has to be shifted to the right on the chart, to cross the nearest unloading curve; and due to the fact that the stress distribution has to remain the same, it corresponds to an increase on the x-direction, which is an increase of the geometrical compression for almost every element, with a maximum for the element having lower stress values (far from its corresponding unloading curve). This is at the origin of the necessity of fine-segmenting the unloading part.

In Figures 5.9÷5.11, the use of the **MPCHG** function is illustrated, as applied to a cable with high stress gradient: after loading the structure with an external applied pressure of 100 MPa, different stress values can be observed along the cable width (stress values higher than the load applied can also be created in limited space regions – Figure 5.9); four decades in stress amplitude give rise to an equivalent number of material categories in the cable, as shown with different colors in Figure 5.10. The resulting Von Mises stress distribution does not move far away from the original figure, and also the extreme stress values are only slightly changed (compare Figure 5.11 with Figure 5.9).

This procedure was applied to both inner and outer layer cables and the final mix of materials for the whole section is the one illustrated in Figure 5.13.

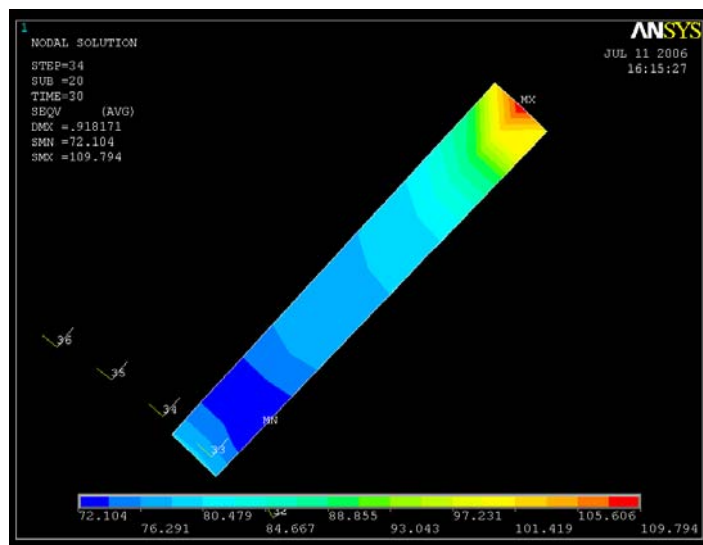


Figure 5.9 _ Von Mises stress distribution for the nodes of a cable of the inner layer, with an external applied pressure of 100 MPa. As shown on the scale below, stress values go from 72 MPa (dark blue zones) up to 110 MPa (red parts).

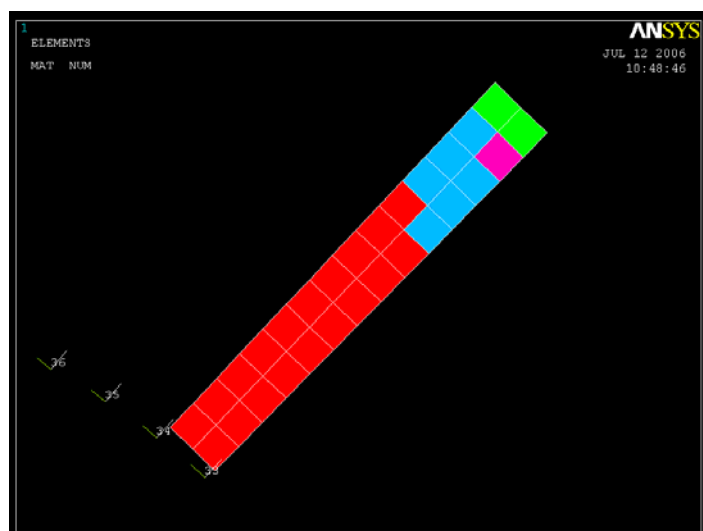


Figure 5.10 _ After applying the MPCHG function, the previously homogeneous cable transforms into a composite structure, where different materials correspond to different stress conditions (in this case 4 new materials have been introduced).

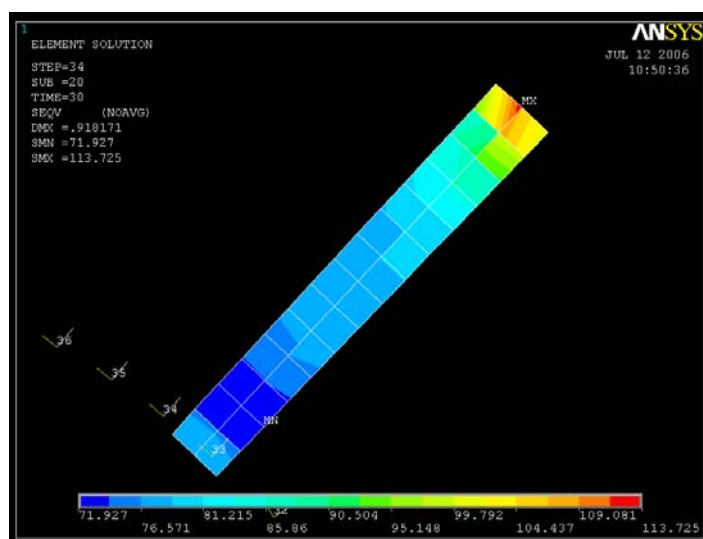


Figure 5.11 _ The resulting Von Mises stress distribution, after applying the material change, is only slightly modified.

5.4. FROM SIMPLE NUMERICAL MODELS TO COMPLETE STRUCTURE.

It is always preferable to check some properties or investigate a particular function or mechanical detail on simple models instead of the intricate, complete structure. This results in an enormous computing time reduction, especially in a case like the present one, in which even a single simulation run is rather heavy and takes up to several hours. The model itself evolved through prototypal phases, to progressively increase its complexity and understand relevant parameters.

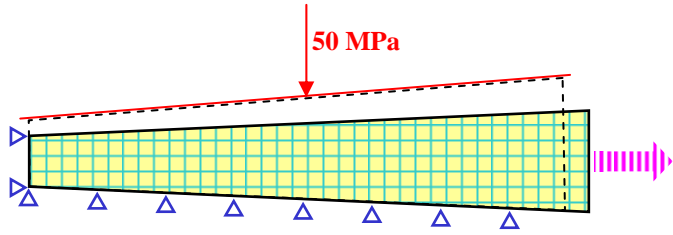
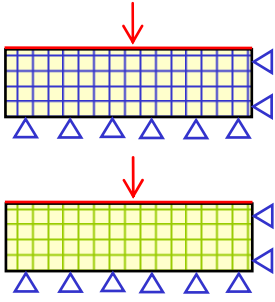
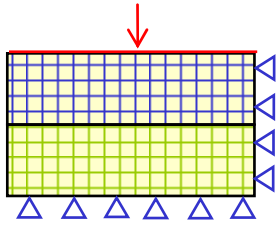
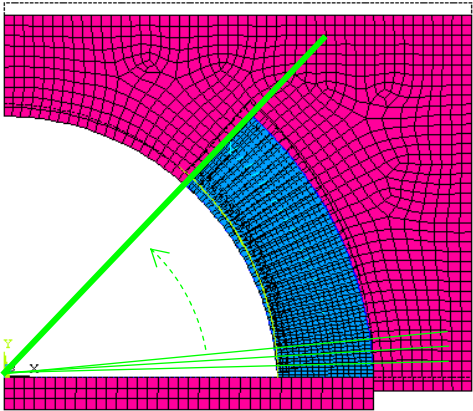
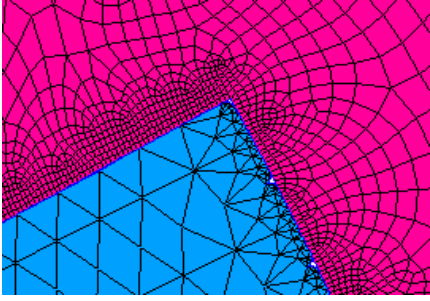
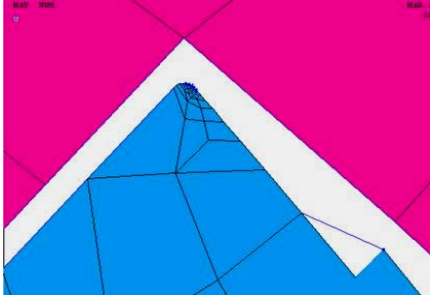
The first important “reduced” model concerns the above mentioned over-dimensioning of the cables. In fact, looking at the cable specifications (LHC Design Report [2004]), it appears that cable dimensions are defined for a nominal applied pressure of 50 MPa: it implies that an unloaded structure should be built with cables with greater dimensions. By means of a model composed by only one cable, as exemplified in row *a* of Table 5.4, these original “unloaded” dimensions could be deduced, by applying to the broad face a pressure of 50 MPa and constraining the other two orthogonal faces. It is evident that, from the choice we did, there is only one direction where the material can “flow”, as indicated by the pink arrow: as a result, a thicker and less wide cable must be used in the modelling. The exact values obtained with the simple cable model are summarized in Table 5.3.

Table 5.3 Comparison between loaded and unloaded cable dimensions.

	Inner layer		Outer layer	
	40/50 MPa	zero-load	40/50 MPa	zero-load
Thin edge [mm]	1.973	1.973+0.042	1.62	1.62+0.024
Thick edge [mm]	2.307	2.307+0.052	1.86	1.86+0.028
Width [mm]	15.40	15.40-0.060	15.40	15.40-0.038

The preference to apply the pressure only on the wide face, leaving the small one unconstrained, was again in accordance with the procedure followed during elastic modulus measurements on stacks: in that case, in fact, the pressure is applied on the wide face and the small ones are in contact with the mould but are neither compressed, nor firmly constrained. Furthermore it is presumable (and it was confirmed by simulations) that the influence of the radial compression with respect to the azimuthal one is very small.

Table 5.4 _ Casuistry of some reduced models for special analysis.

a	 <p>The diagram shows a tapered beam with a yellow grid. A red arrow labeled "50 MPa" points down at the top. A dashed line indicates the top edge. Blue triangles along the bottom represent supports. A pink arrow on the right indicates a shear force.</p>	
b	 <p>The diagram shows a rectangular bulk model with a yellow grid. A red arrow points down at the top. Blue triangles along the bottom represent supports.</p> <p>Bulk</p>	 <p>The diagram shows a rectangular multilayer model with a yellow grid. A red arrow points down at the top. Blue triangles along the bottom represent supports.</p> <p>Multilayer</p>
c	 <p>The diagram shows a stress concentration at a fillet. A green line indicates the fillet. A dashed green arrow points to the fillet. A coordinate system (X, Y) is shown at the bottom left.</p>	
d	 <p>The diagram shows a stress concentration at a sharp corner. A blue triangle indicates the corner. A pink grid shows the stress distribution.</p>	 <p>The diagram shows a stress concentration at a sharp corner. A blue triangle indicates the corner. A pink grid shows the stress distribution.</p>

The second case, presented in row *b* of Table 5.4, concerns the study of the **MELAS** function application and the determination and test of the contact parameters. In fact, for the two separate blocks, we first tested the correct definition of the material through the multi-linear function; this was not merely an academic training, but it was done especially to investigate the influence of the different parameters on the final compression state of the samples, when submitted to particular stress conditions. It was the instrument, in particular, to deduce the relationship between Young's modulus and Poisson's ratio that was described above, and to determine the importance of this ratio on the results.

In the *multi-layer* configuration, the two blocks were put in touch and the contact algorithm was studied, both with blocks of the same material and with blocks of different materials. Also in this case, we studied the accuracy of the results as a function of the contact parameters, for different states of compressive conditions, comparing the sum of the displacement on the separate blocks with the displacement on the coupled ones. Due to the simple configuration used, only the normal interactions between the two blocks could be taken into account; this resulted in a sensitivity analysis for the normal penalty stiffness and for the maximum penetration, with limited influence of the friction coefficient and transversal penalty stiffness and slipping factor. As stated in Paragraph 2, a compromise has to be found between reduced penetration and computing time, which led to acceptable values for the normal penalty stiffness and for the penetration tolerance of 0.1 and 0.001 mm, respectively. Later in this paragraph, we will show that these were considered only as reference values, and different values were used for any couple of mating materials.

After having analyzed these simple models and found the right algorithm for contact and material properties, we investigated complex, single-layer structures like the one shown in Table 5.4-*c*; this was the first simple model with characteristics similar to a real coil, where a multi-contact analysis had to be faced, including cable-to-cable and cable-to-mould contacts. It was nevertheless simpler than the real case, since the cables (the light blue elements in the figure, while the mould is separated into two pink parts) were considered as slices of a circular sector, built at increasing angles, and the outermost side of each cable laid on the same circumference as the external mould. In practice, any corner contact was prevented.

The indications that emerged from this last simple model were important as a starting point for the complex model to be developed, to get accustomed, in particular, with the management of multiple contacts and with the interdependency of normal and transversal dynamics, related by a friction coefficient. Another important point was fixed: the mesh of the cables was chosen so that the number of elements was equal to the number of strands in each one (28 in the inner layer cable and 36 in the outer layer one). A 2-D plane quadrilateral structural element type was used for the whole model (**PLANE42**).

The simulations, we performed on the above-mentioned structure, concerned the investigation of the compression of the arched packet of pseudo-cables when a force was applied on the upper surface of the mould. Speaking in terms of pressure (if we consider the

mould and the whole structure as having unitary thickness), we need in fact to apply charges in the order of 160/180 MPa to our cables, to represent the same values as the ones reached during collaring of the coils. We were not really capable of reaching such high stress conditions: the convergence was never reached and it appeared then necessary to bring in some further modifications. Mesh mismatching was investigated, together with a smoothing of the corners that could be the origin of stress accumulation and mathematical singularities. In the first column of row **d** of Table 5.4, the trial of mesh refinement and rounding off of the corners is presented. The mesh was found to have practically no influence on the convergence problems, while smoothing the sharp corner of the uppermost cable was proven to be beneficial.

The next refinement concerned the insertion in the ‘slice-structure’ of quadrilaterals (representing the cables) not-matching with the external mould (second column of row **d** in Table 5.4). Following the results from the previous step, only the last cable needed to be depicted with a rounded superior corner to get rid of the singularity at the concavity of the mould.

It was at this point that the element **CONTA175** was found to better represent the interaction between the cable corners and the mould, whilst **CONTA172** was proven to be suitable for all other interfaces.

Several other small models were used and the conception of the complete 2-D cross-section required further refinements, but they are an integral part of the activity of the development of any model and are not worthy of being discussed in too many details. They can give an idea of the complexity of the problem, without really helping in the achievement of its comprehension.

All the progresses we did on small or simplified models were collected and gave rise to the drawing of Figure 5.12. This is the final meshed design we built and it constitutes a milestone of this work, where any subsequent analysis started from.

Looking at Figure 5.12, we can make a few comments:

- It may be noticed that the different layers are separated to prevent geometrical interference. This is the reason why the reference circumferences have different origins.
- The color of the cables in the two layers is different because the material characteristics are different. The copper wedges (in green) are separated in four sectors, following the softening of the copper/insulation composite when moving from outside towards the origin of the circular regions (this has been mentioned in the previous paragraph for the case of the cable and represents the increase of ratio between insulation and copper). Furthermore, all the wedges have unique

properties, different from one another. A summary of most relevant material properties is presented in Table 5.5.

- The cables are over-dimensioned, according to what deduced from the small model described in Table 5.4-a.
- While the number of elements in the cable mesh corresponds to the number of cable strands, the one of the inter-layer spacer has been fixed to four/five elements in thickness, since a coarser mesh was not able to represent the combined pressure exerted by opposite layers.
- The layers are bound by a lower plate, constrained from moving in both directions.
- The pressing mould is constrained from horizontal movements (as if vertical walls inside the real press were preventing its sideward motion), while it is submitted on the upper surface to an increasing pressure.
- Any cable/copper wedge is linked to the below reference plane by very soft springs, connected to both the corners of a same wide side. In fact, if it was not like this, as soon as the contact was established, for example, between the mould and the uppermost outer layer cable, the repulsive force originating among the two would push the unbound cable far away (such convergence problems are common for this kind of applications).

Table 5.5 _ Salient material properties at 300 K (*As explained in the text, the Young's modulus of the superconducting cables is non-linear in the whole range). For Cu-wedge numbering refer to Figure 5.1.

	Ex [GPa]	Ey [GPa]	Shear modulus [GPa]	Poisson Ratio
Inner layer cable	3.1 @ 100MPa*		4.3	0.1
Outer layer cable	4.0 @ 100 MPa*		4.0	0.1
Copper wedge 1	77.6	13-41	15-36	0.34
Copper wedge 2	77.6	30-51	29-41	0.34
Copper wedge 3	77.6	35-53	32-42	0.34
Copper wedge 4	75.1	24-47	25-39	0.34
Inter-layer spacer	10	10	4.3	0.3
Steel mould	190		-	0.3

Figure 5.13 shows the result of the ‘morphing’ of the superconducting elements after changing the material properties for unloading. The uniform materials leave place to a jeopardized structure, even if some omogeneous areas are still present.

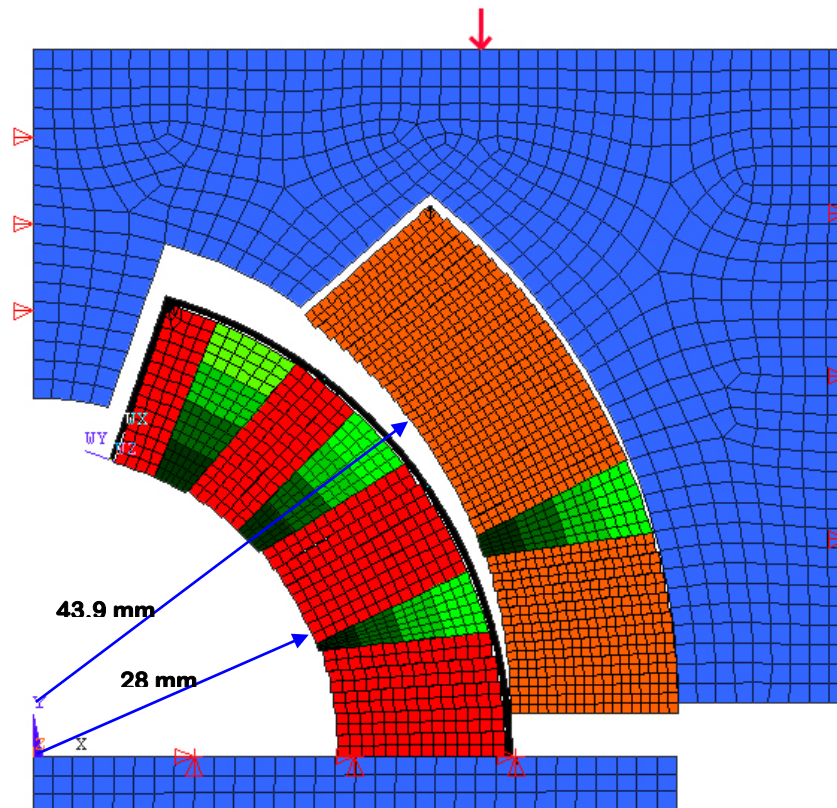


Figure 5.12 _2-D dipole coil cross-section model.

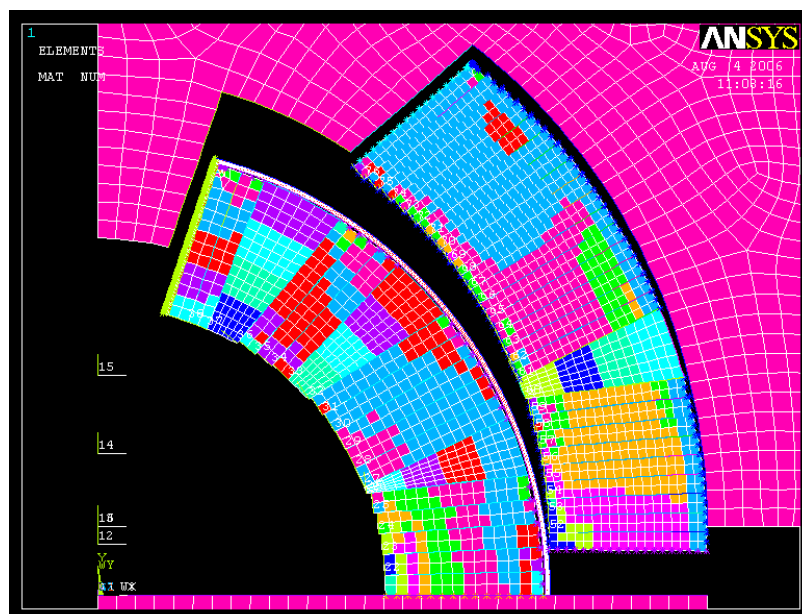


Figure 5.13 _Result of material change for both superconducting layers.

As already explained in paragraph 2, the introduction of friction coefficients enormously increased the complexity of the problem and exponentially augmented the computing time. Once we introduce friction between two elements, the force one exerts on the other is no more simply perpendicular to the contacting surfaces, but a transversal component has to be taken into account, which is proportional to the normal one multiplied by the friction coefficient. In this case, the contact is governed not only by the normal penalty stiffness and the maximum penetration, but also by the transversal penalty stiffness and the maximum slipping factor. We thus have 5 parameters (friction coefficient included) to account for the rough interaction of the two surfaces. 5 parameters that multiply 15 different contact types in our case: it yields a total of 75 values to be optimized so as to properly represent the dynamic behaviour of the coil, finding a good compromise between a faithful representation of reality and mathematical convergence.

To reduce the degrees of freedom, the assumption was made of a minimum penetration; this means that in most of the cases, and whenever possible, the maximum allowable penetration coefficient was fixed to 0.001 mm. In case of a material with high elastic modulus, as in the case of the stainless-steel mould, this value was proven to have a small influence on the interpenetration and was fixed to 0.1 mm, to favour convergence.

All the other values had to be selected by trials and errors, always trying to keep into account the criterion of good accuracy vs convergence-time ratio. A complete list of the numbers used in the model is presented in Table 5.6.

To have a complete view of the complexity of the model, a few figures can be added: a total of 6645 nodes were used in the model, with 118 contact pairs; 15 different contact types were created, each one needing 5 variables to be defined, as mentioned.

Apart from the real constants just described, contact behavior (using surface-to-surface contact elements) is managed through several **KEYOPTs**, options which are used to control the different aspects of the contact algorithm. Three **KEYOPTs** were used in particular in the model after having tested their utility for this specific case: **KEYOPT(9)**, **KEYOPT(12)** and **KEYOPT(10)**.

KEYOPT(9) deals with the initial penetration. This is very important in case involving rigid bodies' motion, which is bound only by the presence of contact: contact between pairs has to be ensured in the initial geometry, so that the contact pairs are "just touching". In this case, once the two bodies enter in contact, the abrupt force exerted by the moving body can result in a breaking-away of the other one (this is the same effect already explained, which is at the basis of fixing by weak springs every free element to the plane). On the other hand, too much initial penetration must be prevented; if this condition is not satisfied, the contact elements may overestimate the contact force, with the same non-convergence result. The choice for this option was thus to keep the default setting, which means that any possible initial penetration is taken into account. Furthermore, 3 mm were selected for the **PINBALL**

term, which means that every target feels its contacting surface even if not directly in contact but within a 3 mm range.

Table 5.6 _ Numerical values for the constants (listed in the same order as in the top left corner) characterizing the contact between any two possible element combinations.

Penalty stiffness Allowable Penetration Transversal Pen. Stiffness Slipping factor Friction coefficient	Inner cable	Inner Cu- wedge	Inter- layer spacer	Mould	Outer cable	Outer Cu- wedge
Inner cable	3 0.001 100 10 0.8	2 0.001 100 10 0.4	6 -0.001 0.001 10 0.4	10 0.001 0.1 0.1 0.4	-	-
Inner Cu-wedge	2 0.001 100 10 0.4	-	2 -0.001 0.01 1 0.35	-	-	-
Last inner cable	3 0.001 100 10 0.8	-	2 -0.001 0.1 0.1 0.2	-	-	-
Inter-layer spacer	6 -0.001 0.001 10 0.4	2 -0.001 0.01 1 0.35	-	6 0.1 0.1 0.01 0.1	1 -0.001 0 1 0.4	2 -0.001 0 1 0.2
Outer cable	-	-	1 -0.001 0 1 0.4	4 -0.001 0.1 1 0.6	4 -0.001 100 100 0.8	2 0.001 10 1 0.4
Outer Cu-wedge	-	-	2 -0.001 0 1 0.2	3 0.1 10 0.1 0.4	2 0.001 10 1 0.4	-
Last outer cable	-	-	1 -0.001 0 1 0.4	10 0.001 0.01 0.1 0.4	4 -0.001 100 100 0.8	-
1 st outer cable	-	-	1 -0.001 0 1 0.4	10 0.001 0.1 0.1 0.4	4 -0.001 100 100 0.8	-

For the different contact surface behaviors, the **KEYOPT(12)** was used, which describes essentially whether the two surfaces are free to move or fixed together. “Bonding” is not allowed, due to the choice of initial separation and the large displacement of the structure. As a consequence **KEYOPT(12)=2** was chosen, which represents no separation contact, in which the target and the contact surfaces are tied (even if sliding is permitted) once contact is established.

For the last option, **KEYOPT(10)=2** was selected. This represents the way in which the contact stiffness is updated. In fact, to improve calculation efficiency, the normal and tangential contact stiffness can be updated during the course of an analysis according, for example, to the current mean stress of the underlying elements and the allowable penetration. To increase model’s ductility, it was chosen to update the contact stiffness at each iteration.

In the same optic of rendering the model more agile, it was decided to increase the loads by linear interpolation or ramping (instead of step changing them), for each substep, from the values of the previous load step to the values of this load step (**KBC, 0**). Other selected options are:

- **solcontrol, on** to use optimized nonlinear solution
- **autots, on**, which specifies the use of both time step prediction and time step bisection
- **antype, 4** to perform a transient analysis, and **nlgeom, 1** to include large deflection effects or large strain effects in the transient analysis.

5.5. RESULTS OF THE SIMULATIONS.

The outcome of the application of the model and the procedure to reproduce the hysteresis of the superconducting material, we have just described, is the reconstruction of the elastic modulus measurements, performed in industry on single layers and on assembled poles. These measurements are detailed in Appendix 1 and were systematically executed in industry to determine the dimension of the cured coils and the shimming needed during the assembly of the cold masses.

In Figures 5.14 and 5.15, the comparison between representative experimental measurements and the simulation results is presented, for both layers. The hysteresis, typical of the insulated cables, is very well represented, especially for the outer layer, where the discrepancy is very small: percentage differences of less than 3% and less than 5% are observed in the worst case for outer and inner layer, respectively. It is important to notice that the material change at maximum pressure is responsible for a small additional compression of the structure, as mentioned before; this is in any case almost negligible in both cases.

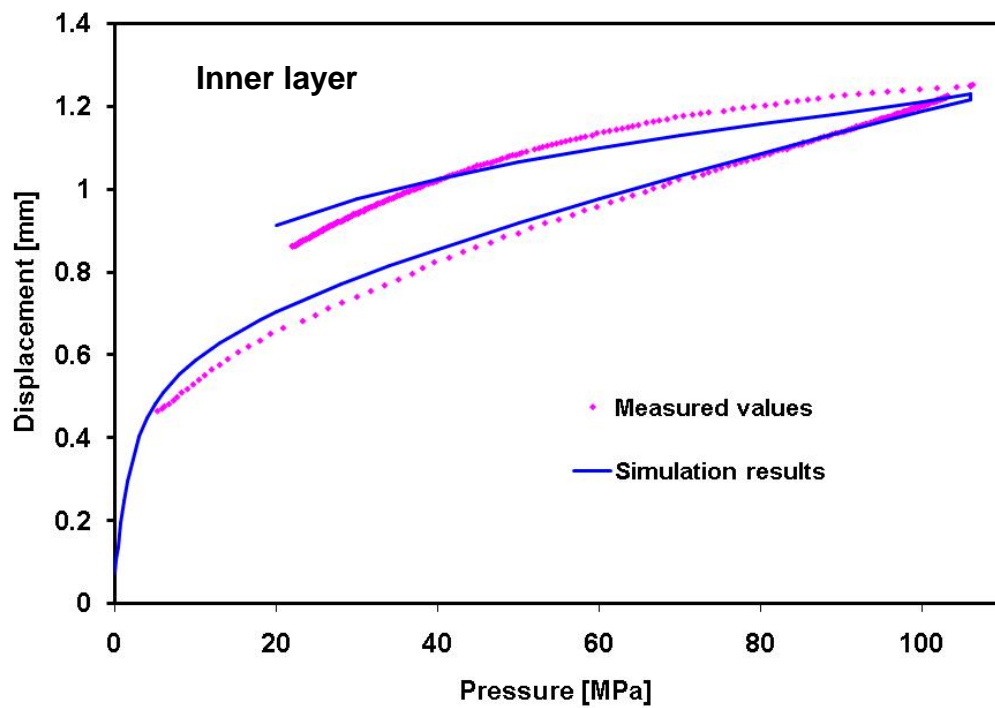


Figure 5.14 _ Loading-unloading cycle for the inner layer. Model results are compared with measured values.

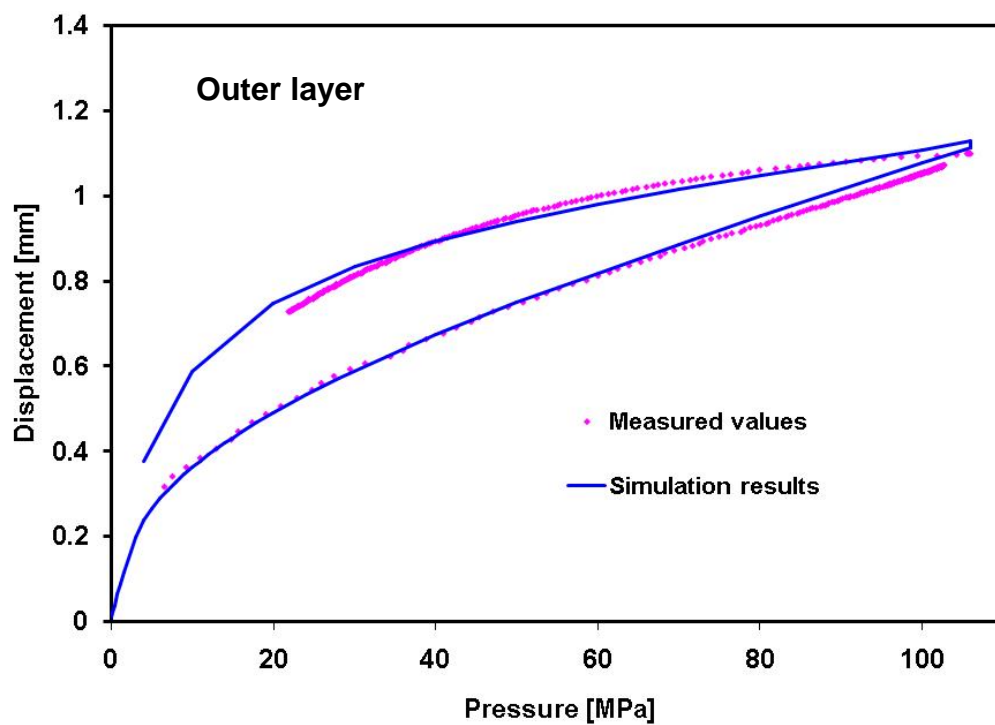


Figure 5.15 _ Loading-unloading cycle for the outer layer. Model results are compared with measured values.

The situation slightly changes looking at the comparison between simulations and measurements on the assembled pole (Figure 5.16): the resemblance of measured and simulated values is not as good as in the case of single layers, but it is nevertheless very satisfactory. The difference between the two series is, in fact, less than 10%, and this is a great improvement in relation with the analytical calculation, which overestimates the Young's modulus of the pole by 50%.

Based on these promising results, it can be argued that the soundness of the model is proven. This can be therefore considered as the starting point for the reproduction of the whole life-cycle of a magnet coil (the following steps being the cooling of the structure and the application of a Lorentz forces map), that is treated in the next chapter.

Link between the two modelling, is the representation of the collaring of the cold mass. The dotted line in Figure 5.16 represents the ideal collaring cycle, which includes a loading up to nearly 140 MPa and the spring-back effect, responsible for the unloading, down to around 70 MPa; this is, as well, treated extensively in the next chapter.

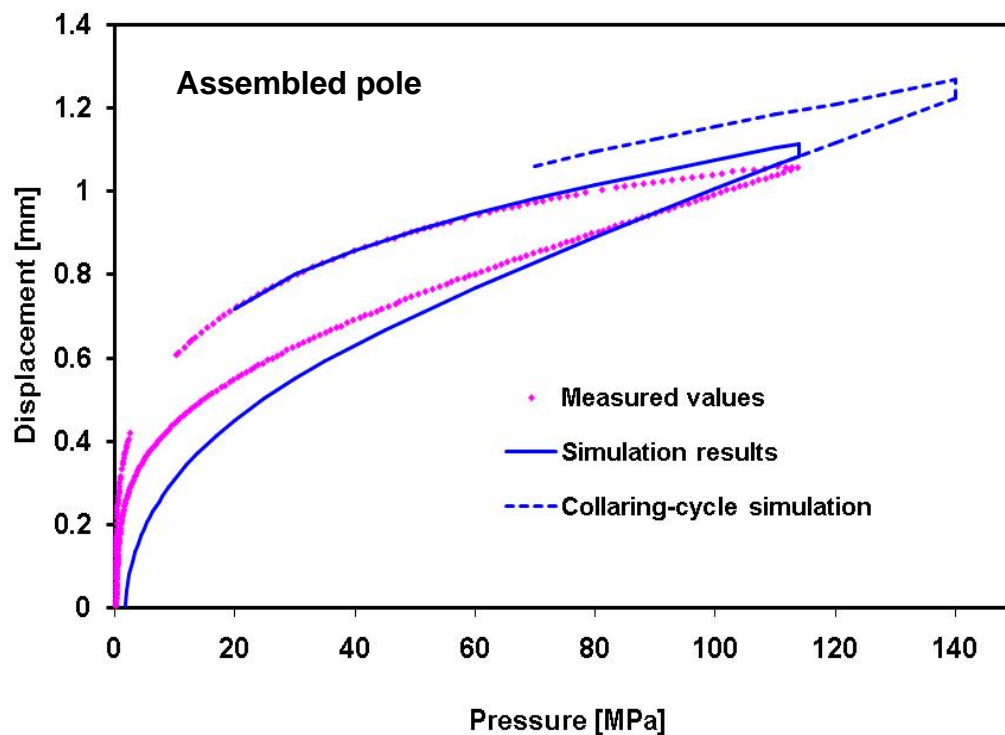


Figure 5.16 _ Hysteretic cycle for the pole. The dotted line represents the ideal collaring, with an increase of the pressure up to 140 MPa and the spring-back.

BIBLIOGRAPHY

- Carson J.A. and Markley F.W., “*Mechanical Properties of Superconducting Coils*”, IEEE Tran. On Magnetics, 21-no2: 706-708 (1985).
- Coulomb C. A., “*The Theory of Simple Machines*”. Mem. Math. Phys. Acad. Sci., 10: 161-331 (1785).
- Couturier K., Ferracin P., Scandale W., Todesco E. and Tommasini D., “*Thermomechanical Properties of the Coil of the Superconducting Magnets for the Large Hadron Collider*”, IEEE Trans. on Applied Superconductivity, vol.12- no2: 1804-1812 (2002).
- Couturier K., Ferracin P., Todesco E., Tommasini D. and Scandale W., “*Elastic Modulus Measurements of the LHC Dipole Superconducting Coil at 300 K and at 77 K*”, AIP Conference Proceedings, vol.613 – no 1: 377-382 (2002).
- Encyclopædia Britannica online, 2005.
- Euler L., “*Sur le Frottement des Corps Solides*”, Mem. Acad. Sci. Berlin, 4 : 122-132 (1748).
- Ferracin P., “*Mechanical and Magnetic Analysis of the Large Hadron Collider Main Dipole*”, Ph.D. thesis, Politec. Torino, Italy, 2002.
- Goodzeit C., private communication.
- Hertz H., “*Über die Berührung Fester Elastischer Körper*”, Journal für die Reine und Angewandte Mathematik, 29: 156-171 (1882).
- “*LHC Design Report - Vol.1 The LHC Main Ring*” (Blue Book). CERN-2004-003. vol.1: 157.
- Man K.W., “*Contact Mechanics Using Boundary Elements*”, Computational Mechanics Publications, Southampton (UK) (1994).
- Markley F.W., Kerby J., Sizemore B., Khoun C. and King T., “*Investigation of the Elastic Modulus of SSC Coils*”, Supercollider 3, J. Nonte, Ed. New York, Plenum. 165-173 (1991).
- Pojer M., Devred A. and Scandale W., “*A Non-Linear Finite Element Model for the LHC Main Dipole Coil Cross-Section*”, IEEE Trans. on Appl. Superconductivity, Volume: 16, Issue: 2, pp.1294- 1297, June 2006.
- Reytier M., Devred A., Durante M., Gourdin C. and Vedrine P., “*Characterization of the Thermo-mechanical Behavior of Insulated Cable Stacks Representative of Accelerator Magnet Coils*”, IEEE Trans. on Applied Superconductivity, vol.11- no1: 3066-3069 (2001).
- Védrine P., Gallet B. and Nouvel C., “*Measurement of Thermo-mechanical Properties of NbTi Windings for Accelerator Magnets*”, IEEE Trans. on Applied Superconductivity, 9-no2: 236-239 (1999).
- Wriggers P., “*Computational Contact Mechanics*”, John Wiley & Sons Ltd, The Atrium, Southern Gate, Chichester, West Sussex PO19 8SQ, England 2002.

CHAPTER 6

POWERING THE LHC DIPOLE

6.1. REPRODUCING THE COLLARING OF THE COILS.

It has been proven, in the course of the previous chapter, that the way chosen to represent the straight section of dipole coils and the model used to describe the non-linear properties of the superconducting materials are appropriate to trustworthily reproduce the elastic modulus measurements. The contacts between mating surfaces have been defined by means of friction coefficients, and the cables featured as individual elements. The hysteretic behaviour of the composite material has also been successfully reproduced through an efficient algorithm, which allows replicating the unloading phase.

It is on this solid basis that, in this chapter, a qualitative model to try to better understand the quench behaviour of the superconducting dipoles is sketched: the collaring of the coils is first simulated, followed by the cool-down of the structure; the powering status of the magnet is finally represented. To this aim, the mould designed in the previous chapter, and representing the machinery used for Young's modulus measurement, has to be replaced by a structure with the shape of an LHC dipole collar. Several simplifications are made, for sake of simplicity and calculation rapidity: the insulating layers are not modelled, because of the complexity of dealing with multiple extended contact surfaces, as well as the iron yoke and the shrinking cylinder are not added, since they are relevant mainly for magnetic field enhancement and confinement. The error we introduce with these simplifications is not easy to estimate, but possibly smaller than the intrinsic error of the simulation.

6.1.1. Collaring the superconducting coils.

When representing the elastic modulus measurements in Chapter 5 (see Figure 5.16), one-quadrant symmetry was exploited. This is no more valid in the case of a complete LHC dipole cross-section; due to the two-in-one structure, in fact, LHC dipole cold masses have a vertical symmetry which corresponds to the vertical mid-plane passing in between the two apertures. The collars have therefore a double symmetry (horizontal and vertical) but only with respect to the centre of the cold mass, as can be seen in Figure 2.3^a. Nevertheless, again for sake of simplicity, it was decided to maintain the one-quadrant description also in this part of the modelling. This represents a simplification which does not diminish the soundness of the analysis performed.

The new model developed from the previous one, replacing the mould by a simplified collar, is shown in Figure 6.1.

^a This is only partially true, since the collars for the straight part of LHC dipoles are normally composed of two non-symmetric components, but the packing of all collars can be nonetheless considered symmetric with respect to the centre of the cold mass.

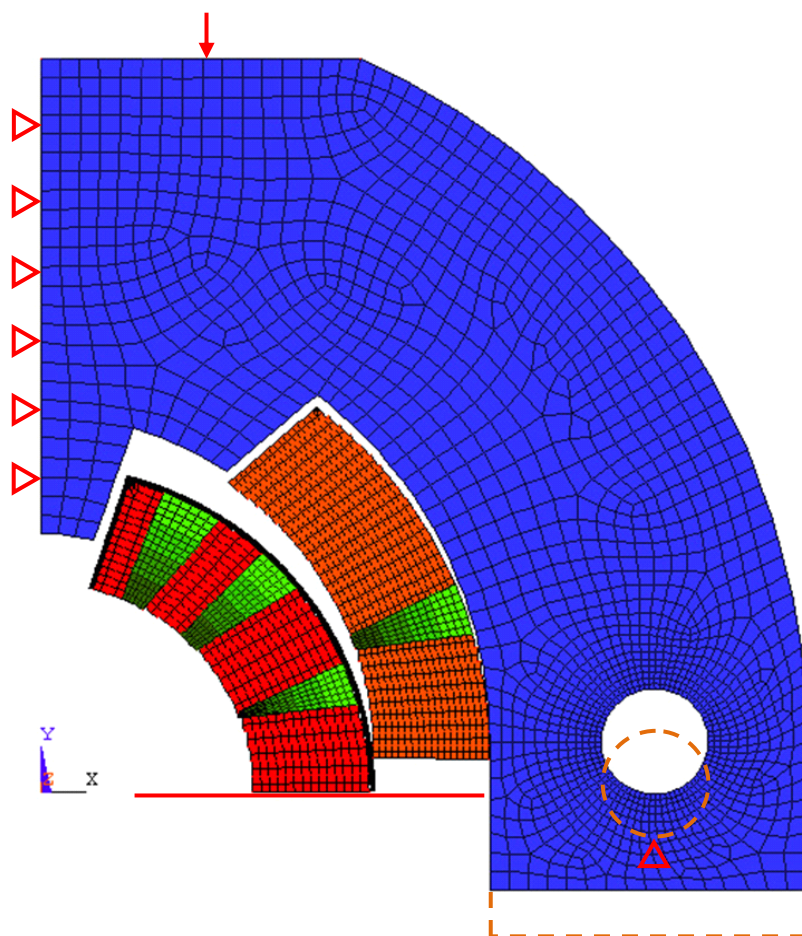


Figure 6.1_ Collared coil model (the dotted lines represent the position of the collar when the bond is applied on the hole).

In this new model, differently from the previous one, the mould featuring the collar is bound only on one side, through the symmetry condition, and the pressure is applied on a smaller surface; the right-hand part of the mould in Figure 6.1 is therefore free to deform along the x-direction, which constitutes a further element of numerical complexity. On the free extremity of the mould, a hole is present, which is used, in real collars, to fix them together through tie rods, once the coils and the collars are assembled and pressed in the collaring press. In the numerical model, before releasing the pressure, the hole has to be bound in the y-direction, representing the action of the rod. This results, when pressure is fully released, in a light ovalization of the coil, as shown in Figure 6.2. The lower extremity of the collar is, in fact, bent toward the center of the coil by some 80-90 μm .

The shape of the two layers in the model of Figure 6.1, and of the inter-layer spacer in between, is of course identical to that of the model defined in the previous chapter; also the material properties for those elements are the same, with the material of the collar identical to that of the previous square mould. As described in detail in Appendix 1, several insulating

layers and protecting sheets are assembled around the coils in a real production. As already mentioned, they are not taken into account in the model, and the inner radius of the collar is adapted consequently. For the protecting sheets, this is not significant, their material being almost the same as for the collars (see details in Appendix 1); substituting the insulating polyimide layers by an equivalent stainless steel layer could, on the contrary, add a further stress on the coils. This effect is anyway homogeneous and should negligibly impact the qualitative result of the simulations. As discussed later, the implementation of the different layers could represent one of the evolutions of the present model.

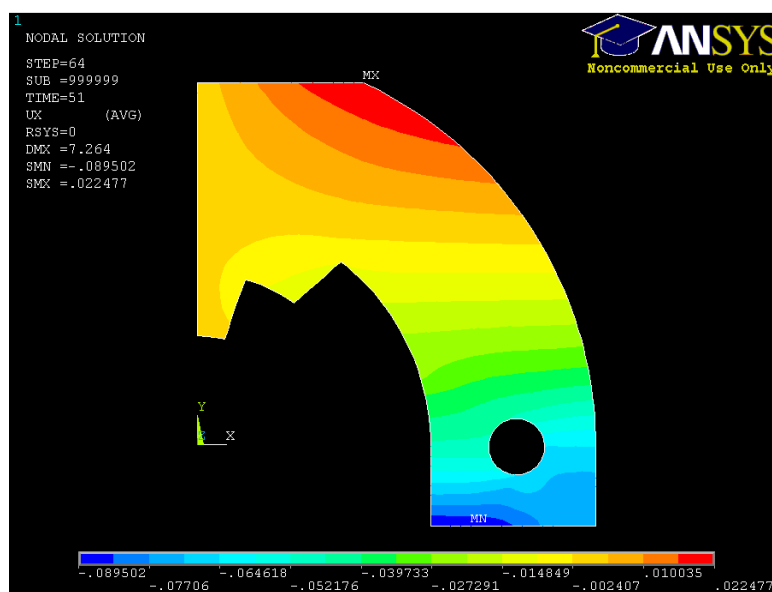


Figure 6.2_ Horizontal deformation of the collar at the end of the collaring process: the lower part exhibits a slight inward displacement.

Before describing the modeling of the collaring phase, it is important to know what is done in industry in the real process. In fact, previous to collaring, the thickness of the mid-plane shims to be added during the assembly of the two halves of each aperture is determined. The objective is indeed to get, after collaring, a residual stress on the coils of nearly 70 MPa. This is the result of several years of study and design, and it's a value which was thought to guarantee a stress status, after cool-down, sufficient to maintain mechanical stability on the coils. To this aim, an algorithm was developed by the three dipole magnet suppliers, based on their experience, to extrapolate the shim values from the elastic modulus measurements of the coils: for every 10 MPa missing, a certain amount of thickness has to be added to the shimming layers.

In the simulated process, a value is estimated, which corresponds to the displacement point where the collar hole has to be fixed (with the bond represented in Figure 6.1) to get a residual stress, after unloading, of 70 MPa. In practice, an increasing pressure is applied to the collars to pack the layers and bring the hole in the position where it ideally superposes to the

corresponding hole of the underneath collar; the collar is further pressed (getting a hole displacement which corresponds to the shim thickness), the bond is put on the hole and the pressure is released to leave the coil free to expand ('spring-back' effect).

After several iterations, a pseudo-shim value of 3.2 mm was found with this routine; it is close to the shim value sometimes found by one of the producers, but much larger than those normally applied in assembling magnets. This means that the poles assembled in industry are normally thicker than the ideal one.

The stress distribution corresponding to the maximum pressure value reached during collaring and the one corresponding to the complete release of the pressure, after rod fixation, are shown in Figure 6.6f and Figure 6.7b and will be analyzed in §4.

6.2. REPRODUCING THE COOL-DOWN OF THE COILS.

6.2.1. Thermal contraction coefficient.

After having reproduced the collaring process, the cool-down of the structure could be simulated. To this aim, a parameter is missing: the thermal contraction coefficient of the composite coil.

The linear coefficient of thermal contraction (α) describes the relative change in length of a material per degree of temperature change. As shown in the following equation, α is given by:

$$\alpha = \frac{\Delta l}{l_i \cdot \Delta T} \quad (6.1),$$

where Δl is the change in length, l_i the total starting length and ΔT the change in temperature.

In the literature, several different values can be found, which differ from one another, according to the way they were obtained. In fact, in the case of a stack of insulated superconducting cables, it is not easy to determine the initial height of the stack; the stress-displacement curve (see Figure 5.7) is, at low pressures, almost flat, and a change of 1 MPa in the compression stress causes a large increase in strain, comparable to, or even larger than the thermal contraction. The way to evaluate the thermal contraction coefficient, used at CERN at the end of 2001 (Ferracin [2002]), was based on stress loss measurement when the stack of cables is inserted in an infinitely rigid mould of known α ; the result obtained is pressure-dependent, and varies from 6 mm/m (at an applied pressure of 40 MPa) to 9 mm/m (with an applied pressure of 80 MPa).

Vedrine [1999] and Reytier [2000] measured, at CEA, the thermal contraction of ten alternately-stacked, insulated superconducting cables inserted in a stainless steel mould; the

mould was equipped with a force sensor and calibrated at room and at liquid helium temperature with different materials of known contraction coefficients. From the comparison with these materials, several samples with different insulation scheme were tested, with and without resin impregnation, and a value of 4 to 5 mm/m was found in the case of an LHC outer layer cable with the same insulation scheme as the one used for the dipoles.

6.2.2. Evaluating the thermal contraction for the coils.

Since the difference between the values obtained by the two laboratories is big and there is no simple way to opt for one or the other (choosing arbitrarily one of the above values could, in fact, lead to a relevant diversity in the final result), it was decided to model the cooling of a cable stack so as to directly infer the thermal contraction coefficient, using measurement data from Durante [2002]. Modeling the cooling of the stack is also a way to validate the algorithm chosen to reproduce the cool-down of the collared coil.

The setup used for the measurements is represented as a confinement box and a press to apply stress on the cables; this simple model is presented in Figure 6.3.

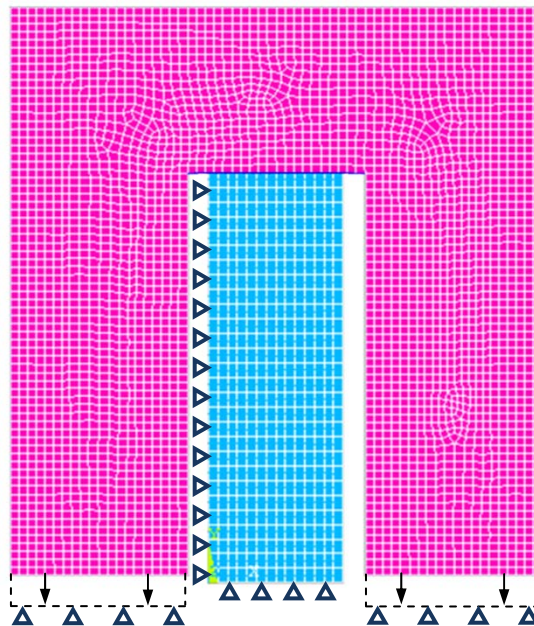


Figure 6.3_ Cable stack model.

Some air gap is present between the cables and the mould to allow the transversal dilation of the material during the application of the mould displacement; the cables are nonetheless horizontally bound on one side, to prevent the relative sliding due to their keystoneing. A vertical bond at the stack bottom replaces the function of cover of the mould.

In Durante [2002], the applied test procedure is based on the so-called *thermal constraint method*: the thermal contraction of a sample, placed in a known mould, is deduced from the variation of the constraint due to the thermal change. In practice, the sample is placed in the mould and pressed up to a stress status of 75.40 MPa and the pressure is kept, blocking the cover with screws. The whole structure is then cooled down to 4.2 K and a stress of 59.91 MPa is measured. An analytical calculation gives the value of thermal contraction of the unknown specimen.

In our model, a progressive stress is applied to the sample, up to the nominal value of 75.40 MPa, by displacing the mould in the compressive direction with bonds on the two bases. This allows using the same bond during the cool-down of the assembly, once the initial stress position has been found. Concerning the cooling part, it was reproduced via an algorithm that enables to gradually change the mechanical properties of the cable. In fact, the colder the sample is, the more rigid the cable becomes (see Figure 5.7). The applied solution consists in making temperature steps of 10 K and attributing, on every temperature plateau, different mechanical properties to the superconducting cable: this is a *discretization of the thermo-mechanical properties* of the cable. The various stress-strain curves were deduced from the elastic modulus measurements performed by Couturier [2002] at room temperature and at 77 K, via a linear interpolation^b.

Referring to Figure 6.4, and looking at a particular element n , the applied algorithm consists in cooling the sample in steps of 10 K. The thermal contraction reduces the stress and the element n moves along the strain-stress characteristic (blue line) established at the initial temperature. The mechanical properties are at this point changed, to adapt to the temperature change: the yellow line (which represents the elastic properties of the material at a temperature 10 K lower than the previous one) is used to describe the increase in rigidity of the material; a simple algebraic calculation is applied to move this new curve along the strain axis according to the stress status reached in the element n . This algorithm is capable of treating every element independently, increasing, nevertheless, the complexity of the calculation.

Applying the described method to the cable stack, and making some attempts with different thermal contraction coefficient, the integrated thermal contraction coefficient which better fits the final value of 59.91 MPa is 0.003 m/m. This does not mean that it is the real value of integrated α , but it is certainly the one which matches, in combination with the algorithm developed, the experimental results. This is therefore the value which will be used in the course of the cooling of the coil model.

^b The variation of the thermal contraction coefficient, as well as the mechanical properties of the cables, is not linear; nevertheless, no data are available in literature and such a simplification is required.

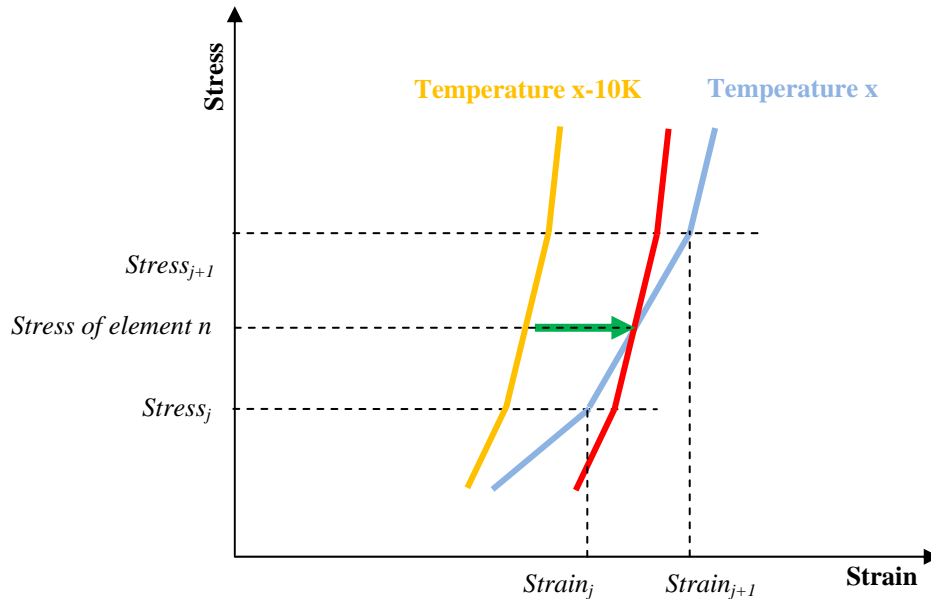


Figure 6.4_ Thermal variation of mechanical properties for element n .

6.2.3. Cooling the magnet.

The evaluated thermal contraction coefficient and the algorithm developed for the simple layer stack could be subsequently applied to the main model, to reproduce, after collaring and spring-back, the thermal behaviour of the coil. Steps of 10 K each were applied to the temperature change and mechanical properties changed on each plateau. Concerning the bonds, those of Figure 6.1 are all kept during the cool-down phase (pressure excluded, since it is removed at the end of the collaring); this means that the structure in figure is constrained on the left side (representing the symmetry condition) and on the bottom of the collar hole (representing the blocking rod), and will therefore move, during the thermal contraction, towards both negative x - and y -directions. This is important to note, since the coil will be compacted not only azimuthally, but also radially.

Two of the phases of cool-down of the coils are presented in Figure 6.7c and Figure 6.7d: the stress distribution in the superconductor is shown in the middle of the process (210 K uniform temperature) and at the end of the cooling (1.9 K).

For a detail description of the resulting stress distribution at the end of the process, refer to §4.

6.3. POWERING THE MAGNET.

The electro-magnetic analysis of a coil with ANSYS not only requires the use of a different type of elements (magnetic and not structural), but also the modelling of the iron structure, which plays, as in most electro-magnetic devices, an important role in enhancing the magnetic field and improves the magnetic field quality, reducing the stray field. To this kind of approach it was preferred a more pragmatic one, based on applying, to the mechanical model, the output of the calculation results from a dedicated software: ROXIE®.

The ROXIE® (Routine for the Optimization of magnet X-sections, Inverse field calculation and coil End design) program package was in fact developed at CERN for the design and optimization of the LHC superconducting magnets, allowing the accurate calculation of the field harmonics and the field distribution within the superconducting coils [Russenchuck, 2005]. It was with this program that the LHC coil design was originally defined and later modified to respond to the requirement of multipoles correction imposed by magnet production deviations.

In Figure 6.5, a typical map of the magnetic induction modulus is presented, computed for a nominal current of 11850 A (corresponding to a central field of 8.33 T). This clearly shows the increase of the magnetic field intensity in the center of the aperture and on the inner border of the first layer; the outer layer, on the contrary, has a minimum of the magnetic field intensity in the mid-plane region.

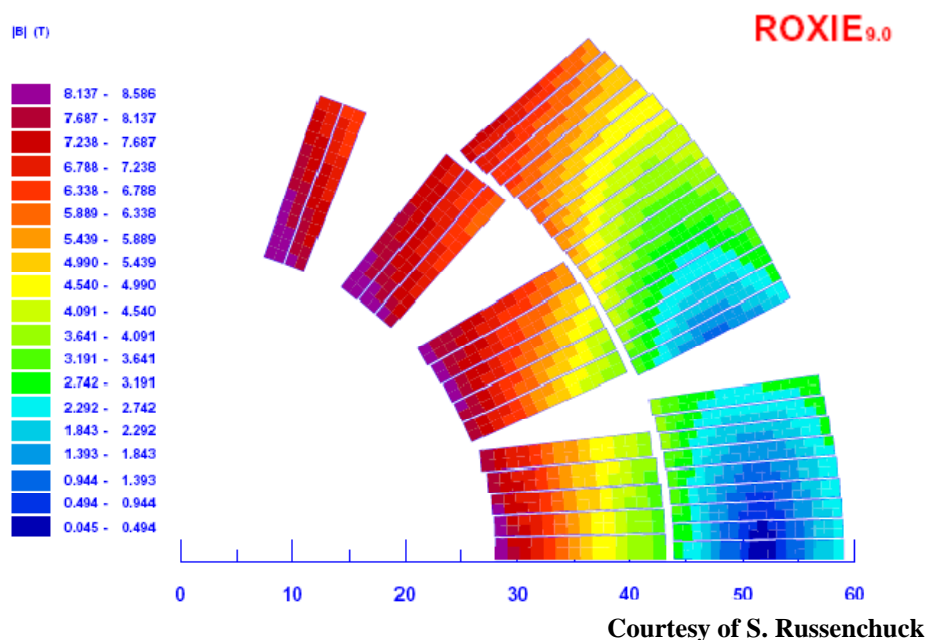


Figure 6.5_ Magnetic induction modulus for the cables of an LHC dipole coil.

Once we know the magnetic field intensity at each strand position, we can easily derive the Lorentz force components, calculated, for each superconducting strand, from the vector product of the current density with the magnetic field. The complete matrix of force components could then be transferred to the ANSYS model and applied in ten progressive steps, corresponding to excitation currents of 1200 A, 2400 A...11850 A.

Figure 6.7e and Figure 6.7f present the result of this run, with the plot of the equivalent stress in the coil for an applied current of 50% of the nominal value and for the full excitation of the coil. Once again, the analysis of the results is given in §4.

6.4. ANALYSIS OF THE SIMULATIONS.

Snapshots from the simulation process are displayed in Figure 6.6 and Figure 6.7, from which some interesting observations can be inferred. The figures have a chronological order, with the representation of the collaring phase and the loading of the structure up to 140 MPa (Figure 6.6 *a-f*), the spring-back effect (with an average residual stress at the bottom of the coil of nearly 70 MPa, Figure 6.7 *a-b*), the cooling of the structure (Figure 6.7 *c-d*) and the powering of the coils (Figure 6.7 *e-f*).

In Figure 6.6*a* and *b* the first steps of closure of the mould are represented, with the compaction of the two layers and the inter-layer spacer in between; in the second image, the equivalent pressure applied on the coil is 5 MPa and some stress starts to appear on the coil.

In Figure 6.6*c, d, e* and *f*, a pressure of 25, 60, 100 and 140 MPa, is progressively applied. The outer layer is piling-up more stress than the inner one, with a progressive accumulation of stress in particular on the first block of the outer layer (nearly 200 MPa are reached locally, with an applied pressure of 140 MPa). Stress gradients of the order of 120-130 MPa are also appearing on some cables of the inner layer, which are preserved throughout the simulation process.

From this point, the bond is applied to the collar hole and the unloading phase of the structure is initiated. The properties of the superconducting cables are changed from the loading to the unloading branches and the hysteresis of the material is reproduced. Figure 6.7*a* and *b* are showing two phases of this unloading process, with the second one representing the final step when the external pressure is removed; the coil holds its stress under the effect of the bond on the collar. This is as well shown in Figures 6.8 and 6.9, where the average stress during the entire life-cycle is described, as an example, for the mid-plane cable and the polar cable (uppermost cables of each layer) for both inner and outer layers: a residual stress between 50 and 70 MPa is observed, with a maximum stress of nearly 150 MPa for the mid-plane cable of the outer layer.

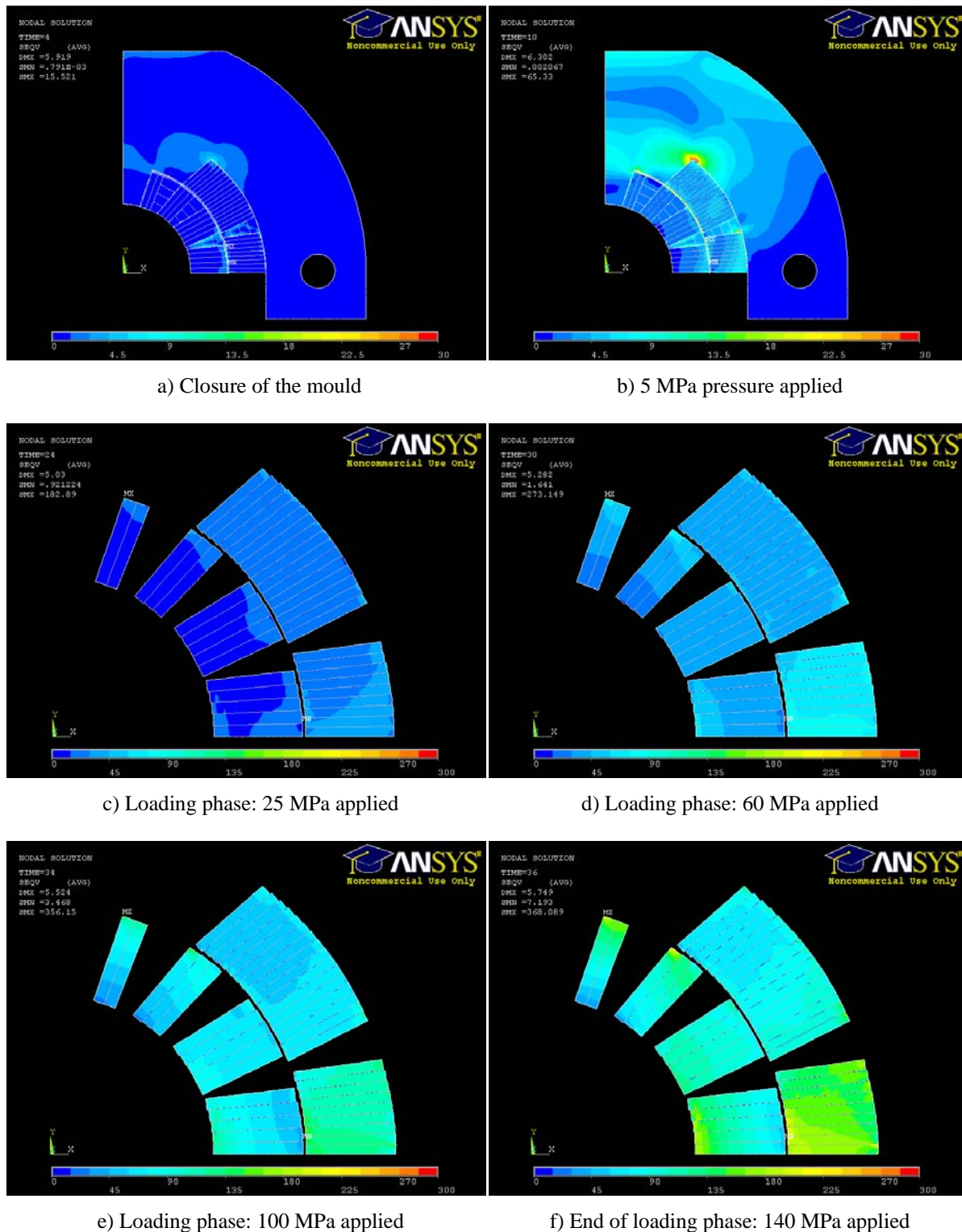


Figure 6.6_ Von Mises stress plots for increasing pressure during the collaring phase.

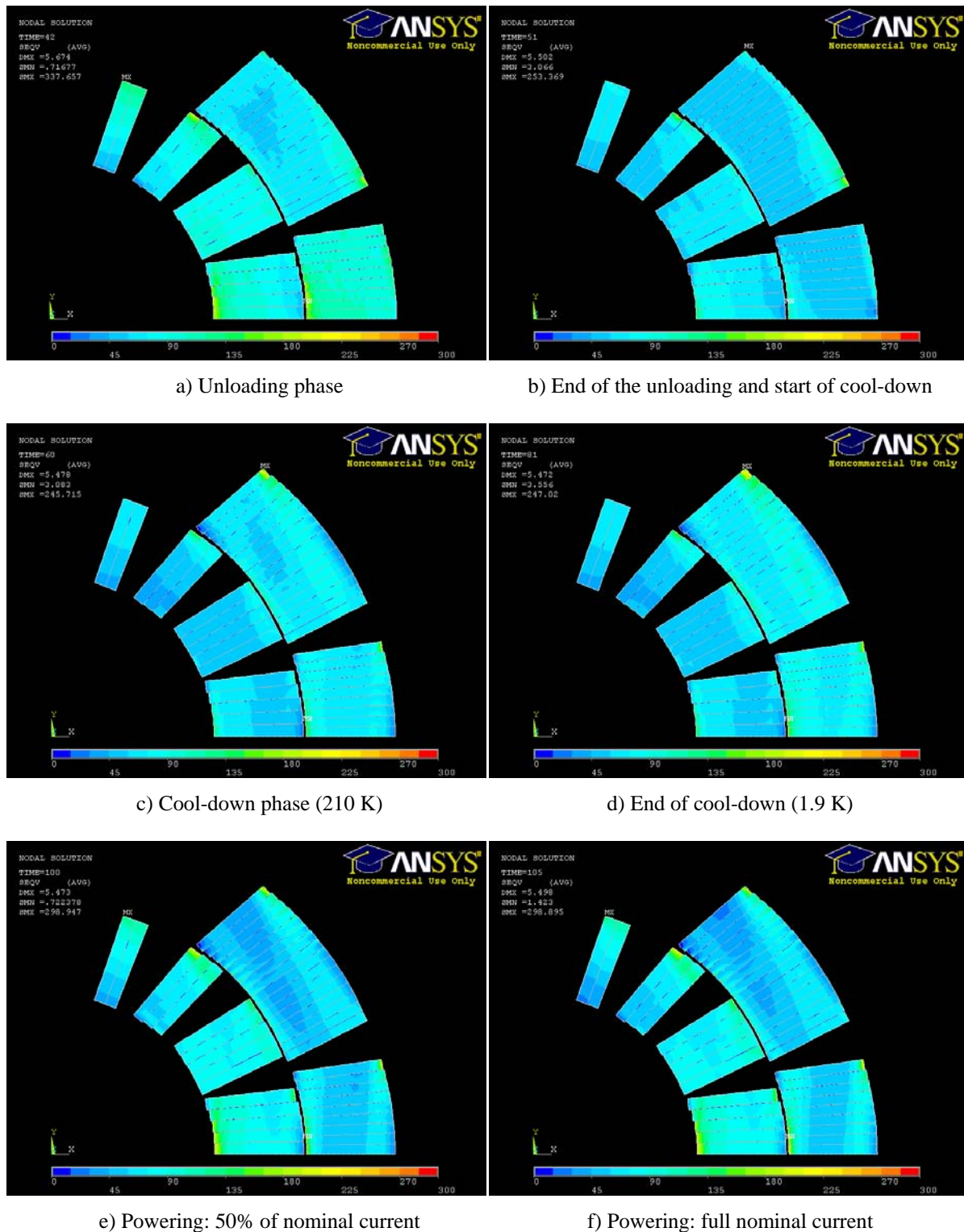


Figure 6.7_ Von Mises stress plots for the unloading (after collaring), cool-down and powering of the superconducting coil.

What is displayed in Figure 6.7*c* and *d* are two moments in the cooling progression: the inner layer loses stress while the outer one gets more constrained due to the effect of the pressurizing collar; the upper corner on the outer layer is the most stressed part. In this case, looking at Figures 6.8 and 6.9, we notice something different for the cables at the extremities of the coils: all of them increase their stress status and, in particular, the cable where the change is more evident is the mid-plane cable in the outer layer, with a delta of nearly 20 MPa. It is important to observe, looking at these two charts, that there is some difference between the stress values at the end of the collaring and the beginning of the cool-down, as well as at the end of the cool-down and the beginning of the powering. This is due to the change of material properties of the cables and, moreover, to the averaging over the whole cable.

In Figure 6.7*e* and *f*, finally, the powering of the coil is shown, at 50% and at 100% of the nominal excitation current. The stress distribution further changes: the outer layer loses part of its stress while the inner one increases under the effect of the Lorentz force. The change of stress status is particularly relevant for the turns of the outer layer, where some areas present almost no stress (mostly evident for the upper part of the second block). The same phenomenon of decrease and loss of stress is occurring for the inner layer. Looking again at the Figures 6.8 and 6.9, we can observe an average reduction of the stress on the polar cables of about 15 MPa, compensated by an almost equivalent increase on the outer layer mid-plane cable (while a smaller increase is detected in the inner one).

Both inner and outer layer cables, which suffer from this loss of stress, are anyway strongly constrained on the external side. This high gradient, that we found in the last cables of the outer layer (from 0 up to nearly 200 MPa) as well as of the inner layer (from 0 up to 130 MPa), is really important to note. In fact, some people have been thinking that a training quench originates from the movement of an entire cable; the conclusion of the simulations seems to suggest the idea that no global cable movement can happen, and the quench origin has possibly to be found in the strand frictional motion. In particular, the uppermost cable of each layer is extremely critical, since these cables are also those subjected to the highest Lorentz forces and those with the lowest stress on the inner side.

The idea that the quench can originate in these two cables, due to the loss of bond of some strands, is strongly supported by the cold test results of SM18 and from the precise localization done with specially developed quench antennas [Calvi, 2006]. At the same time, recent quench studies carried on with the magnets installed in the LHC tunnel, have shown that the linear voltage signal developed after a quench (see, for example, Figure 3.6) sometimes increases by almost a factor 2 or 3: the quench is propagating to the nearby cables. If the quench originates in the last cable of the inner layer, it can only rapidly propagate to a single cable (the copper wedge acts as a quench stopper), while it can propagate to two or more, in case it originates in the external layer. Both locations are therefore source of the motion-induced transition, as emerges from the model.

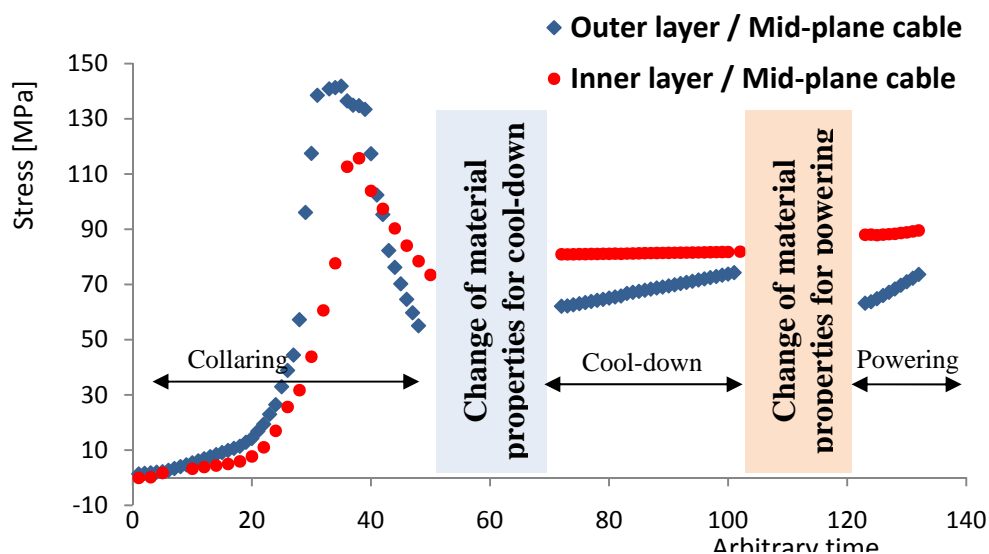


Figure 6.8_ Stress variation for the mid-plane cable of inner and outer layers during collaring, cool-down and powering.

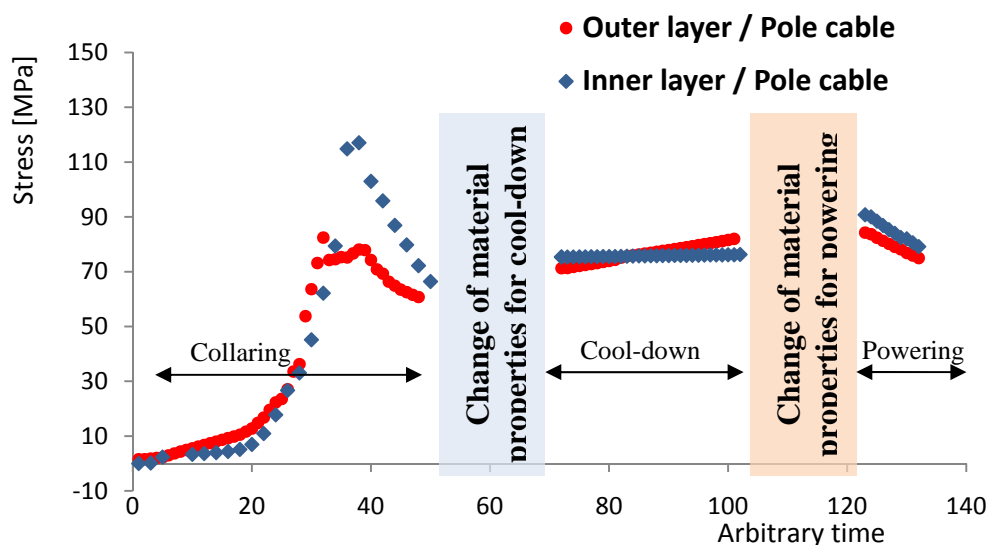


Figure 6.9_ Stress variation for the pole cable (uppermost of the layer) of inner and outer layers during collaring, cool-down and powering.

Looking at the statistics on quench position of Table 4.3, it is evident that a very small percentage of the quenches are localized in the central part of the LHC dipole magnets, while most of them were detected on the extremities, most likely at the transition from the low to the high field region and in presence of the saddle-like-shaped coil. Establishing a correlation, between the real behaviour of these magnets and the (2-D) straight-part-limited model

developed in this thesis, is therefore difficult. The stress loss and the gradient on the uppermost cables are nevertheless incontrovertible, and the results of these simulations could eventually assist in correcting the anomalous behaviour of some magnets belonging to this design. The present model could possibly help in understanding the reason why, regardless of the excellent performance of the LHC-class magnets, some poor behaviour is sometimes observed; and, although big improvements were made from the first prototypes (where quenches were mainly concentrated in the straight part) to the actual design magnets, the quenches still observed in the central part of the LHC magnets could be reduced by, for example, a different shape of the collar that better distributes the stresses and reduces stress gradients. This would require a complex parametric study which goes far away the temporal limit of this thesis. In the meanwhile, a validation of the present model could come from the comparison with the finite element reproduction of the old design and the comparison of their weaknesses (mainly a higher concentration of quenches in the straight part and a worse magnetic field quality); again, this could not be completed in a short time and could become the objective of one of the possible developments of this job. Moreover, another chapter that would deserve in-depth examination concerns the inclusion in the model of the insulating layers between the coil and the collars, plus the addition of the iron yoke, on which basis a full electro-magnetic analysis could be performed.

BIBLIOGRAPHY

Calvi M., *Private Communications*, 2006.

Couturier K., Ferracin P., Todesco E., Tommasini D. and Scandale W., “*Elastic Modulus Measurements of the LHC Dipole Superconducting Coil at 300 K and at 77 K*”, AIP Conference Proceedings, vol.613 – no 1: 377-382 (2002).

Durante M., “*Mesure du rétreint thermique d’empilements droits de conducteurs isolés et d’autres échantillons*”, Note Interne 5-2650N—230000500 CEA (October 2000).

Ferracin P., Todesco E., Tommasini D. and Scandale W., “*Thermal Contraction Measurements of the Superconducting Coil of the Main Magnets for the Large Hadron Collider*”, Proceedings of the Cryogenic Engineering Conference-CEC, Madison, Wisconsin, Vol.47 (a): 372-376 (2002).

Reytier M., Devred A., Durante M., Gourdin C. and Vedrine P., “*Characterization of the thermo-mechanical behavior of insulated cable stacks representative of accelerator magnet coils*”, presented at ASC2000, Virginia Beach (USA), 17-22 September 2000.

Russenchuck S., “*Electromagnetic Design and Mathematical Optimization Methods in Magnet Technology*”, E-Book 2005 - CERN 1211 Geneva 23, Switzerland. ISBN: 92-9083-242-8

Vedrine P., Gallet B. and Nouvel C., “*Measurement of Thermo-Mechanical Properties of NbTi Windings for Accelerator Magnets*”, IEEE Trans. On Applied Superconductivity, Vol.9, no.2: 236 – 239 (1999).

Conclusions

The Large Hadron Collider, under commissioning at CERN, is the largest and most powerful particle accelerator ever built. In its 27 km tunnel, more than two third of the circumference are filled with magnets (to guide and focus the particles); it is therefore obvious that the performance of the accelerator depends critically on the reliable operation of its magnets, most of which are superconducting. The bending (dipole) magnets are requested to work at an operating field of 8.33 T and at a temperature of 1.9 K; they must have optimum field quality and stability, for which the accurate mechanical positioning of the cables plays a very important role. To this concern, the geometry of the LHC dipoles has been iteratively refined and the final design has benefited from a perfect positioning of the cables and a well calibrated applied pre-stress. The robustness of these magnets has already been asserted and their reliability in operation has been, as well, recently proven. Nevertheless, after years of studies and observations, the mechanical stability of the LHC main dipole magnets still raises some issues and the anomalous mechanical behaviour sometimes observed is not yet completely understood.

The ultimate performance of a superconducting magnet is determined by the critical current of the cable from which it is wound. In practice, superconducting magnets are designed so as to be operated at a safe margin below this current limit. However, when a magnet is energized, it can happen that it switches back to the normal, resistive state at a current below the design value. This fast and irreversible phenomenon, referred to as a quench, is of course undesirable and must be prevented.

If we exclude magnets behaviour in operation^a, quenches have two main origins: local degradation of conductor (such as in the splices between magnet coils) and frictional heating resulting from mechanical disturbances (such as conductor motion under the effects of the Lorentz forces). Both quench sources were investigated, with the help of the statistical treatment of quench data (including statistics on number of quenches to reach defined current levels, number of quenches after thermal cycle, position of quenches with relative distribution among straight part and ends) and with quenches performed at a temperature around 4 K. Important information could also be deduced for the operation of the machine, including the temperature margin of the LHC dipoles.

When a superconducting magnet behaves below expectations, it is important to understand the quench origin and to relate this origin to either specific design features or to discrepancies in assembly procedures. Analysis of the quench data and disassembly of magnets, that hardly or never reached their theoretical limit, were instrumental in

^a In operation, energy deposition due to external causes (such as beam losses) is even a more severe cause for magnet quench.

understanding and locating these limitations. In some cases the thorough analysis of collected data gave the explanation to the malfunctioning, finding a confirmation, after inspection of the magnets, of faults in the insulation scheme or of local degradation of quench current. Repairing and avoiding these faults eventually lead to the improvement in magnets fabrication. Also, the survey and comparison of assembly procedures at various magnet manufacturers (creating a unique reference on the procedures followed by the manufacturers for assembling dipole magnet coils up to the so called pre-collaring phase) were used to trace assembly faults.

With the aim of providing an instrument for better explaining the above-mentioned anomalies, a finite element model of the dipole collared coil was developed, which reproduces the magnet life-cycle. To test the soundness of the model, a comparison was done between the elastic modulus measurements on coil (performed in industry) and the finite representation of it, both with single layers and with assembled poles.

The first important novelty of this model, with respect to the previous ones built at CERN, is the subdivision of the structure of the coil into individual turns, instead of considering them embedded in homogeneous blocks. There are, in fact, evidences that even the movement of a single cable can trigger a quench, as the consequence of the solid friction originating between rough surfaces: the stick-slip motion (with the combined effect of local temperature increase and fluxoid motion) is at the basis of the flux jumping phenomenon and the magnet quench transition; even a movement of few micrometers is capable of producing, by friction, a local heating that can generate flux jump and possibly drive the magnet to quench. A modelling of the LHC dipole cross-section which takes into account the fine structure of the coil had not yet been attempted, due to the great complexity of the problem. For this reason, the general approach, followed in developing the model, was to work with simplified test models, to focus on the single problems and then to extend the analysis to the sophisticated structure. The contact capabilities of ANSYS[®], to represent the interface between different materials, were above all investigated, and a set of proper values for the coil model was derived. Also, another innovation in the study is represented by the insertion of friction between all mating surfaces, which was in fact found to play an important role on the mechanical response of the system. More generally, a sensitivity study, to investigate the influence of the contact parameters on the solution result, was performed: a set of values which better reflects the mechanical behaviour of the coil was chosen for the model.

A suitable modelling of the composite magnet coil in agreement with its stress-strain characteristics constitutes one more important element; in fact, the complicated layout of the insulated cable is responsible for a non-linear Young's modulus. While the representation of the non-linear loading path was done with already existing ANSYS material models, the major originality is represented by the fact that the composite cable was modelled with the real hysteresis it shows in practice, with an unloading branch different from the loading one, and not unique, depending on the peak stress value reached upon loading. This means that, increasing the pressure, the whole pole follows the same stress-strain mechanical behaviour.

But when we reduce the applied pressure, any cable has a Young's modulus different from that of the other cables; the higher is the stress reached, the greater the Young's modulus and the smaller the hysteresis. Having at disposal only few experimental curves for the unloading part, measured at random interval, it was necessary to deduce a scaling law from these unloading curves to reconstruct every stress condition. After several attempts, a coherent and simple common fit for these curves was found; an algorithm was finally built to join the two curves, the loading and the unloading one for each cable, to reproduce the observed hysteresis with a good accuracy.

This exercise is completely new in this kind of applications and constitutes an original part of the thesis: no one has ever attempted the description of the mechanical hysteresis to such a complete and effective extent. It was applied both to single layers and to the assembled pole and the results obtained were more than satisfactory, being able to reproduce the experimental data to within 10% in the worst case. In any case, the new model better reflects the elastic modulus of the pole than analytical calculations: the weighted sum of the Young's modulus of the two layers gives in fact an overestimation of the pole Young's modulus by 50%.

Over-dimensioned cables were also implemented, to represent the unstressed cables: this posed many problems from the numerical convergence point of view, having to work with a coil greater than the surrounding structure. Also, the materials used for the cables were the object of some studies; indeed they had been considered isotropic. Measurements performed by other labs showed that this is not the case. An implementation of the model was done to take into account the anisotropy of the material, but this was proved to be not relevant for the result of the simulation. Anisotropy was thus neglected for sake of a reduced complexity.

The trustworthy and accurate description of the mechanical measurements on assembled poles may be considered the strong basis of what followed, which is the simulation of the collaring process (for which a 3.2-mm-thick shim was computed and found larger than the values normally used by the producers) and the cool-down process. The latter represents another original part of the job, for the way it is simulated and the results it leads to. It required, first of all, the determination of an average integrated thermal contraction coefficient, deduced by reproducing the experimental measurements performed in several labs: 0.003 mm/m was indeed used in the cool-down simulation. The dynamics of the cool-down was then represented through an ad-hoc algorithm to scale in temperature and contemporarily change the superconductor mechanical properties, increasing the rigidity as the temperature reduces. Finally, a pseudo powering was carried out, by inserting in the model the map of forces calculated inside the dipoles. What resulted is an unexpected distribution of stresses: both inner and outer layer cables suffer from a loss of stress, but they are anyway strongly constrained on the external side. The high gradients developed suggest that no global cable movement can happen and the training quenches possibly originate from a frictional motion of strand rather than the movement of an entire cable; in particular, the

pole turn of each layer is extremely critical, since these cables are also those subjected to the highest Lorentz forces and those with the lowest stress on the inner side. The data from the test results of SM18 and the precise localization sometimes obtained seem to confirm this hypothesis; recent quench studies carried out with the magnets installed in the LHC tunnel also support the localization.

If further confirmed, the present model could possibly help in understanding the reason why, regardless of the excellent performance of the LHC-class magnets, some poor behaviour is sometimes observed: the quenches could be reduced by, for example, a different shape of the collar. This would require a complex parametric study which goes far beyond the temporal limit of this thesis. In the meanwhile, a validation of the present model could come from the comparison with the finite element reproduction of the old magnet design and the simulation of its weaknesses; again, this could not be completed in a short time and could become the objective of one of the possible developments of this job. Moreover, another chapter that would deserve in-depth examination concerns the inclusion in the model of the insulating layers between the coil and the collars, plus the addition of the iron yoke, on which basis a full electro-magnetic analysis could be performed.

Last, but certainly not least, a full 3-D model could be built. The statistics shows, in fact, that only a very small percentage of the quenches are localized in the central part of the LHC dipole magnets, while most of them were detected on the extremities, most likely at the transition from the low to the high field region and in presence of the saddle-like shape. A 3-dimensional evolution of what proposed in this work would nevertheless require a step back towards a simplification of the structure, to comply with a faster numerical convergence.

APPENDIX 1
MANUFACTURING THE
DIPOLES AT THE THREE FIRMS
(UP TO PRE-COLLARING)

Preliminary remarks

In this appendix, a complete review of the components used and of the procedure followed to manufacture LHC arc dipole magnets is given, up to pre-collaring, for the three magnet producers (MP's): Alstom-Jeumont consortium (France), Ansaldo Superconduttori (Italy) and Noell (Germany).

It is important to note that this review goes back in time up to mid 2004, when the procedures for magnet production were already well defined, but some magnets exhibited performances below expectation. A comparative analysis was launched, with the aim of finding a possible explanation for these low performances in discrepancies in magnet assembly. This was the occasion for generating three documents (one per producer) which remain a reference for collared coils production.

The following paragraphs give a detailed description of the salient features common to the three producers, leaving to tables at the end of each section the task of depicting differences between producers.

A1.1. COMPONENTS AND TOOLING

A1.1.1. Cable insulation

The first and most important component is clearly the superconducting cable. Its parameters have already been described in Table 2.2, and it is the insulation which is of interest here. The 3 MP's apply the same scheme: 3 polyimide layers, where the 2 innermost ones (referred to as I1) are interleaved and butt-wrapped, and the outermost one (referred to as O1) is wrapped in opposite direction to I1, with a 2-mm-gap (Figure A.1).

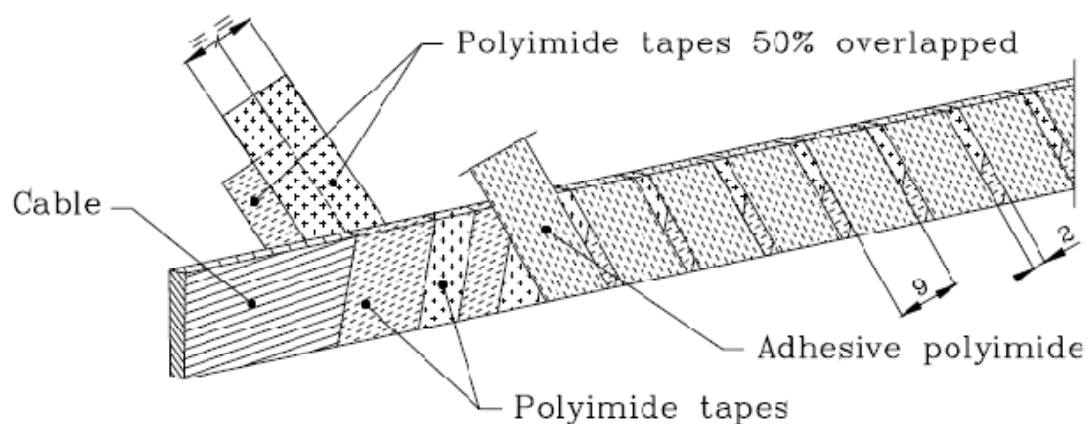


Figure A.1 _ Superconducting LHC cable insulation.

The O1 layer has an adhesive coating on the external surface that makes it non-sticky at room temperature and bonds to the insulations of the cables next to it at a minimum temperature of 185 °C and a moderate contact pressure (see in § 2.4 for details on the curing cycle).

Table A.1 lists the different tensions applied by the MP's, both on the polyimide tapes and on the cable, during cable wrapping. In Figure A.2, a detail of the application of the first two layers is shown.

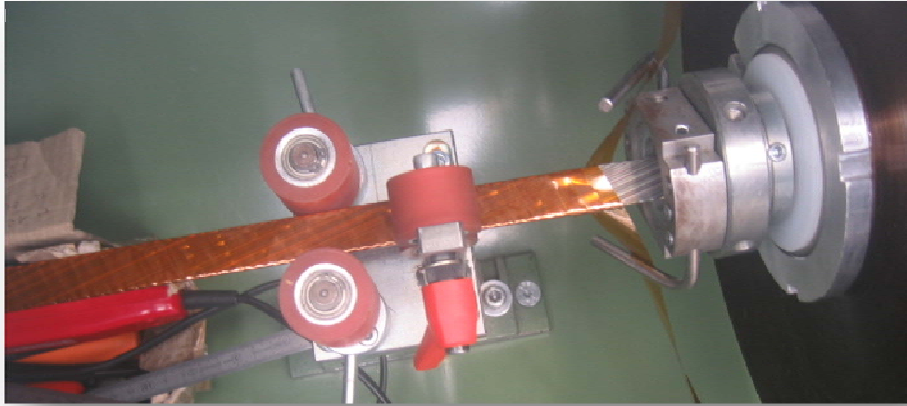


Figure A.2 _ Detail of I1 cable wrapping at Jeumont.

A1.1.2. Angular copper wedges

These spacers are made of OFHC copper and are inserted between blocks of conductors in order to produce the desired field quality and approximate quasi-circular coil geometry, thereby compensating for the insufficient keystoneing of the cables. They are provided by CERN to the MP's in lengths of 3.6 m and insulated by MP's with the same procedure as for the cables.

A1.1.3. End spacers

The end spacers are special, saddle-shaped, insulating fillers, designed to constrain the conductor to a consistent and mechanically stable shape in coil ends. Suitable shapes are determined using a “constant perimeter” approach combined with empirical methods, refined during prototyping; the thicker ones are produced by 5-axis machining of epoxy impregnated fibreglass thermoset, while the thinner ones - those having a maximum wall thickness below 10 mm (end chips) - are produced by injection moulding of polyetherimide resin with 30-vol% glass fibre loading (LHC Design Report [2004]). CAD files for machining are provided by CERN and can be modified by the MP's; manual re-machining on site is also applied, as a refinement. Furthermore, on the contact surfaces of all end spacers, a resin is applied by brush to increase bonding. A full set of end spacers is presented in Figure A.3. Local modifications by the three MP's are shown in Table A.1.

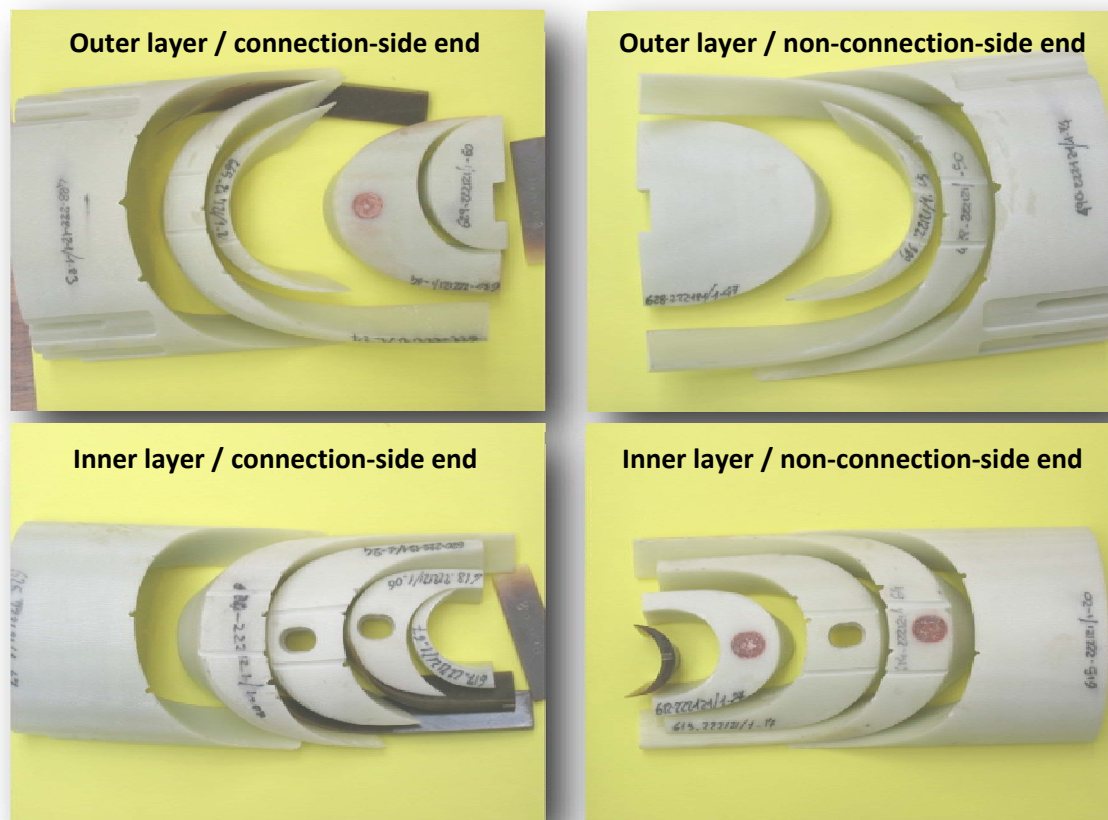


Figure A.3 _ Complete set of end spacers for LHC dipole coils.

A1.1.4. Inter-layer spacers

A slotted interlayer spacer made up of a polyetherimide resin, 10-vol% loaded with glass fibre (ULTEM 2100TM material) is positioned between the two coil layers. This provides channels for superfluid helium flow and gives an accurate mechanical support for the outer layer. The production was subcontracted to Tosti (Italy). A piece of inter-layer spacer is shown in Figure A.4.

A1.1.5. Ground plane insulation

Electrical insulation is required between the coils and their support structure (collars) sitting at ground potential. The ground insulation is composed of several polyimide film layers which are cut azimuthally and longitudinally for assembly. Besides its electrical function of preventing shorts from coil to coil and from coil to ground, it also has the role of providing slip surfaces during the collaring operation as well as a smooth surface over which both azimuthal and radial preloads are adequately distributed to avoid deterioration of cable insulation. The ground plane insulation is normally a 15-m-long polyimide, cold-folded sheet, and it is composed of several layers.

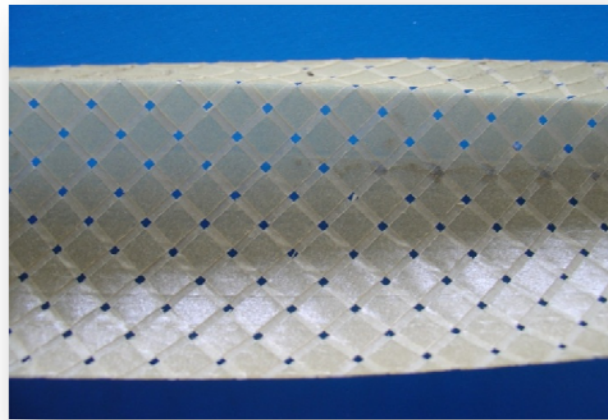


Figure A.4 _ Inter-layer spacer (also called fishbone for obvious reasons).

TABLE A.1 _ COMPONENTS AND TOOLING _ 1ST PART.

Alstom-Jeumont	Ansaldo	Noell
Cable insulation		
80-90% subcontracted to Buisin [till end 2004], which applies the tensions: Inner I1: 13-14 N Outer I1: 8-9 N O1: 7-10 N 20-10% in house on machine built by Innocable, with tensions: Cable: 18 N Inner & Outer I1: 13.5-15 N O1: 20 N	Subcontracted to Selva, which applies the following tensions: Cable: 130-170 N I1: 25-30 N O1: 15-20 N	Subcontracted to VonRoll Isola
End Spacers		
Machined by Tosti Modified during prototype phase so as to feed back initial winding results (to maintain proper angles of conductor blocks) Re-machined manually to add resin injection channels on inner surfaces of selected spacers (after resin application) AZ15 resin on the whole surface for all but the pole spacers of both layers	Machined by Tosti (partially modified design) Re-machined manually occasionally to remove sharp edges, to add resin injection channels on inner surfaces of end saddles Araldite on the whole surface for the last spacer and on the upper half for all the others	Machined by Gatex (standard design) Re-machined manually to remove sharp edges, to file tips of 2 nd and 3 rd end spacers of inner layer, in order to prevent cable insulation damage during insertion and to add resin injection channels on inner surfaces of end saddles Araldite; a cycle of polymerization of the treated spacers is carried in oven

A1.1.6. Collars

The mechanical structure of the dipoles is designed to withstand the high Lorentz forces generated in the coils and to limit as much as possible their deformation over the range of operation. The materials used for the most highly stressed components have a high load-bearing capacity, high elastic moduli, good fatigue endurance and a good behaviour at cryogenic temperatures. The most important are the collars, which are fine-blanked out of 3-mm-thick austenitic steel sheets. The coils are assembled inside the collars and pre-compressed at room temperature.

There are two different collars producers (Malvestiti in Italy and FSG in Germany) and each MP assembles the collars in different pack length (see Table A.2 for details). Figure A.5 shows the example of the Ansaldo collar pack.

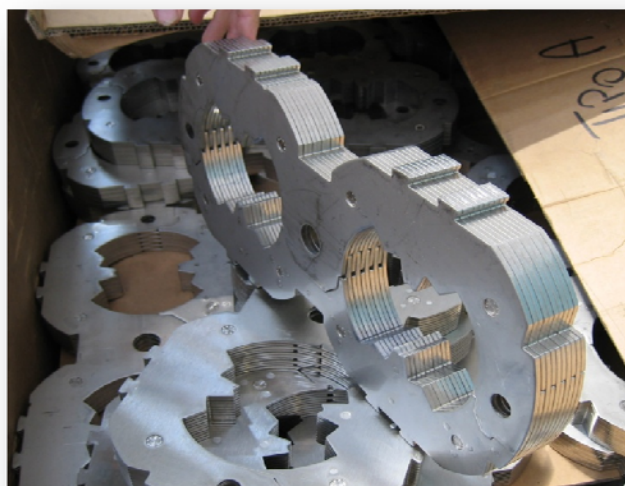


Figure A.5 _ Collar packs at Ansaldo.

A1.1.7. Winding machine and winding mandrels

The coils are manufactured in a clean area with adequate air circulation and air filtration. Coil winding is performed with “winding machines” that are complex tools consisting of a table supporting the winding mandrel and a suitable mechanism to move the cable spool and enable proper conductor positioning. For the winding of the layer ends, the mandrel is forced to rock around its longitudinal axis. The spool of insulated cable is held by a rotating support with a brake to control the tensile force on the cable; the tension applied to the cable is important to obtain reproducible and stable coils.

The winding mandrels (see Table A.2) can be either massive or laminated and have different dimensions for inner and outer coil layer; they can be covered with steel liners or sprayed with PTFE Teflon to prevent sticking. An example of winding machine is shown in Figure A.6.

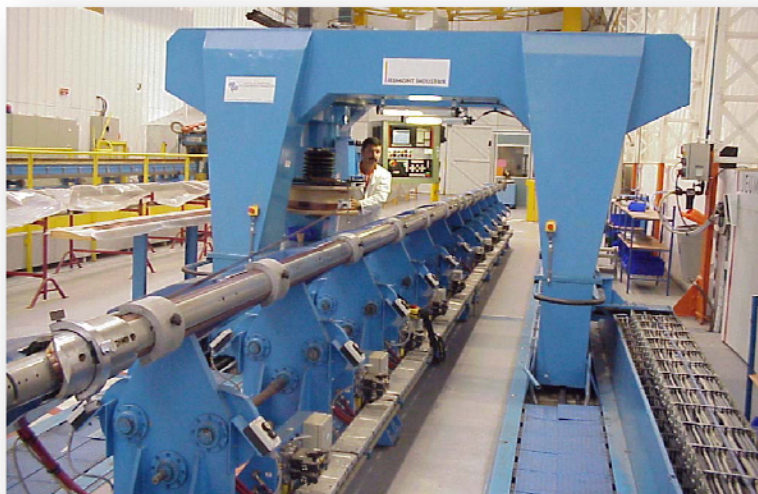


Figure A.6 _ Winding machine at Jeumont.

TABLE A.2 _ COMPONENTS AND TOOLING 2ND PART.

Alstom-Jeumont	Ansaldo	Noell
Collars		
Fine blanked by Malvestiti [nearly 90%]; about 15 out of 155 collared coils use FSG collars Assembled by pairs	Fine blanked by Malvestiti. Assembled in 90-mm-long (straight section) and 60-mm-long (ends) packs by Brandi	FSG (few exceptions: Malvestiti's collars were used at the beginning of the production) Assembled in packs of 82-83 mm
Winding machine		
Two operational machines (SDI): one for inner layers, one for outer layers	Three operational machines: one for inner layers, one for outer ones and the third one used indifferently for both types	Four machines (two dedicated to inner layers and two dedicated to outer layers)
Winding mandrels		
4 massive mandrels dedicated to inner layers and 4 massive mandrels dedicated to outer layers (3 regularly used + 1 spare) Each mandrel is made up of 7 chromium-plated, steel blocks tied up together and support a winding island made up of about 11 chromium-plated steel pieces Mandrels are sprayed from time to time with PTFE Teflon	Six laminated mandrels dedicated to inner layers and six laminated mandrels dedicated to outer layers	Six laminated mandrels dedicated to inner layers and six laminated mandrels dedicated to outer layers Mandrels are covered by ~1.5-m-long steel liners, which are replaced from time to time 15-m-long shims of nominal thickness (0.5 mm) mounted on pole (defining pole angle)

A1.1.8. Sizing bars, protection sheets and suiting covers

The sizing bars are used at the end of winding to azimuthally block the cable and keep the coil in position during removal from winding machine and preparation for curing. Shims may be used on top of the sizing bars to tune the arc length of the curing mould cavity (see Table A.3).

After coil winding and to ease curing, Jeumont has the particularity of relying on protection sheets and suiting covers. The protection sheets are 0.95-mm-thick (1500-mm-long in straight parts) and are made up of Z6CN 1809 steel; contact surfaces are sprayed with PTFE teflon from time to time. The suiting covers for the outer layers are around 1 cm thick, while the ones for the inner layers are thicker (Figure A.7), with the same external diameter; this allows treating both with the same curing press in case of shut down of one of them. The covers for the outer layer are 1000-mm-long in the straight part, 1010-mm-long over connection-side head and 1150-mm-long over non-connection-side head; for the inner layer, they are 500-mm-long in straight part, 510-mm-long over connection-side head and 650-mm-long over non-connection-side head. Sheets and suiting covers are put in place starting from the coil center and moving towards the coil heads; all joints of sheets, suiting covers, sizing bars, but also winding mandrel and winding island blocks are staggered with respect to each other.

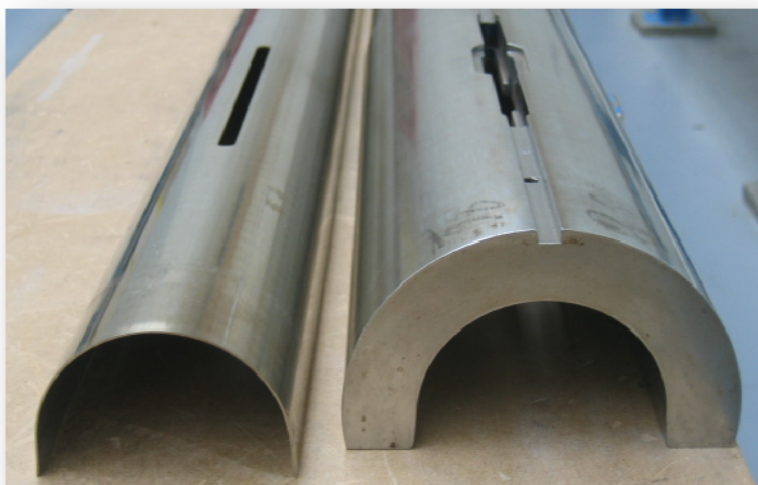


Figure A.7 _ Protection sheet and suiting cover for inner layer at Jeumont.

A1.1.9. Mould top hats and curing presses

The curing of the coils is carried out in moulds with heating systems that allow the adhesive on the polyimide tapes to be activated and to glue all the turns together, thus facilitating the subsequent phases in pole assembly.

The curing presses also include a mould top hat to fit the dimension of the coil being cured when a suiting bar is not present.

TABLE A.3 _ COMPONENTS AND TOOLING 3RD PART.

Alstom-Jeumont	Ansaldo	Noell
Sizing bars		
2 sets for inner layers and 2 sets for outer layers, numbered and always used at the same position; sets are not mixed. Mostly 1540-mm-long in straight part, 1320-mm-long over connection-side head and 1415-mm-long over non-connection-side head	<p>Five sets of sizing bars, used indifferently for inner and outer layers but never mixed; the bars are 1 m long in ends and 1.5 m long in straight part</p> <p>Two shims of adjustable thickness mounted on top of sizing bars:</p> <ul style="list-style-type: none"> - 1 mm thick, 15 m long shim (directly on bars) - 0.2 mm (inner)/0.3 mm (outer) thick, 14.2 m long shim (on top and centered wrt previous shim) 	<p>Each mandrel has a dedicated set of sizing bars (29 massive pieces)</p> <p>15-m-long shims of adjustable thickness mounted on top of sizing bars</p>
Mould top hats		
Integrated into presses (identical for the two presses)	Two inner and two outer, removable mould top hats	Integrated into presses
Curing presses		
1 old (revamped) Technique Réa machine, dedicated to outer layers (first used for 10-m-long prototypes) and 1 new CTE Systemi machine, dedicated to inner layers. Each machine has its own heating system (3000 l of oil, 220 kW heaters)	Two presses with independent pressure and heating systems. Initially, one was used for inner layers and the other one for outer layers, but, then, used indifferently for both layer types, since the mould top hats are removable	Two presses (one dedicated to inner layers and one dedicated to outer layers); mould top hat stays inside the press

**Figure A.8** _ Curing press at Noell.

A1.2. WINDING AND CURING

A1.2.1. Layer-jump preparation

Prior to winding, a procedure is applied by the MP's to prepare the layer-jump on the inner cable. This is a small portion of the inner layer cable which is used to connect with the outer layer cable on one magnet end. The first part of the preparation is common to the three MP's, that is removal of the conductor insulation and cleaning of the conductor with Scotchbright and alcohol. The second part is the shaping of the layer-jump itself (the mould used at Ansaldo is shown in Figure A.9), followed by the addition of a copper stabilizer; it is important to note that Noell uses a procedure which is different from the one recommended by CERN, since the stabilizer is put before formation of the layer jump shape.



Figure A.9 _ Shaping tooling at Ansaldo.

A1.2.2. Winding: mandrel covers, winding tension and duration

To maintain the cable at the start of winding, a small Cu block is soldered onto the extremities of both types of cables, as shown in Figure A.10 (only on inner layer cable at Jeumont).



Figure A.10 _ Cu block soldered on outer layer cable extremity at Ansaldo.

Since Ansaldo and Noell use laminated winding mandrels, they have to rely on mandrel covers to protect the cable from the laminations. These covers are blocked under the winding island on top of the mandrel before winding starts; small kapton pieces are put at their junction. In Figure A.11, the laminated mandrel with its green covers and island are shown as they are used in Ansaldo.

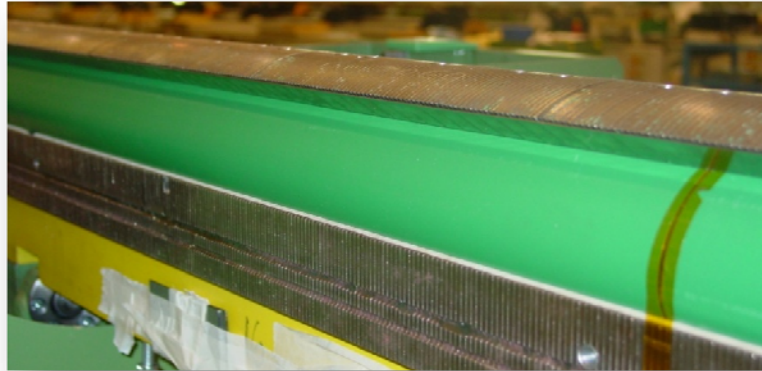


Figure A.11 _ Mandrel ready for winding at Ansaldo.

Concerning the tensions applied during winding of the coils and the winding duration, they are listed in Table A.4 for the three MP's.

TABLE A.4 _ WINDING _ 1ST PART.

Alstom-Jeumont	Ansaldo	Noell
Layer-jump preparation		
Conductor shaping and tinning (235°C) in dedicated tooling (steel with alu-dur insert)	Conductor shaping and tinning in dedicated tooling (chromium-plated)	Conductor tinning Layer jump formation
Mandrel cover		
No protection cover since the mandrel is not laminated	0.2-mm-thick, 800-mm-long stainless steel sheets coated with Teflon on their outer surface	0.5-mm-thick, ~1-m-long stainless steel sheets
Winding tension		
50 kg for straight sections of inner layers, 30-35 kg for heads (10-20 kg for the first turn); 40 kg for straight sections of outer layers, 25 kg for heads (increase from 10 to 10 kg for first half turn)	50 kg for straight sections of inner layers, 25 kg for heads (23 for the first 4 turns) 50 kg for straight sections of outer layers, 28-30 kg for heads (26-27 for first turn)	50 kg for straight sections of inner layers, 30 kg for heads 40 kg for straight sections of outer layers, 30 kg for heads
Winding duration		
~8 hours per layer	Less than 6 hours per layer (around 4 hours without pauses)	Maximum of nine to ten hours per inner layer (less for outer layers)

A1.2.3. Support of coil heads during winding

The coil heads must be supported during winding, since the saddle shapes assumed by the cables render them highly unstable. Several types of supports have been developed by the MP's: radially (to prevent the cables from slipping one over the other at the coil turnaround), azimuthally (all along the coil as winding progresses) and axially, after winding completion. Some examples are presented in Figure A.12, and a list for the three producers is given in Table A.5.

TABLE A.5 _ WINDING _ 2ND PART.

Alstom-Jeumont	Ansaldo	Noell
Radial support on ends (Figure 12)		
290-mm-long, chromium-plated steel covers (internally sprayed with PTFE Teflon at regular intervals); covers are moved manually along the mandrel as winding proceeds Note that covers are held in place throughout winding and curing and are only removed after curing	Plastic (PA6G) or aluminum (internally coated to reduce friction) covers; covers are moved manually along the mandrel as winding proceeds by means of a long screw	Multi-arm 'octopuses' positioned manually; octopuses are left on the coil heads after winding completion until they are replaced by ~50-mm-wide steel clamps
Azimuthal support		
Each winding machine is equipped with 14 x 200-mm-wide azimuthal pushers (starting from one end, the distances between pushers are: 5 x 1160 mm, 920 mm, 540 mm, 920 mm and 5 x 1160 mm); the pushers are set up manually as winding proceeds	Conductors entering and exiting coil heads are supported azimuthally throughout winding by pneumatic pushers Spirex 1500: old design, 8 x 40-mm-wide pushers in the straight section plus 280 mm-wide pushers over heads Spirex 1000: 14 x 50-mm-wide pushers in straight section plus 80-mm-wide pushers over heads Insertion of last spacer requires lowering down azimuthal pusher over coil heads While turning around the heads, only the nearby pushers are lowered for accommodating the cable	Conductors entering and exiting heads are supported azimuthally throughout winding by dedicated 180-mm-long pusher bars mounted and dismounted manually Straight sections supported by ten ~10-cm-long automatic pushers on each side
Axial support (after winding completion)		
Support pieces with two pushing cylinders are mounted on extremities of winding mandrel; these are used during curing to apply axial loading (fixed force but not fixed position) onto coil heads by means of pneumatic pumps	Support pieces with four screws (to apply axial loading onto coil heads) are mounted on extremities of winding mandrel (while the azimuthal pushers are kept lowered); the support pieces are left in place throughout curing	Support pieces with four set screws to apply axial loading onto coil heads are mounted on extremities of winding mandrel; the support pieces are left in place throughout curing

TABLE A.6 _ WINDING 3RD PART.

Alstom-Jeumont	Ansaldo	Noell
Miscellaneous		
<ul style="list-style-type: none"> - Three inner-layer end spacers are fixed by screws to winding mandrel - Gaps between angular wedges are controlled by means of small plastic pieces, implemented during winding and removed at the time of curing preparation - Vetronite spacers inserted below layer jump to azimuthally support second turn cable during winding; 220-mm-long, teflon sheet inserted between spacer and cable to prevent bonding during curing - Since pole set 115, 125-microns-thick kapton shims added on midplane turns of inner and outer layers (in order to reduce arc length of curing cavity and achieve smaller azimuthal coil size), which are removed after curing; in a few cases (<i>i.e.</i>, 1108 and 1127) a 2x125-μm-thick kapton shim is added - ~500-mm-long temporary, plastic sizing bars are applied at the end of winding 	<p>Tedlar sheets are inserted between first and second turn over 0.6-0.7 m from connection-side end to avoid gluing of conductor sections needed for splicing (only on inner layer)</p>	<p>For outer layer: connection-side-end pole spacer used during winding and curing is made of copper; replaced by G11 afterwards</p> <p>Teflon sheets inserted between first and second turn over one meter from connection-side end to avoid gluing of conductor sections needed for splicing (on both inner and outer layers)</p>

**Figure A.12** _ Some of the fixtures used by the MP's to support cables during winding: at Jeumont (top-left corner), at Ansaldo (right column) and at Noel (bottom-left corner).

A1.2.4. Curing

After winding, each layer is moved to the curing preparation bench, where different procedures are applied, as detailed in Table A.7.

TABLE A.7 _ CURING _ 1ST PART.

Alstom-Jeumont	Ansaldo	Noell
Curing Preparation		
<ul style="list-style-type: none"> - Temporary sizing bars are replaced by final ones - 700-mm-long, 0.025-mm-thick adhesive kapton tapes are added on midplane of non-connection-side heads of both layers - AZ15 resin is applied on top of all conductor blocks of coil heads up to ~2 cm into straight part - Protection sheets and suiting covers are mounted, together with a fixture to apply axial loading over coil heads during curing (by means of two pistons) - Dressed layer is moved to curing press bed(which was raised by 2 mm compared to initial design by means of a 15-m long sheet made up of tool steel); further corrections are applied over mandrel extremities by means of additional 460-to-480 mm stainless steel strips; strips thicknesses have been optimized for every mandrel in use - Removal of the three screws fixing the inner layer end spacers to winding mandrel - Implementation of hydraulic jack to apply axial loading (30 bars total over two pistons) - Coil cavity is determined by closing gap between sizing bars and mould top hat 	<p>Coils are protected by 1.5-m-long, 0.8-mm-thick steel covers (internally coated with Teflon), which are replaced from time to time</p> <p>Note that no Teflon tapes are put at their junctions</p>	<ul style="list-style-type: none"> - Coils are covered by 500-mm-long covers, with Teflon tapes at their junctions (later changed to Apical to have better protection) - Additional Teflon fillers are positioned on conductor blocks of coil heads with large gaps; the fillers are held in place by adhesive Kapton tapes (the fillers are removed after curing completion)



Figure A.13 _ Example of Teflon fillers added at Noell on conductor blocks.

The curing cycle was defined by CERN and includes a temperature ramp up to 190 ± 3 °C under a maximum pressure of 80-90 MPa. The aim of the curing operation is to activate the polyimide adhesive on the outer surface of the outermost insulating layer, so as to glue the turns together, and define the coil geometry, that must respect a tolerance of ± 0.05 mm, with a standard deviation, along coil length, of ± 0.03 mm.

The MP's use several variants of the curing cycle, and two of them encountered problems related to it: at Jeumont, large peak-to-peak variations were observed due to inaccurate molds, and at Noell a drift of the average sizes was sometimes recorded.

TABLE A.8 _ CURING _ 2ND PART.

Alstom-Jeumont	Ansaldo	Noell
Cycle		

Temperature is controlled by means of 4 temperature sensors.

The initial cycle (used until cold mass 48) includes a temperature step at 100 °C to allow creep of polyimide.

Starting with cold mass 49, the temperature was risen from 100 to 130 °C to accelerate creep, but without modifying the pressure cycle.

After various trials (P.S. 49-115: intermediate step at 130°C; P.S. 115-130: intermediate step at 140-150 °C; P.S. 130-146: various pressure steps during ramp up), the pressure profile was modified to ensure that the coils are under significant compression as soon as the temperature exceeds 100 °C.

The standard profile (used since PS 147) includes successive pressure plateaus at ~50 MPa, ~80 MPa and ~100 MPa at high temperature.

Post-curing inspection

After undressing, a visual inspection is carried out;

steel end pole spacers are removed and the holes in inner-layer end spacers are filled with impregnated glass-fiber;

125-micron-thick kapton shims over midplane turns are removed

A typical treatment is shown in Figure A.14.

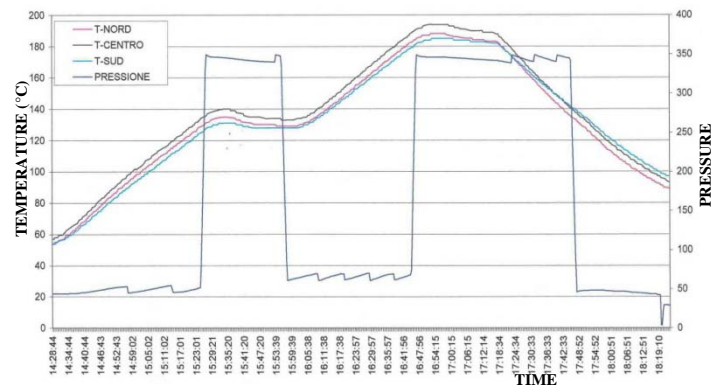


Figure A.14 _ Example of curing cycle at Ansaldo.

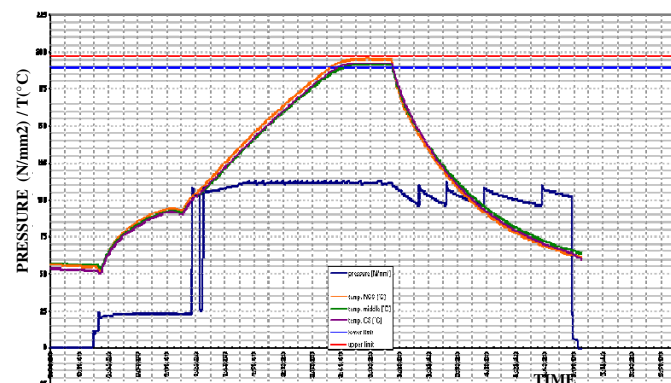


Figure A.15 _ Example of curing cycle at Noell.

A1.2.5. Re-surfacing

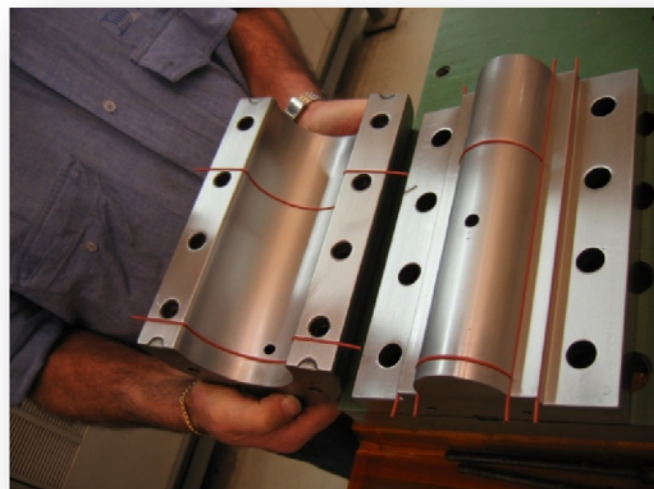
Once the layer has been cured, gaps are still present over the saddle-shaped cables in the coil ends, due to the slope of the cables themselves. For this reason, an operation is carried out to fill these gaps with resin in order to provide a uniform surface to the collars and prevent the cables from having a free space to move in. Two kinds of resin (Stycast and Ecobond) are used by the MP's, and different mould geometries and procedures have been developed, which are summarized in Table A.9 and illustrated in Figure 16 for the Ansaldo case.

TABLE A.9 _ RE-SURFACING _ 1ST PART.

Alstom-Jeumont	Ansaldo	Noell
Re-surfacing		
Layers are mounted on temporary mandrels enabling careful positioning of "trimmed" end pole spacers Stycast; injected from top. Ecobond was used from PS 131 to PS 158. Back to Ecobond later on (when solved the difficulty of supply)	Stycast; injected from bottom	Ecobond; injected from bottom
Mould geometry		
<ul style="list-style-type: none"> - Top part covers coil head and extends 150 mm over straight section; nominal dimension over coil heads, but part extending over straight part is given a conical shape to achieve a 0.2 mm clearance at extremity. - Bottom part: curved inner part of mould is lifted by 0.2 mm, to ensure that contact with coil first occurs on coil inner surface rather than on mid-plane 	Same as curing mould with upwards curvature	Same as curing mould; with curvature downward Small (a few hundredth of a millimeter thick) shims are added on inner parts of mould to ensure that contact first occurs on coil inner surface rather than on mid-plane
Mould closure		
Closed by 2x3 hydraulic jacks, dimensioned to apply 30 MPa	Mould is closed by applying a given torque on four bolts on each side (corresponding to a total force of 50 tons) After closure, mould exhibits a ~0.3mm gap between top and bottom parts towards coil straight section	Since the cavity has the nominal geometry, the two halves are tightened until gap closure

TABLE A.10 _ RE-SURFACING 2ND PART.

Alstom-Jeumont	Ansaldo	Noell
Heating cycle		
Resin is pre-heated to 75 °C for 30 min and injected into mould for 25 min (under pressure); then mould is heated up to 120 °C for 2 hours; finally it is let to cool off naturally and is opened at 40-50 °C Note that mould is equipped with four heaters on top part and 2 heaters on bottom part to ensure good temperature uniformity	Resin is pre-heated to 80 °C and injected into mould; then mould is heated up to 100 °C for 2 hours	
Fixture sealing		
For inner and outer layers: 140 mm from non-connection-side end (first two turns free of resin)	For inner and outer layers: 140 mm from non-connection-side end (first two turns free of resin)	For inner layer: 140 mm from non-connection-side end (first two turns free of resin) For outer layer: the joint of the internal half of the mould has been modified, to leave the first two cables of outer layer free of resin and to block resin propagation in straight part
Finishing		
Ecobond is applied by hand to fix end pole spacer and to cover first conductor block (located outside seal of resurfacing fixture, on both layers) Defects are fixed by applying Ecobond manually	Manual filing of extra resin at the point of resin alimentation	Defects are fixed by applying Ecobond manually

**Figure A.16 _ Re-surfacing mould at Ansaldo for the inner layer.**

A1.3. YOUNG’S MODULUS MEASUREMENTS AND SHIMMING

To verify coil dimensions and to compute the thickness of the shims necessary for pre-loading the coils when assembled into the collars, measurement of the azimuthal size of the coils under pressure are performed on individual layers and assembled poles (see Table A.11); presses as the one shown in Figure A.17 are used. (This kind of measurements is recalled in Chapter 5 for the definition of the finite element model).

TABLE A.11 _ YOUNG’S MODULUS MEASUREMENT.

Alstom-Jeumont	Ansaldo	Noell
Devices		
Only on poles, using Jeumont old machine	Layer: revamped HERA machine for individual layers Pole: IMM machine	Layer: BNN machine already used for prototypes and revamped for series production
Sampling		
Since pole set 136: - 9 points on one pole of each set (1 on each head, 2 on ramp-splice, 5 on straight parts); - 4 points on all other poles (1 on each head, 2 on ramp splice, none on straight part) Measurements over ramp splice are used to determine shims to be implemented on the two G10 filling pieces mounted behind splice box	1 inner and 1 outer layer per cold mass, with 14 points of measurement in the straight part Replaced layers are measured systematically Poles are measured in case of problems	Measurements are performed on individual layers, over three points determined after a statistical study



Figure A.17 _ Device for Young’s modulus measurements at Jeumont.

A1.3.1. Pole assembly

Next step in production is the mounting of the outer layer over the inner one, with insertion of the inter-layer spacer described in §1.4 (see Table A.12 for details).

Concerning the soldering between the cables of the inner and outer layers, after removal of the insulation, the splicing is carried out in a dedicated tooling, by heating up an additional piece of tin-based material (a strip of high conductivity copper has already been soldered to the inner cable during shaping to thermally stabilize and mechanically stiffen the ramp and its curved portion). Re-insulation of the soldered cable section follows, with the mounting of the layer-jump box. In Figure A.18, an example of splice before and after soldering is shown, together with the tooling used at Jeumont and Ansaldo for splicing.

TABLE A.12 POLE ASSEMBLY 1ST PART.

Alstom-Jeumont	Ansaldo	Noell
Positioning of inter- layer spacer		Preparation
<ul style="list-style-type: none"> - Over heads: two points of glue (cyanocrilate IS12) - Straight section: one 10x10 mm piece of double face adhesive (20 µm polyester + 3 µm adhesive, supplied by MICEL) at both extremities of each 1-m-long piece 		~300-mm-long adhesive Kapton tapes added on midplane to protect coil heads (thickness: 25 µm + adhesive)
Inter-layer splicing		
Heating up of 2 x 15-mm-wide, 0.05-mm-strips of Sn 96% Ag 4% to a maximum temperature of 245 °C (temperature is controlled by thermocouples) Up to P.S. 130 tin was also added in the channels of the tooling	Heating up of a 15x0.2 mm ribbon of Sn 95%, Ag 5% to a maximum temperature of 240 °C (temperature is controlled by two thermocouples)	Heating up of a 14x0.2 mm film of Sn 96%, Ag 4%; heated to 235 °C (temperature on tooling)
Re-insulation with two butt-wrapped layers of I1 Apical, shifted by 50% and one layer of 12-mm-wide pre-impregnated glass-fibre tape (Isovolta IP HR108P-37), wrapped with a 2 mm gap	Re-insulation with Apical-tape Typical cable insulation: two butt-wrapped layers of I1 and one layer of O1, wrapped with 2 mm gap Starting from magnet 31, the two butt-wrapped layers have been substituted by a single 50%-overlapped layer	Re-insulation with Apical-tape (trials with pre-impregnated fiberglass tape to achieve better adhesion in layer-jump box and avoid use of araldite had been attempted but rejected) The insulation is the same as for the cables: two butt-wrapped layers of I1 and one layer of O1
Mounting of layer-jump box, with temporary Al filling pieces (to prevent gluing during re-conditioning and allow shimming of final G10 filling pieces after azimuthal coil size measurements)	Mounting of layer-jump box (the filling pieces behind the layer jump boxes are made up of two parts as in CERN design) The box is sometimes manually re-worked for accommodating the re-insulated cable Spot gluing of detached conductor section with Araldite	Mounting of layer-jump box (the filling pieces behind the layer jump boxes are made up of two parts as in CERN design) Spot gluing of detached conductor section with Araldite



Figure A.18 _ Left column: on the top, splicing tooling at Jeumont; on the bottom, tooling at Ansaldo. Right column: splice before and after formation.

After splice formation, the connection-side end of the pole is re-cured “in-situ” and finished up according to the different procedures detailed in Table A.13.

TABLE A.13 _ POLE ASSEMBLY 2ND PART.

Alstom-Jeumont	Ansaldo	Noell
Re-curing of splice region		
Over a length of about 650 mm using dedicated top hat, made up of a cover and two liners fixture closed by 2x7 hydraulic jacks (500 bars) The re-curing cycle is: 130 °C for one hour (no need to go higher, thanks to the use of pre-impregnated glass fiber tape) with an applied pressure over the coil of 30 MPa	Over a length of about 600 mm using dedicated top hat and press The top hat is made up of the same laminations as the outer-layer curing mould, and the coil head is protected by a similar steel cover The cycle is: ramp to 130 °C at 0 MPa, application of pressure for mould closure and ramp to 180 °C for 30 min	Over a length of about 2 meters in a mould having nominal dimensions (ramp to 50 °C at 0 MPa, ramp to 70 MPa for 1 hour, ramp to 100 °C for 15 minutes while at 70 MPa)
Current lead repair	Finishing	
If mid-plane turn leading to current lead is detached from layer, it is repaired by application of an epoxy-type resin (developed by Jeumont); resin normally cures at room temperature, but cycle is accelerated by heating up coil head to 80 °C (in a dedicated fixture)	Grooves for quench heaters are manually finished to eliminate sharp edges	

A1.3.2. Pole end measurement and shimming

After having assembled them, the pole ends have to be measured and shimmed in order to get a smooth transition of the mechanical pre-stress from the straight part (70-75 MPa) towards the extremity (20-30 MPa); the three MP's use to divide this region in either three or five sections. Measurements are performed in a rigid cavity of nominal dimension, using a standard press (CEP-Rejlers) provided by CERN. In some cases, nevertheless, the press is not always used. As can be seen in Table A.14, Ansaldo applies higher pre-stress values on ends.

Concerning the shimming, adding an extra layer of polyimide insulation between the poles is an option for fine-tuning magnetic field harmonics. This option (with an extra layer thickness of 125 μm on both inner and outer layers) is implemented in cross-section design number 3.

TABLE A.14 _ POLE ASSEMBLY 3RD PART.

Alstom-Jeumont				Ansaldo				Noell			
Measurements											
Old Jeumont press and CEP (Rejlers) press in case of problems				CEP (Rejlers) press				CEP (Rejlers) press Averaged over 5 sections (starting from coil ends: 40 mm + 4 x 35 mm)			
Target profile											
Target [MPa]	Min [MPa]	Max [MPa]	Section	Target [MPa]	Min [MPa]	Max [MPa]	Section	Target [MPa]	Min [MPa]	Max [MPa]	Section
30	10	50	3	60	40	70	5	25			5
60	40	90	2	65	40	70	4	25			4
100	80	130	1	70	50	80	3	35			3
			straight part	75	50	80	2	55			2
				80	60	90	1	75	80/60 (in/out)	110/120 (in/out)	1
							straight part				straight part
Shims are made up of three layers of 125-μm-thick polyimide tape graded in diminishing steps (170 mm, 145 mm, and 120 mm long starting from coil end)				Shims are made up of layers of 125-μm-thick polyimide tapes (sometimes also 60 μm) assembled in a staircase fashion (with 5 mm steps between layers) and are divided up in 3 parts (starting from pole ends: 70 mm + 70 mm + 40 mm)				Shims are made up of layers of 125-μm-thick polyimide tapes assembled in a staircase fashion (with 2 to 3 mm steps between layers)			
Since pole set 90, an additional pyramidal set of shims was added on both sides of both outer layer coil heads. The pyramid is made up of three 125-μm-thick, polyimide steps (which are 80 mm, 60 mm and 40 mm long) and its center is located 110 mm from the layer ends. It is meant to compensate the dip observed in coil heads in the area where the conductors exit the straight section and start its turnaround								Generally no shims are applied in sections 1 and 2 The pressure profile is 5 MPa lower than the above value because of the introduction of the mid-plane shims, not present during measurements			

A1.4. GROUND PLANE INSULATION AND PRE-COLLARING

Once the two poles have been assembled around the cold bore tube, with the proper shim in between, the ground plane insulation (already described in § 1.5 and detailed in Table A.15 and Figure A.19) has to be mounted. In the straight part, it is made up of 15-m-long polyimide sheets, while over the ends four layer of ~200-mm-long polyimide sheets are applied according to slightly different procedures.

TABLE A.15 _ PRE-COLLARING 1ST PART.

Alstom-Jeumont	Ansaldo	Noell
Ground plane insulation		
Heads		
<p>Four layers of 200-mm-long, 360° polyimide sheets: junction of first (innermost) layer is 8 mm away from pole plane; junction of second layer is located at 180° from that of first layer; junction of third layer is located at 180° plus 18 mm from that of second layer; junction of fourth (outermost) layer is located at 180° from that of third layer; the fourth (outermost) layer is 50 mm shorter than the others and is aligned to coil assembly end, thereby leaving a gap towards coil straight section</p>	<p>Four layers of ~200-mm-long, 180° polyimide sheets (with junction at the pole assembly mid-plane), held in place by small adhesive Kapton tapes which are removed when putting the coil protection sheets</p>	<p>Four layers of ~200-mm-long, 359° polyimide sheets (shifted by 90°), held in place by small adhesive Kapton tapes (two layers overlapped by a few millimeters with straight-section ground plane insulation)</p>

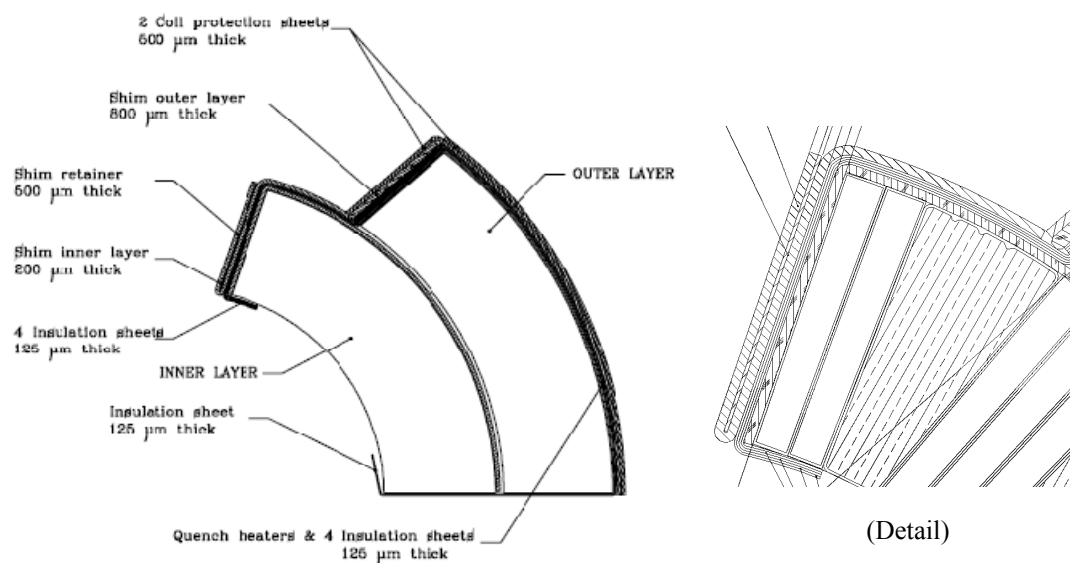


Figure A.19 _ Insulation scheme for pole assembly (left), with a detail of the last turns of inner layer (right).

The collaring shims are implemented at the layer poles (see Figure A.19) and they provide a means to control the pre-loading of the coils and field harmonics of the magnet. The shims are inserted inside special retainers on the inner layers. These components are made of a folded metal sheet and prevent the shims from slipping during assembly and collaring. On the outer layer, the shims lie directly on the ground insulation and they are protected from the collars by an extension of the so-called coil protection sheets which are positioned between the ground insulation of the outer layer and the inner surface of the collars. These elements prevent damage to the insulation from contact with the serrated edges of the collars. In addition, the coil protection sheets help to avoid ground plane insulation damages and provide continuous support to the conductors. A complete scheme of the insulating layers installed in magnets is shown in Figure A.19, whilst details on dimensions and types of such insulations are listed in Table A.16.

TABLE A.16 _ PRE-COLLARING 2ND PART.

Alstom-Jeumont	Ansaldo	Noell
Collaring shims		
Outer layers: 15 x 1 m long vetronite pieces (0.8 mm thick) Inner layers: 15 m long stainless steel shims (0.2 mm thick since 1083; 0.7 mm thick prior to 1083)	Outer layers: 3 x 5 m long vetronite pieces (0.8 mm thick) Inner layers: 15 m long stainless steel shims (0.2 mm thick)	15 m long
Shim retainer		
18 x 0.8-m-long bronze pieces whose design has evolved in time. Prior to 1083, the thickness was 0.25 mm with a double layer over outer surface of inner coil. Since 1083, it has been 0.5 mm thick, with a single layer over inner coil outer surface to enable a visual inspection of the presence of the shim. Material is mainly CuSn ₉ P H12	18 x 0.8-m-long stainless steel pieces (0.8 mm thick) on inner layer	1.5 m long
Coil protection sheet		
Over heads, 2 layers of bronze sheets: inner layer made up of 2x0.5-mm-thick, 190-mm-long, 180° sectors; outer layer made up of 2x0.5-mm-thick, 440-mm-long, 100° sectors (extending partially over straight section) plus 2x0.5-mm-thick, 190-mm-long, 80° sectors (extending only over coil heads)	Over heads: 2 x 2 x 180° NIPPON STEEL YUS 130S (0.5 mm thick) sheet, with junction in polar position and a small junction offset between layers	Over heads: 2 x 359° NiZn alloy (mounted with 180° shift). Changed to Nippon steel after coil protection sheet crisis (February-March, 2004)
Over straight section: 2 layers of 0.5-mm-thick 960-mm-long bronze sheets, assembled with a 1.5 mm gap. Since 1055, material is CuSn ₉ P H12. Prior to 1055, it was mostly CuSn ₃ Zn ₉ H12	Over straight part: 1-m-long NIPPON STEEL YUS 130S sheets plus a final piece of 800 mm of the same material for length compensation (both types have nominal cross-section and thickness)	

A1.4.1. Pre-collaring

At this stage, the collars are mounted manually but not locked because of the oversized dimensions of the coils which are not yet under compression; different systems of clamping are used by the MP's to temporarily support them (the case of Jeumont is shown in Figure A.20). Different procedures are also applied for coil length adjustment. See Tables A.17 and A.18 for details on pre-collaring and finishing.

TABLE A.17 _ PRE-COLLARING 3RD PART.

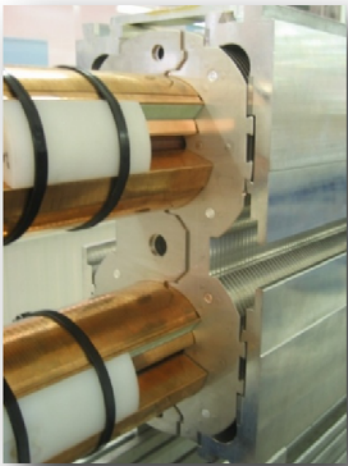
Alstom-Jeumont	Ansaldo	Noell
Preparation		
	Molikote powder on the outer surface of coil protection sheets and on inner surface of collars	Teflon spray over collaring shoes
Mounting of collar pairs/packs		
<ul style="list-style-type: none"> - Pairs are mounted manually over a length of 200 mm - Structure is pressed and held in position by means of clamps 	<ul style="list-style-type: none"> - Three benches operated in parallel, each equipped with an independent small press - Starting from layer jump; they are forced in place by means of the small press and are locked around the pole sets by 60/90-mm-long, 11-mm-diameter rods (two packs at a time over coil heads, three over straight section) - The collar pack length is adjusted at the non-connection side, a couple of packs before the end 	<p>Collar packs are mounted manually by set of two, starting from layer jump; they are forced in place by means of a small press and are locked around the pole sets by 160-mm-long (under-sized) rods</p>

Figure A.20 _ Example of pre-collaring at Jeumont.

The next important steps in assembly are the locking of collars with tie rods, under a press (as described in Chapter 6), the addition of the iron yoke laminations and the soldering of the two halves of the shrinking cylinder and the end covers. The cryostating is done at CERN. The description of these phases goes, anyway, beyond the scope of this work and they are recalled only for completion.

TABLE A.18 _ PRE-COLLARING 4TH PART.

Alstom-Jeumont	Ansaldo	Noell
TABLE A.10 PRE-COLLARING – PART 1		
Miscellaneous		
A cross-check for coil end shimming is done, consisting in measuring the pressure needed to insert 11 mm rods on first three packs over coil heads		
Length adjustment		
Before pole assembly		
- Targets are mounted on coil heads so as to measure inner length with Leica - Pole spacers are milled to appropriate dimension (so as to achieve a tolerance on overall length of the order 2 tenths of a millimeter)		
After pole assembly		
Specific tooling used to align the two layers with respect to the inner sides of end pole spacers; excessive length is trimmed with a circular saw; operation is repeated at both ends	Pole length is adjusted by precisely mating the two layers at the connection-side ends and by trimming the non-connection-side ends (when too long) with a circular saw	Pole length is adjusted by cutting both ends with a circular saw
After collaring		
After collaring the length is not adjusted, but differences are compensated by the end plate screws	As a result of collaring, the outer layer is usually more elongated than the inner layer. Compensation for differential elongation and for vertical alignment is implemented by means of vetronite semi-circular pieces. This compensation is all the more important in the Ansaldo design, because the subsequent axial loading of coil heads is applied by means of a stainless steel plate which needs to be in good contact	
Kapton reinforcement over outer layer midplane.		
The 0.025-mm-thick kapton reinforcements over midplane of outer layer are applied in two phases to limit the risks of damage during layer or pole handling: a 650-mm-long piece is applied over connection-side head prior to layer mating, while the rest is applied at the end of pole assembly prior to shipping to Alstom.		



Europass Curriculum Vitae

Personal information

Surname(s) / First name(s)	Pojer Mirko		
Address(es)	6, Chateau Banquet CH-1202 Geneva (Switzerland)		
Telephone(s)	+41 (0)22 344 38 43	Mobile	+41 (0)76 487 24 82
E-mail(s)	mirko.pojer@cern.ch		
Nationality	Italian		
Date of birth	5 Mar 72		
Gender	Male		

Desired employment / Occupational field	Project manager in the domain of applied Physics and for R&D projects.
--	---

Work experience

Dates	1 Nov 06 - 31 Dec 08
Occupation or position held	Project Associate as Engineer in the Hardware Commissioning Coordination for the LHC project
Main activities and responsibilities	<ul style="list-style-type: none">- Planning and scheduling of all installation phases and test activities.- Compilation of detailed and comprehensive procedures for the test of the superconducting circuits and the associated technical systems (power converters, superconducting links, HTS current leads, quench detectors, energy extraction systems and secondary services).- Definition and planification of systematic, as well as specific actions to guarantee an excellent quality assurance.- Coordination of the tests for the qualification of the individual systems (vacuum, cryogenics, interlocks, magnet protection, power converters).- Follow up of electrical and mechanical non-conformities.- Powering test coordination and transition handling from hardware commissioning to cold check-out.- Report to the project management and the steering committees.
Name and address of employer	CERN - European Organization for Nuclear Research INFN - Istituto Nazionale di Fisica Nucleare
Type of business or sector	Hardware Commissioning coordination and QA assessment
Dates	1 Nov 03 - 31 Oct 06
Occupation or position held	PhD Student
Main activities and responsibilities	<p>The aim of my PhD project was to build a finite element model (using ANSYS code) of the LHC dipole coil cross-section, with hysteretic, non-linear mechanical behaviour and single turn description. This may be used to explain instabilities sometimes observed in the dipoles and suggest an interpretation of the quench origin. Statistical collection and treatment of quench results of the whole magnet production was also performed.</p> <p>During my work I also visited the firms responsible for the production of the dipoles to compile detailed reports on the different assembly procedures and to participate to the disassembly of bad-performing magnets, giving a useful feed-back to the industries and suggesting corrective actions to be taken.</p>
Name and address of employer	CERN & EPFL (Ecole Polytechnique Fédérale de Lausanne)
Type of business or sector	Magnet design and quench characterization

Dates	1 May 01 - 31 Oct 03
Occupation or position held	Fellowship
Main activities and responsibilities	In the framework of the LHC-MTA Group activity, I participated actively in cold tests of the LHC superconducting magnets, supervising test activities carried out in the SM18 test plant. I was in particular responsible for the quenches performed around 4 K, useful to provide an indication of the temperature margin of the magnets. I also contributed to the development of test procedures, standard and non-conventional ones, such as techniques for measuring the very low splice resistance (with optimization of the current cycles and current source, together with the definition of LABVIEW instruments to analyse the data and to control the equipment). I participated as well in the definition of performance criteria now inserted in the ID card of each dipole.
Name and address of employer	CERN
Type of business or sector	Superconducting magnets electrical and magnetic qualification
Dates	1 Jan 00 - 30 Apr 01
Occupation or position held	R&D responsible
Main activities and responsibilities	Within the project of a HTS cold dielectric cable prototype, I was in charge of the development of a test plant for critical current and AC loss measurements on high temperature superconductors, including definition of the layout of the system, implementation of the software for acquisition and the execution of tests.
Name and address of employer	EDISON Termoelettrica S.p.A., Turin. Italy
Type of business or sector	Superconductors development for industrial applications
Dates	1 Mar 99 - 31 Dec 99
Occupation or position held	Fellowship in the Department of Physics of the Università degli Studi di Milano
Main activities and responsibilities	Short-term collaboration for the analysis and test of a Nb ₃ Sn prototype winding for a low-beta quadrupole (including the diagnostics for quench and the cold test); resistivity, RRR and contact resistance measurements of joints of Al-stabilized NbTi cables in medium field for the project of the ATLAS Barrel Toroid.
Name and address of employer	INFN – LASA, Milan, Italy
Type of business or sector	Superconductors development and prototyping

Education and training

Dates / Principal subjects / organisation	Nov 07	Habilitation Electrique : Non Electriciens	CERN
-	14 - 25 Jan 06	JUAS 2006 - Accelerator Physics	Joint University Accelerator School – Archamps
-	Jun 05 - Jul 05	USPAS - US Particle Accelerator School - "Fundamentals of accelerator physics"	Cornell University - Ithaca (NY-USA)
-	4 - 14 Apr 05	EMAG-2005: EM Design and Mathematical Optimization in Magnet Technology	CERN
-	Feb 05-Dec 05	Fondamenti di sistemi operativi con elementi di networking TCP/IP	CERN
-	20 - 23 Apr 04	Introduction to ANSYS	CERN
-	Nov 03-Sep 08	PhD in Applied Physics: Finite element modeling and magnet design	Ecole Polytechnique Fédérale de Lausanne - Lausanne (CH)
-	May 02	CAS - Superconductivity and Cryogenics for Accelerators and Detectors - Erice (I)	
-	Jul 00	Course on Superconducting Materials and Applications - Karlsruhe (D)	2nd SCENET Summer School
-	1991 - 1998	Laurea in Fisica	Università degli Studi di Milano – Italy
-	1986 - 1991	Diploma di maturità scientific	Liceo Scientifico di Gavirate – Italy

Personal skills and competences

Mother tongue(s)

Italian

Other language(s)

Self-assessment

European level (*)

English

French

Spanish / Castilian

Understanding				Speaking				Writing	
Listening		Reading		Spoken interaction		Spoken production			
C2	Proficient user	C2	Proficient user	C1	Proficient user	C1	Proficient user	C1	Proficient user
C2	Proficient user	C2	Proficient user	C2	Proficient user	C2	Proficient user	C1	Proficient user
C2	Proficient user	C2	Proficient user	C2	Proficient user	C2	Proficient user	C2	Proficient user

(*) [Common European Framework of Reference \(CEF\) level](#)

Social skills and competences

Team spirit: this is fundamental for the success in my present job.

Good communication skills gained during the Hardware Commissioning Coordination activity and through the experience as official CERN guide.

I'm used to deal with a multicultural environment in my daily work and out-of-work relations.

I'm accustomed in giving frequent presentations to experts and management.

Organisational skills and competences

Planning and organisation skill, fundamental requirement for the coordination activity I'm presently carrying out.

Leadership, expressed in heading daily meetings and in running the test activity as Engineer in Charge in the control room.

Technical skills and competences

Very sound knowledge of superconductivity and related phenomena.

Good knowledge of cryogenic processes, machine interlock and quench protection devices.

Computer skills and competences

Structure Analysis Tools and Field Calculations: ANSYS, ROXIE (basic knowledge), Superfish/POISSON (basic knowledge).

Mathematics Tools: MathCAD, Matlab, M. Origin, Excel, Adobe Illustrator, M. Dreamweaver (HTML)

Mechanical CAE: AutoCAD

Controls: LabView

Artistic skills and competences

Carpentry and photography

Other skills and competences

Official CERN guide

Driving licence(s)

Category B

Additional information

References:

Roberto SABAN	CERNTS/ICC Group Leader	Roberto.Saban@cern.ch
Lucio ROSSI	CERN/AT/MCS Group Leader	Lucio.Rossi@cern.ch
Arnaud DEVRED	Superconductor Systems & Auxiliaries Section Leader for ITER IO	Arnaud.Devred@iter.org
Leonid RIVKIN	EPFL / SB / IPEP / LPAP	leonid.rivkin@epfl.ch
Andrzej SIEMKO	CERN/AT/MEI Deputy Group Leader	Andrzej.Siemko@cern.ch
Giovanni VOLPINI	INFN-LASA INFN-Milan-IT	giovanni.volpini@mi.infn.it

List of relevant publications

- *"Short Circuit Tests: First Step of LHC Hardware Commissioning Completion"*, to be published in the proceedings of EPAC 2008, Genova (I)
- *"Coordination of the Commissioning of the LHC Technical Systems"*, to be published in the proceedings of EPAC 2008, Genova (I)
- *"Performance of the Superconducting Corrector Magnet Circuits during the Commissioning of the LHC"*, to be published in the proceedings of EPAC 2008, Genova (I)
- *"Performance of the Main Dipole Magnet Circuits of the LHC during Commissioning"*, to be published in the proceedings of EPAC 2008, Genova (I)
- *"Scheduling the Powering Tests"*, to be published in the proceedings of EPAC 2008, Genova (I)
- *"The commissioning of the LHC technical systems"*, Particle Accelerator Conference, 2007. PAC. IEEE 25-29 June 2007 Page(s): 3801 – 3803
- *"The Commissioning of the DFBs"*, Hardware Commissioning Engineering Specification, EDMS 755782.
- *"A Finite Element Model for Mechanical Analysis of LHC Main Dipole Magnet Coils"*, presented at the ASC Conference, Seattle, August, 27- Sept., 1 2006.
- *"Status Report on the Superconducting Dipole Magnet Production for the LHC"*, presented at the ASC Conference, Seattle, Washington, 27, August - 1, September, 2006.
- *"A Non-linear Finite Element Model for the LHC Main Dipole Coil Cross-section"*, IEEE Trans. Appl. Supercond., Vol. 16, no 2, pp. 1294-1297, 2005. Presented at the 19th International Conference on Magnet Technology (MT - 2005) 18/09/2005 - 23/09/2005 Genova, Italy.
- *"Conductor-limited quenches of LHC superconducting main dipole"*. IEEE Trans. Appl. Supercond.: 14 (2004)no, 2 pp 153-158.
- *"Performance of the first LHC pre-series superconducting dipoles"*, Proceedings of the ASC conference, Houston-Texas, August 2002
- *"Critical state analysis in MgB2 bulk by means of quantitative MO technique"*, cond-matt/0104069 (2001)
- *"Experimental characterization of resistive joints for use inside ATLAS toroids"*, Proceedings of the ASC conference, Virginia Beach-Florida, September 2000
- *"AC losses in transport current regime in applied AC magnetic field: experimental analysis and modeling"*, Proceedings of the ASC conference, Virginia Beach-Florida, September 2000
- *"Measurement of an internal joint and a layer-to-layer joint as a function of the magnetic field"*, internal INFN report (1999)
- *"Development and characterization of ITD multifilamentary Nb3Sn superconductors for 10-15 T field magnets"*, INFN/TC-99/25 report, November 1999
- *"Characterization of a high critical current, low cabling degradation, NbSn conductor for accelerator magnets"*, MT15-Proceedings of the Fifteenth International Conference on Magnet Technology, p.993, Science Press (1998)